The Thesis Committee for Scott Joseph Schoen, Jr.
certifies that this is the approved version of the following thesis:

# Acoustic Characterization of Encapsulated Microbubbles at Seismic Frequencies

APPROVED BY

SUPERVISING COMMITTEE:

Mark F. Hamilton, Supervisor

Preston S. Wilson

# Acoustic Characterization of Encapsulated Microbubbles at Seismic Frequencies

**by**

**Scott Joseph Schoen, Jr., B.S.**

**THESIS**

Presented to the Faculty of the Graduate School of

The University of Texas at Austin

in Partial Fulfillment

of the Requirements

for the Degree of

**MASTER OF SCIENCE IN ENGINEERING**

The University of Texas at Austin

December 2013

To Mom & Dad, Stephanie, Katie, Sarah, and Tyler,
my perpetual teachers and role models

# Acknowledgments

The work on this thesis would not have been possible without the guidance and wisdom of my advisor, Professor Mark Hamilton. His passion for acoustics and for research has been inspiring and humbling. Having had the chance to learn from him, in and out of the classroom, has been the most rewarding of my academic experiences.

I am indebted to Professor Preston Wilson, for agreeing to be a reader on this thesis, and for allowing me access to his experimental facilities. Dr. Wilson's dissertation and related research have been an invaluable resource for the resonance tube measurements in this thesis, and his generosity and advice have informed most of my results. Thanks to Dr. Richard Coffin of the U.S. Naval Research Laboratory for providing access to the pressure vessel used in this work.

It has also been a privilege to work with Drs. Yurii Ilinksii and Evgenia Zabolotskaya; learning from their substantial contributions to acoustics and their related work on this topic has been an amazing opportunity.

The research described herein was funded by the Advanced Energy Consortium, which is administered by the Bureau of Economic Geology at The University of Texas at Austin. AEC's support of education and basic research has afforded me the ability to further my education. I am incredibly thankful to have had the opportunity to learn and work on this project over the last two years. The success of this work was also contingent upon collaboration with Professor Michael Rubinstein's synthesis group at The University of North Carolina at Chapel Hill: Drs. Rubinstein, Sergei Sheiko, and Natalia Lebedeva. They have supplied not only contrast agents, but the knowledge, advice, insight, and understanding that have allowed experiments to happen.

I am grateful for the patience and guidance of Craig Dolder, who has been enormously helpful for the entirety of my research. I am thankful also to Chad Greene,

whose thesis has been indispensable, and for willingness to train and advise me long after he was obligated to do so.

I have been fortunate for the last two years to share an office with Daniel Tengelsen, from whom I've learned a good deal about acoustics, bubbles, and the virtues of Python. Thanks also to my fellow graduate students Ben Copenhaver, Kyle Spratt, Nick Joseph, and Tim Klatt, who were willing to help with the heavy lifting.

Finally, I am incredibly fortunate and incredibly thankful for unwavering love and support of my parents, who are wholly responsible for any modicum of success I may ever have. And for sharing the adventure of becoming a Texan, thanks to my incomparable fiancée Stephanie Tam. It's impossible not to look forward to the future, whatever it may bring, knowing she's a part of it.

Scott Joseph Schoen, Jr.

# Acoustic Characterization of Encapsulated Microbubbles at Seismic Frequencies

Scott Joseph Schoen, Jr., M.S.E.
The University of Texas at Austin, 2013

Supervisor: Mark F. Hamilton

Encapsulated microbubbles, whose diameters are on the order of microns, are widely used to provide acoustic contrast in biomedical applications. But well below the resonance frequencies of these microbubbles, any acoustic contrast is due solely to their relatively high compressibility compared to the surrounding medium. To estimate how well microbubbles may function as acoustic contrast agents in applications such as borehole logging or underground flow mapping, it must be determined how they behave both at atmospheric and down-well conditions, and how their presence affects the bulk acoustic properties of the surrounding medium, most crucially its specific acoustic impedance. Resonance tube experiments were performed on several varieties of acoustic contrast agents to determine their compressibility as a function of pressure and temperature, and the results are used to estimate the effect on sound propagation when they are introduced into rock formations.

# Table of Contents

# List of Figures

# List of Symbols

**Roman**

| | |
|---|---|
| $a$ | Outer radius of cylindrical tube |
| $a_i$ | Acoustic pressure amplitude in layer $i$ |
| $b$ | Inner radius of cylindrical tube |
| $c$ | Sound speed |
| $c_{\text{eff}}$ | Sound speed (phase speed if dispersive) in effective medium |
| $d_i$ | Thickness of layer $i$ |
| $D$ | Thermal diffusivity |
| $f$ | Frequency |
| $j$ | Imaginary unit $j = \sqrt{-1}$ |
| $k$ | Wavenumber $k = \frac{\omega}{c}$ |
| $k_{\text{liq}}$ | Wavenumber in liquid $k_{\text{liq}} = \frac{\omega}{c_{\text{liq}}}$ |
| $K$ | Bulk modulus |
| $K_{\text{bub}}$ | Bulk modulus of bubble |
| $K_{\text{CA}}$ | Bulk modulus of contrast agent |
| $K_{\text{dry}}$ | Bulk modulus of dry rock frame |
| $K_{\text{eff}}$ | Bulk modulus of the effective medium |
| $K_{\text{min}}$ | Bulk modulus of rock mineral (i.e., the rock material itself with no pores) |
| $K_f$ | Bulk modulus of pore fluid |
| $K_r$ | Bulk modulus of saturated rock |
| $l_D$ | Thermal boundary layer thickness inside bubble wall |
| $m$ | Mass |
| $N_b$ | Number of bubbles per unit volume $N_b = \frac{\text{Number of Bubbles}}{\text{Total Volume}}$ |
| $p$ | Acoustic pressure |
| $P$ | Total pressure |
| $P_0$ | Equilibrium pressure |
| $P_\infty$ | Pressure far from the bubble |

| | |
|---|---|
| $\mathcal{R}$ | Pressure reflection coefficient $\mathcal{R} \equiv \frac{p_{\text{reflected}}}{p_{\text{incident}}}$ |
| $R$ | Instantaneous bubble radius |
| $R_0$ | Equilibrium bubble radius |
| $t$ | Time, and with time dependence $p \propto e^{j\omega t}$ |
| $\mathcal{T}$ | Pressure transmission coefficient $\mathcal{T} \equiv \frac{p_{\text{transmitted}}}{p_{\text{incident}}}$ |
| $T$ | Temperature |
| $T_e$ | Bubble expansion temperature |
| $T_g$ | Glass transition temperature |
| $v$ | Volume |
| $v'$ | Perturbation of volume from equilibrium $v' = v - v_0$ |
| $v_0$ | Equilibrium volume |
| $V_B$ | Biot's reference velocity |
| $V_P^{\text{dry}}$ | P-wave velocity in the dry rock frame |
| $V_P^r$ | P-wave velocity in the saturated rock |
| $V_S$ | S-wave velocity |
| $z$ | Vertical coordinate |
| $Z$ | Specific acoustic (characteristic) impedance |
| $Z_r$ | Plane-wave characteristic impedance of the saturated rock |

**Greek**

| | |
|---|---|
| $\alpha$ | Attenuation |
| $\alpha'_{mn}$ | $n^{\text{th}}$ root of the first derivative of the Bessel function of order $m$, i.e., $J'_m(\alpha'_{mn}) = 0$ |
| $\beta$ | Dimensionless bubble volume (also referred to as compression factor) $\beta = v/v_0$ |
| $\chi$ | Heat diffusion parameter |
| $\delta$ | Damping coefficient |
| $\eta$ | Shear viscosity |
| $\gamma$ | Ratio of specific heats $\gamma = \frac{c_P}{c_v}$ |
| $\kappa$ | Polytropic index |
| $\lambda$ | First Lamé parameter |
| $\mu$ | Shear modulus (second Lamé parameter) |
| $\mu_r$ | Shear modulus of the saturated rock |
| $\Omega$ | Porosity |

| | |
|---|---|
| $\omega$ | Angular frequency $\omega = 2\pi f$ |
| $\Phi$ | Argument given by Eq. (2.44) |
| $\phi$ | Relative volume $\phi = \frac{v}{v_{\text{total}}}$; void fraction for gas bubbles in liquid |
| $\rho$ | Density |

**Mathematical Functions and Operators**

| | |
|---|---|
| $J_n(x)$ | Bessel function of order $n$ and argument $x$ |
| $\Delta A$ | Change in quantity $A$ |
| $\delta(x)$ | Dirac delta function of argument $x$ |
| Im $\tilde{z}$ | Imaginary part of complex number $\tilde{z}$ |
| Re $\tilde{z}$ | Real part of complex number $\tilde{z}$ |

# Chapter 1

# Introduction

## 1.1 Motivation and Background

Broadly, this thesis deals with the characterization of encapsulated microbubbles, and examination of the feasibility of their use as acoustic contrast agents to detect water flow in geological formations. In previous years and still to this day a number of groups, including one at Applied Research Laboratories, The University of Texas at Austin (ARL:UT), have been investigating magnetic nanoparticles for this purpose due to their very small size and ability to move easily through pore spaces. However, recent synthesis of smaller, more robust microbubbles have made acoustic contrast agents promising. At least two applications have motivated interest in such contrast agents. One is secondary recovery, in which a resevoir is flooded with water to displace any remaining oil toward the well for extraction, or a well itself is flooded with water in an attempt to direct any remaining oil to nearby wells for recovery there. In both cases, knowing the location of the interface between the oil and water would provide important information about the progress and effectiveness of the technique. The resulting oil/water interface is difficult to detect acoustically, as the characteristic impedances of the two media are very similar. Acoustic contrast agents added to the water flood could potentially make its front (interface with the oil) easier to detect by creating a larger impedance mismatch between the water and oil.

A second application of interest is hyrdraulic fracturing, in which liquid is injected into a well at high pressure to create fractures in the surrounding rock, thus producing pathways for the hydrocarbons to flow more easily from the resevoir into the borehole. Attempts have been made to determine the locations and geometries of these fractures using microseismic monitoring, a technique in which passive recordings are made of

the noise generated as the fractures form due to crack propagation. However, this technique faces issues of small signal-to-noise ratios and large uncertainties that can make resolving these fractures difficult.[1] The use of acoustic contrast agents within these fractures may allow seismic techniques to yield more reliable characterization of the fractures.

The use of medical ultrasonic imaging has been commonplace for decades, and microbubbles have been used in this context with great success to produce acoustic contrast and enable more effective imaging.[2–6] Gas bubbles exhibit dramatic resonance behavior, as do encapsulated bubbles, provided their shells are sufficiently compliant. Thus ultrasound incident on the bubbles at frequencies near resonance is strongly scattered. For bubbles with radii of several microns, as are encountered in medical ultrasound imaging, up to radii of several millimeters, as are encountered in calibration studies reported in this thesis, the resonance frequencies range from several megahertz for the former to several kilohertz for the latter. See the gray area on the right in Fig. 1.1, which is a plot of the specific acoustic impedance of water containing gas bubbles of radius 10 microns, and occupying 1% of the fluid volume compared with that of pure water. This is well above the useful frequency range for seismic imaging, which is indicated by the gray region on the left in Fig. 1.1. Therefore the resonant behavior of bubbles is not the primary contrast mechanism of interest here. Instead, contrast is acheived by the quasi-static behavior of the bubbles in the surrounding medium, usually water.

Well below resonance, the bubbles behave simply as inclusions having compressibility much greater than that of the surrounding liquid, four orders of magnitude for gas bubbles in water at atmospheric conditions. Since such contrast agents, whether pure gas or shelled, are significantly softer than the liquid around them, their effect is to reduce the overall bulk modulus (stiffness) of the fluid. The sound speed in the fluid, and therefore the specific acoustic impedance of the fluid, are reduced accordingly. It this manner, addition of the much more compressible bubbles to the liquid, even in relatively small quantities, causes a significant change in the acoustic

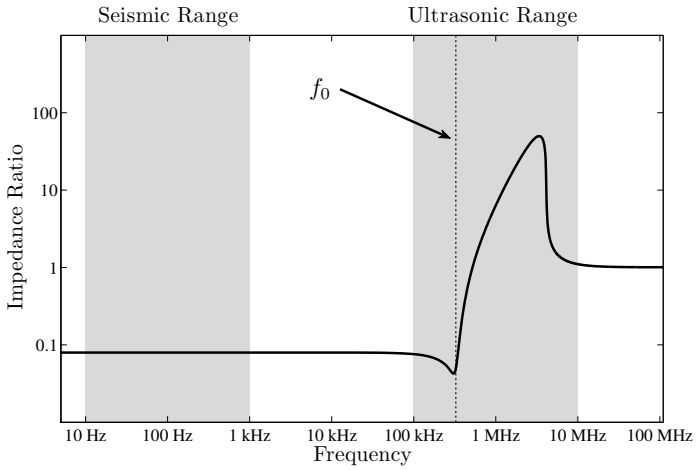


**Figure 1.1:** Ratio of specific acoustic impedance magnitude $Z_2/Z_1$ for water with bubbles $Z_2$ and water without bubbles $Z_1$. The calculations are made for air bubbles of radius 10 $\mu$m in water and occupying 1% of the total volume. An impedance ratio of 1 implies no contrast. The resonance frequency of these particular bubbles, shown by the dotted line, is denoted $f_0$.

properties of the bubble/liquid mixture, and thus provides the acoustic contrast that is observed at low frequencies.

However, the high-pressure, high-temperature conditions of down-well applications present a challenge: the bubbles must remain sufficiently soft to provide acoustic contrast even at high pressures, conditions which can cause rapid diffusion of gas out of the bubbles and into the surrounding liquid. Additionally, the bulk modulus of a gas bubble is proportional to the local pressure, and therefore a gas bubble at a depth of 1 km, which underwater is subjected to a hydrostatic load of approximately 100 atmospheres, is 100 times less compressible than at ground level. Recent synthesis of microbubbles with tunable shells and core characteristics at University of North Carolina at Chapel Hill (UNC) is promising in that it provides bubbles that can endure the harsher conditions present in downhole conditions. It remains then to determine the physical properties, most fundamentally the bulk modulus, of the synthesized contrast agents at these elevated conditions. If the properties of the contrast agents are known, then existing models for propagation in effective media (i.e.,

media comprised of several separate constituents, such as gas bubbles in liquid, but modeled as a homogeneous medium) can be used to estimate the magnitude of the contrast they will provide in resevoir conditions.

It was the primary purpose of the research reported in this thesis to make measurements of the bulk moduli of contrast agents provided by UNC at frequencies relevant to seismic imaging. From the bulk moduli may be determined the sound speed and specific acoustic impedance of a liquid containing such contrast agents, and from this information one may calculate the extent to which acoustic contrast is enhanced for seismic imaging.

## 1.2 Outline of Thesis

Chapter 2 reviews various models of linear acoustic propagation in mixtures. First considered are homogeneous mixtures of fluids, and then effective medium models specific to bubbly liquids are considered. These fluid models are coupled with low-frequency models of poroelastic media to estimate the impedance change when gas bubbles are introduced into water-saturated, porous rock, with the effects of elevated presure included.

Chapter 3 describes the resonance tube and associated apparatus employed for experiments discussed in Chapter 4. Calibration is performed with a static gas bubble apparatus, and sources of uncertainty for the arrangement are considered. A one-dimensional layered-medium model of a resonance tube containing discrete samples of a second acoustic medium is developed to estimate the limits of the homogeneous mixture assumption underlying the modeling.

Chapter 4 describes measurements at ambient conditions, elevated pressure, and elevated temperature on contrast agents synthesized and provided by UNC. Alterations of the models discussed in Chapter 2 are made to estimate the effects of elevated pressure on contrast agent behavior, and comparison with ultrasonic measurements performed by the synthesis team at UNC is made.

While the feasibility of detection and the methods and limitations of real equipment are concerns that remain, these factors are not considered herein. Ultimately, this thesis seeks to estimate the magnitude of the changes in effective acoustic properties that might be expected due to introduction of contrast agents in geologic conditions.

# Chapter 2

# Effective Medium Models for Acoustic Propagation

This chapter outlines the relevant models that will be used in measurements and simulations involving the acoustics of bubbly media. Section 2.2 describes models of propagation in bubbly liquid. Both quasi-static (Wood's law) and dynamical approaches (Zabolotskaya and Soluyan, Commander and Prosperetti) are reviewed for gas bubbles in water. Section 2.3 outlines Gassmann-Biot theory, which describes low-frequency propagation in a liquid-saturated, poroelastic rock. The effect of air bubbles in saturated rock is estimated at atmospheric conditions by using Wood's law. While the effects of bubble shells are considered in Chapter 4, the models discussed here will be the basis of predictions for contrast agents (synthesized microbubbles with shells), and subsequently for rock impregnated with these contrast agents.

## 2.1 Background

Modeling accurately the propagation of acoustic energy through complicated media is difficult, and it is often more convenient to find a way to treat the entire medium as having effective properties. The medium then may be approximated as a homogeneous medium with those effective parameters. Used also in the context of electromagnetic waves,[7,8] the underlying intuitive basis of these effective medium models is that the inhomogeneities of the medium are significantly smaller than a wavelength.[†] In this way, it is reasoned that the incident energy "sees" the averaged

[†]The wavelength in the effective medium is not known *a priori*. However, since the effective medium of interest often consists of a host medium with inclusions, the wavelength in the host medium with respect to the size of the inclusions is the primary benchmark.

macroscopic properties of the mixture, rather than the localized discontinuities of material properties. This long-wavelength criterion limits such effective medium theories to the corresponding low-frequency regime. While straightforward, such models are powerful tools due to their simplicity and "surprisingly accurate"[9] results.

## 2.2 Bubbly Liquids

### 2.2.1 Wood's Law

A basic model of the low-frequency acoustic response of a mixture of substances can be developed from basic principles. The small-signal[†] speed of sound $c$ in a fluid is given by[10,11]

$$c = \sqrt{\frac{K}{\rho}}, \tag{2.1}$$

where $K$ and $\rho$ are the material's bulk modulus and density, respectively. The material properties on the right-hand side of Eq. (2.1) are understood to be evaluated under local ambient conditions.[‡]

If the medium is composed of more than one immiscible fluid, or a liquid containing microbubbles or even elastic particles, then Eq. (2.1) must account for the effect each individual component has on the overall properties of the mixture. The mixture is treated as a new homogeneous medium, with effective properties determined by the properties and relative volumes of each constituent.

It is assumed that each the various phases of the mixture does not undergo any change of mass or volume when combined with the others at equilibrium conditions. In this case, if the total volume $v$[§] is composed of $N$ components, then the total

[†]In general, the quantity $c^2 = \partial P/\partial\rho$ is a thermodynamic variable that depends on acoustic, as well as ambient, pressure. However, Eq. (2.1) is considered constant in linear acoustical theory, i.e., for infinitesimal, or "small-signal" disturbances in the medium, such as those considered in the present work.

[‡]By low frequency is meant that the medium responds quasi-statically to the pressure fluctuations in the sound wave, for example, well below any bubble resonances for gas bubbles in liquids.

[§]Lower case $v$ will be used for volume, rather than the more traditional $V$, reserving the latter for the velocity of elastic waves in rock to conform with the conventional notation used in geophysics.

volume is simply the sum of the volumes of each material; similarly, the total mass $m$ is the sum of the mass of each material. Thus,

$$v = \sum_{i=1}^{N} v_i, \tag{2.2}$$

$$m = \sum_{i=1}^{N} m_i. \tag{2.3}$$

The effective density $\rho_{\text{eff}}$ is the total mass divided by the total volume:

$$\rho_{\text{eff}} = \frac{\sum_{i=1}^{N} m_i}{\sum_{i=1}^{N} v_i}. \tag{2.4}$$

But since $m_i = \rho_i / v_i$ and $\sum_{i=1}^{N} v_i = v$, Eq. (2.4) becomes

$$\begin{aligned} \rho_{\text{eff}} &= \frac{1}{v} \sum_{i=1}^{N} \rho_i v_i \\ &= \sum_{i=1}^{N} \rho_i \frac{v_i}{v}. \end{aligned} \tag{2.5}$$

Then substituting the definition of the volume fraction

$$\phi_i \equiv v_i / v \tag{2.6}$$

into Eq. (2.5) gives

$$\rho_{\text{eff}} = \sum_{i=1}^{N} \rho_i \phi_i. \tag{2.7}$$

Next, the effective bulk modulus $K_{\text{eff}}$ of a material is defined by

$$K_{\text{eff}} = -v \frac{\Delta P}{\Delta v}, \tag{2.8}$$

where $\Delta P$ and $\Delta v$ are quasi-static pressure and volume increments, respectively, evaluated for a material near its equilibrium state. By Eq. (2.2), the total volume is simply the sum of the consitutent volumes, and so the total volume change is the sum of the volume changes of each material:

$$\Delta v = \sum_{i=1}^{N} \Delta v_i. \tag{2.9}$$

Rewriting Eq. (2.9) using the definition of the bulk modulus of each phase to solve for $\Delta v_i$ gives

$$\Delta v = \sum_{i=1}^{N} \left( -\frac{v_i \Delta P}{K_i} \right). \tag{2.10}$$

Substituting Eq. (2.10) into Eq. (2.8) and cancelling the pressure change $\Delta P$ gives

$$K_{\text{eff}} = v \sum_{i=1}^{N} \frac{1}{v_i / K_i}, \tag{2.11}$$

or

$$\frac{1}{K_{\text{eff}}} = \sum_{i=1}^{N} \frac{v_i / v}{K_i}. \tag{2.12}$$

Use of the definition of the volume fraction permits Eq. (2.12) to be written

$$\frac{1}{K_{\text{eff}}} = \sum_{i=1}^{N} \frac{\phi_i}{K_i}. \tag{2.13}$$

If the effective medium of interest consists of two constituents, then Eqs. (2.7) and (2.13) can be written

$$\rho_{\text{eff}} = \phi \rho_1 + (1 - \phi) \rho_2 \tag{2.14}$$

$$\frac{1}{K_{\text{eff}}} = \frac{\phi}{K_1} + \frac{1 - \phi}{K_2}, \tag{2.15}$$

where $\phi = \phi_1$. Equations (2.14) and (2.15) are collectively known as "Wood's law" or "Wood's equations", and are generally credited to A. B. Wood, who published them in this form in 1930.[†]

#### 2.2.1.1 Bubbles and Wood's Law

Wood's law is often, to a good approximation, applied to effective media consisting of a liquid with gas bubbles. Indeed, Wood had in mind precisely this application

[†]As has been noted,[12] Wood's law is equivalent to expressions published by Arnulph Mallock some 20 years previously.[13] Indeed, the first edition of Wood's book[14] includes the citation, while subsequent editions do not.[15] Therefore it has been proposed that Eqs. (2.14) and (2.15) be termed the "Mallock-Wood" equations. For brevity and by convention, "Wood's law" is used in this thesis, though Mallock is due credit for the relations.

when he developed his mixture relations. In the zero-frequency limit, meaning in practice that the frequency is far below any bubble resonance, Wood's law provides a very accurate estimation of the effective sound speed,[16]

$$c_{\text{eff}} = \sqrt{\frac{K_{\text{eff}}}{\rho_{\text{eff}}}}. \tag{2.16}$$

From Eqs. (2.14) and (2.15), for air in water,

$$c_{\text{eff}} = \sqrt{\frac{\left(\frac{\phi}{K_{\text{air}}} + \frac{1-\phi}{K_{\text{water}}}\right)^{-1}}{\phi\rho_{\text{air}} + (1-\phi)\rho_{\text{water}}}}. \tag{2.17}$$

The solid line in Fig. 2.1 shows the sound speed prediction of Wood's law as a function of the volume fraction $\phi$ (or "void fraction") of air. Unless otherwise noted, the properties for water and air used for calculations in this thesis are listed in Table 2.1.

| | Sound Speed [m/s] | Density [kg/m$^3$] | Bulk Modulus [Pa] |
|---|---|---|---|
| Water | 1482 | 998 | $2.19 \times 10^9$ |
| Air | 343 | 1.2 | $1.40 \times 10^5$ (adiabatic) |
| | | | $1.01 \times 10^5$ (isothermal) |

**Table 2.1:** Nominal material properties for water and air.

Perhaps unintuitively, Wood's law predicts that the sound speed in a mixture of two fluids is lower than the sound speed in either medium separately for a large range of volume fractions; the inset of Fig. 2.1 indicates that this effect persists until the void fraction approaches unity (i.e., the mixture becomes pure air). It is also worth noting that even very small void fractions can cause very significant changes in the sound speed. From Fig. 2.1 it can be seen that a mixture of water that contains just 0.01% air bubbles ($\phi = 10^{-4}$) has a sound speed that is nearly 40% lower than that of pure water.

If the void fraction is small, which is often the case for air bubbles in water, then Eq. (2.17) may be simplified. For $\phi \ll 1$, and since $\rho_{\text{air}} \ll \rho_{\text{water}}$, Eqs. (2.14) and

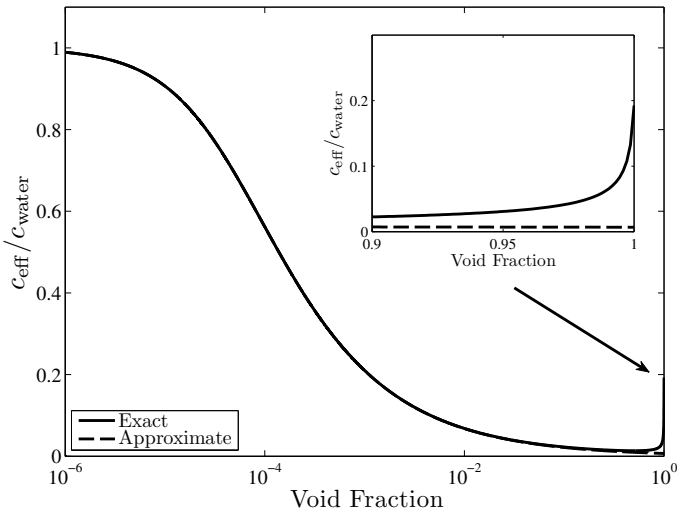


**Figure 2.1:** Sound speed prediction of Wood's law for air in water, given by Eq. (2.17). The approximate form, Eq.(2.20), is indicated by the dashed line. The bulk modulus of water is taken to be $K_{\text{water}} = 2.19$ GPa. The air bubbles are assumed to pulsate isothermally, and so $K_{\text{air}} = P_0$, where $P_0$ is atmospheric pressure. The inset show an enlargement of the region for void fractions close to unity. As the mixture approaches 100% air, the effective sound speed quickly approaches that of air, for which $c_{\text{air}}/c_{\text{water}} = 0.193$. Because $K_{\text{air}}$ is taken to be its isothermal value, the prediction for $c_{\text{air}}$ differs from its value for actual acoustic propagation in air, which is an adiabatic process.

(2.15) may be approximated as

$$\rho_{\text{eff}} \simeq \rho_{\text{water}} \tag{2.18}$$

$$\frac{1}{K_{\text{eff}}} \simeq \frac{1}{K_{\text{water}}} + \frac{\phi}{K_{\text{air}}}. \tag{2.19}$$

Substitution of Eqs. (2.18) and (2.19) into Eq. (2.16) yields

$$c_{\text{eff}} = \frac{c_{\text{water}}}{\sqrt{1 + \phi K_{\text{water}}/K_{\text{air}}}}, \quad \phi \ll 1. \tag{2.20}$$

From Fig. 2.1 it can be seen that this approximate form (dashed line) accurately matches the exact prediction (solid line) for all but very large ($\phi > 10\%$) void fractions. Equation (2.20) is thus valid for all conceivable void fractions of interest in the present investigation.

If the opposite limit is taken, such that $\phi \simeq 1$, then the effective sound speed based on Wood's law may be approximated as

$$c_{\text{eff}} = \frac{c_{\text{air}}}{\sqrt{1 + (1-\phi)\rho_{\text{water}}/\rho_{\text{air}}}}, \quad \phi \simeq 1. \tag{2.21}$$

Rather than seeing a sharp decrease in bulk modulus of the water due to the gas bubbles, in this limit the air experiences a large increase in density due to the water droplets. Of course, at these high void fractions, the mixture has become an aerosol, i.e., liquid droplets suspended in gas, rather than gas bubbles suspended in liquid. It should be noted that discussion of Wood's law in the limit of $\phi \simeq 1$ is purely academic in the context of acoustics, because the dynamics of aerosols is very complicated due to the large inertia of the water droplets relative to that of air. The water droplets translate out of phase with the air by an amount determined by the frictional force acting on the surfaces of the droplets. The size of the droplets is important, not just their overall volume fraction, a result of which is the appearance of a time constant. Thus, for the purpose of acoustics, the approximate Eq. (2.20) is valid at all void fractions for which Wood's law is an appropriate model of an effective *acoustical* medium.

#### 2.2.1.2 Contrast Agents

The enormous changes in sound speed, and thus specific acoustic impedance, in a fluid due to the presence of bubbles imply a great potential for acoustic contrast at low frequencies. However, high-pressure, high-temperature conditions in boreholes exclude pure gas bubbles as candidates for such applications. As the ambient conditions are raised substantially from atmospheric, the gas within the bubble will diffuse into the host liquid, negating the increased compliance effects seen when the gas exists as a bubble.

One solution would be to use much more robust contrast agents that will remain intact under these conditions. However, the large effect of air bubbles on sound speed shown in Fig. 2.1 is due to the substantial difference in compliance between the

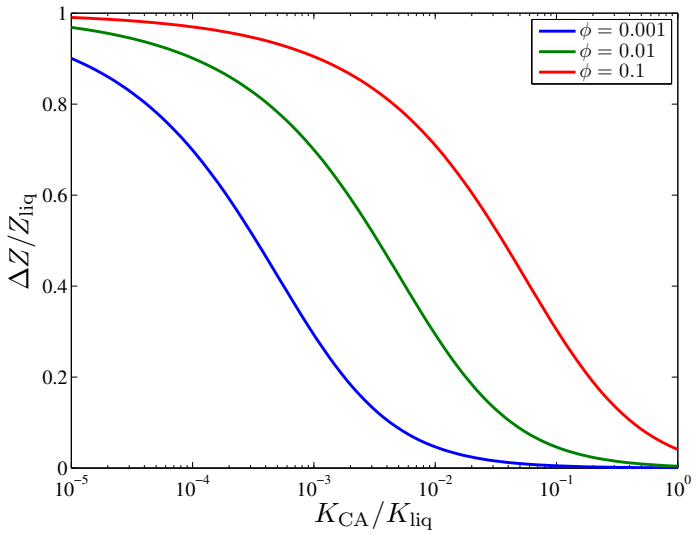


**Figure 2.2:** Relative change in characteristic impedance for a contrast agent with relative volume $\phi$, density $\rho_{\mathrm{CA}}$ and bulk modulus $K_{\mathrm{CA}}$, homogeneously combined with a liquid with density $\rho_{\mathrm{liq}}$ and bulk modulus $K_{\mathrm{liq}}$, as a function of its bulk modulus $K_{\mathrm{CA}}$. The density $\rho_{\mathrm{CA}}$ is taken to be 20% of $\rho_{\mathrm{liq}}$, but this effect is negligible for the volume fractions considered.

two media: air is about 10,000 times more compressible than water.[17,18] Increasing the viability of contrast agents at high pressure necessitates a substantial increase in the stiffness of the particles. But as the bulk modulus of the inclusions becomes comparable to that of the host liquid, the potential for contrast is severly diminished.[†]

Figure 2.2 shows the change in characteristic impedance for the indicated volume fraction of a contrast agent as a function of its bulk modulus. That is, the difference between the effective characteristic impedance of the mixture

$$Z_{\mathrm{eff}} = \rho_{\mathrm{eff}} c_{\mathrm{eff}} \tag{2.22}$$

and that of the liquid $Z_{\mathrm{liq}} = \rho_{\mathrm{liq}} c_{\mathrm{liq}}$. This change is plotted as a function of $K_{\mathrm{CA}}$, the bulk modulus of the contrast agent, at the indicated volume fractions $\phi$. For air in

[†]While it would be possible to increase the characteristic impedance of the effective medium, doing so would require void fractions approaching unity of a contrast agent with a bulk modulus several orders of magnitude greater than the host liquid. For water, where $K_{\mathrm{liq}} \sim 2$ GPa, not even diamond ($K_{\mathrm{CA}} = 500$ GPa[19]) would be feasible, aside from any cost considerations.

water, where $K_{\text{air}}/K_{\text{water}} \sim 10^{-5}$, the impedance is lowered by about 90% when the void fraction is 1%. However, for something like alcohol in water $K_{\text{alc}}/K_{\text{water}} \sim 10^{-1}$, the impedance change is only about 5% for $\phi = 1\%$.

### 2.2.2 Bubble Dynamics

The main deficiency of Wood's law with respect to its application to acoustic propagation in bubbly liquids is its neglect of any dynamical behavior of the bubbles, because Eqs. (2.14) and (2.15) were derived subject to the assumption of quasi-static compression of the effective fluid. In the present section, the Rayleigh-Plesset equation is used to account for the resonant, frequency-dependent dynamical response of the bubbles to an oscillating pressure field. The Rayleigh-Plesset equation is combined with a wave equation for an effective medium to determine the speed, and also attenuation, of sound in the medium.

One of the earliest mathematical treatments of free bubble pulsations was given by Minnaert in 1933.[20] Interested in the mechanism of sound production in water waves, streams, and waterfalls, Minnaert set out to quantify the harmonic oscillations of gas bubbles. Minnaert first considered the state of a single spherical bubble when it was maximally compressed, in which case the total energy would be the potential energy stored by the compressed gas. Once compressed, the bubble wall is then driven radially outward by the gas. The bubble expands most quickly, and has the greatest bubble wall velocity, when it passes by its equilibrium radius, at which point the gas is again at its equilibrium pressure, and the total energy is the kinetic energy of the liquid being pushed radially outward from the bubble. If there are no losses, both extremes represent the total energy. Equating the two expressions allowed Minnaert to solve for a natural pulsation frequency:

$$f_M = \frac{1}{2\pi R_0}\sqrt{\frac{3\gamma P_0}{\rho_{\text{liq}}}}, \tag{2.23}$$

where $\gamma$ is the ratio of specific heats for the gas, $P_0$ is the equilibrium pressure of the gas inside the bubble, and $R_0$ is the equilibrium radius of the bubble. While

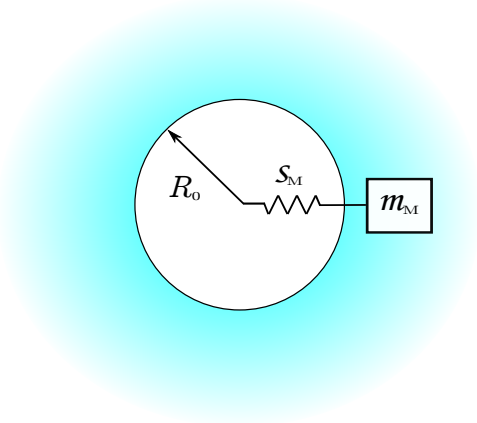


**Figure 2.3:** Mass-spring model of a gas bubble.[21,22] The effective mass $m_M$ is due to the inertia of the surrounding liquid, and the stiffness $s_M$ due to the gas within the bubble.

this model of bubble oscillations ignores some important effects, for example any damping mechanisms or effects of surface tension, it is an important benchmark for determining when bubble resonance effects must be included.

It is common to model the bubble as a lumped-element oscillator after identifying the gas inside as an acoustic compliance and the entrained liquid mass outside as an acoustic inertance,[11] a cartoon of which is shown in Fig. 2.3.

The appearance of $\gamma$ in Eq. (2.23) implies adiabatic oscillation of the gas pressure and bubble volume, e.g., for a diatomic gas such as air $\gamma = 1.4$. A more general relation for the equation of state is[23]

$$Pv^{\kappa} = \text{constant}, \tag{2.24}$$

where $\kappa$ is referred to s the polytropic index of the gas. Depending on the frequency and size of the bubble, $\kappa$ will vary between 1, the isothermal case, and the ratio of specific heats $\gamma$, for the adiabatic case; see Fig. 2.4. Then in general for a gas bubble,

$$K_{\text{bub}} = \kappa P_0. \tag{2.25}$$

Replacing $\gamma$ with $\kappa$ in Eq. (2.23) accounts for the effect of heat conduction on the natural frequency. A full discussion of bubble thermodynamics is outside the scope

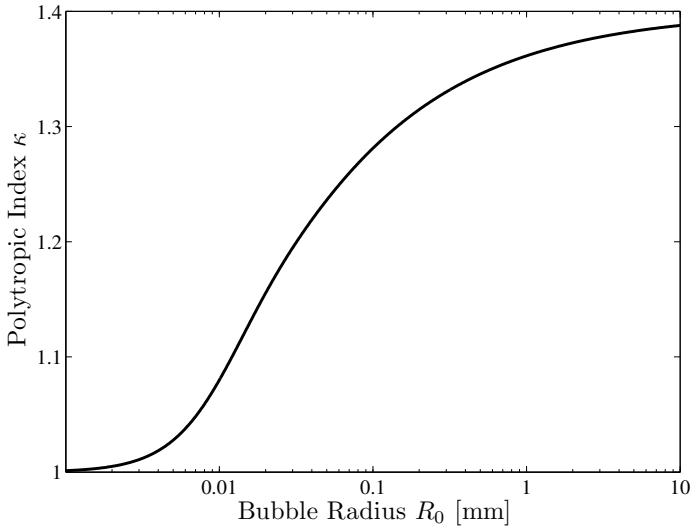


**Figure 2.4:** Polytropic index for air bubbles in water. Computed from Eq. (3.197) of Ref. 24.

of this thesis, but the area is well-studied (see, e.g., Ref. 24). The relevant thermal behavior of the bubble is accounted for by the models discussed in Sec. 2.2.3.

### 2.2.3 Wave Propagation in a Bubbly Liquid

#### 2.2.3.1 Historical Context

The roots of modern effective medium models for propagation of sound in bubbly liquid can be traced back the benchmark papers in 1967 and 1973 by Zabolotskaya and Soluyan.[25,26] Theirs are nonlinear acoustic wave propagation models because, in addition to introducing strong dispersion, the bubbles also introduce strong nonlinearity. Strong nonlinearity and dispersion are also inherent to nonlinear optics, interest in which had exploded in the early 1960s following the invention of the laser.[†] The leading theorist in nonlinear optics in the former Soviet Union was Khokhlov, then head of the group at Moscow State University in which Zabolotskaya and Soluyan worked.

[†]The laser was invented simultaneously and independently in the former Soviet Union and in the United States, for which two Soviets and one American jointly received the 1964 Nobel Prize in physics.[27]

The focus here is on the linear form of Zabolotskaya and Soluyan's model, and in particular the dispersion relation, which accounts for the dependence of both phase speed and attenuation of the sound wave on frequency. While attenuation was not a concern of the 1967 paper, it was one focus of the 1973 paper, where they introduced a general damping constant $f$ and proceeded to show how to determine it based on measurement of acoustic attenuation in the bubbly liquid. Specifically, by obtaining the acoustic attenuation coefficient from the dispersion relation they derived, they showed how to determine the damping constant from a measurement of acoustic attenuation, recognizing that $f$ "accounts for the losses in overcoming internal friction in the liquid-air bubble system [and] energy dissipation due to heat transfer, which produces a phase shift between the bubble volume and pressure in it, as well as acoustic radiation losses".

In the absence of such acoustic attenuation measurements, or even direct measurements of the damping constant, one could have appealed at that time to a 1970 paper by Eller[28] that provides analytical expressions for the viscous, thermal, and radiation loss coefficients for the bubbles at all excitation frequencies. Indeed, a purpose of the present section is to demonstrate that simply by setting $f = (\delta_{\text{vis}} + \delta_{\text{th}} + \delta_{\text{rad}})\omega_0$, where $\omega_0$ is the natural angular frequency of the bubbles, in Eq. (9) of Zabolotakaya and Soluyan's 1973 paper, for all practical purposes one recovers the dispersion relation that is at the core of virtually all subsequent models of acoustic wave propagation in bubbly liquids, including the oft-cited model published in 1989 by Commander and Prosperetti.[29] What small differences remain are typically associated with the ever evolving expressions for the thermal loss factor, owing to the very difficult nature of this problem. It is therefore a mystery why the pioneering contribution by Zabolotskaya and Soluyan is all but ignored in the western literature.

#### 2.2.3.2 Zabolotskaya-Soluyan Model

By assuming the void fraction is small, the authors show that the presence of a uniform distribution of gas bubbles in a liquid can be described by the linear inho-

mogeneous wave equation[25,26] (see also pp. 167–170 in Ref. 30)

$$\nabla^2 p - \frac{1}{c_{\text{liq}}^2}\frac{\partial^2 p}{\partial t^2} = -\rho_0 N_b \frac{\partial^2 v'}{\partial t^2}, \tag{2.26}$$

where $c_{\text{liq}}$ is the sound speed in the liquid without bubbles, $p$ is the sound pressure in the effective fluid, $v' = v - v_0$ is volume change from equilibrium of the gas bubbles, each of which has the same equilibrium volume $v_0$, and $N_b$ is the number of bubbles per unit volume. The right-hand side of Eq. (2.26) is equivalent to a distribution of simple sources having local volume velocity per unit volume $q = N_b \partial v'/\partial t$ [see, e.g., Eq. (D-10) on p. 360 of Ref. 11]. Then enforced is the following simplified form of the Rayleigh-Plesset equation for the bubble dynamics:[31,32]

$$R\ddot{R} + \frac{3}{2}\dot{R}^2 + 4\eta\frac{\dot{R}}{R} = \frac{P_0 - P_\infty}{\rho_{\text{liq}}}. \tag{2.27}$$

In Eq. (2.27), the dots indicate time derivatives (conventional form of the Rayleigh-Plesset equation), $\eta$ is the shear viscosity of the liquid, $P_0$ is the pressure of the gas inside the bubble, and $P_\infty$ is the total pressure far from the bubble. For adiabatic behavior of the gas, letting $P_\infty = P_0 + p$, and retaining only linear terms allows Eq. (2.27) to be rewritten

$$\ddot{v}' + \delta'\omega_0\dot{v}' + \omega_0^2 v' = -\frac{4\pi R_0}{\rho_{\text{liq}}}p, \tag{2.28}$$

where $\omega_0$ is the Minneart frequency of the bubble. Note that Eq. (2.28) has the form of a forced simple harmonic oscillator with natural frequency $\omega_0$ and damping $\delta' = 4\eta/\omega_0\rho_{\text{liq}}R_0^2$.[†] If time-harmonic behavior is assumed, such that $\partial/\partial t \to j\omega$,[‡] then $v'$ may be eliminated from Eqs. (2.26) and (2.28), which yields a homogenous wave equation for propagation through the bubbly liquid in terms of the effective wavenumber $\tilde{k}_{\text{eff}} = \omega/\tilde{c}_{\text{eff}}$,

$$\left(\nabla^2 + \tilde{k}_{\text{eff}}^2\right) p = 0, \tag{2.29}$$

[†]References 24 and 28 use $d$ to denote the damping coefficient and $\delta$ for the damping coefficient at resonance. Here, $\delta$ is used for the general damping coefficient, and $\delta'$ for the damping coefficient evaluated at bubble resonance.

[‡]When a harmonic time dependence is assumed, positive time convention, $p \propto e^{+j\omega t}$ is used.

where the tilde indicates that the effective wavenumber is a complex quantity. Here,

$$\tilde{k}_{\text{eff}}^2 = k_{\text{liq}}^2 + \left(\frac{\rho_{\text{liq}}\omega^2}{K_{\text{bub}}}\right)\frac{\phi}{1-\omega^2/\omega_0^2 + j\delta'\omega/\omega_0} \tag{2.30}$$

is the dispersion relation, where $k_{\text{liq}} = \omega/c_{\text{liq}}$ is the wavenumber for the liquid without bubbles. Rearranging Eq. (2.30) gives an explicit expression for the effective complex phase speed $\tilde{c}_{\text{eff}}$:[30]

$$\tilde{c}_{\text{eff}} = c_{\text{liq}}\left[1 + \left(\frac{K_{\text{liq}}}{K_{\text{bub}}}\right)\frac{\phi}{1-\omega^2/\omega_0^2 + j\delta'\omega/\omega_0}\right]^{-\frac{1}{2}}. \tag{2.31}$$

Note that for $\omega \ll \omega_0$ Eq. (2.31) reduces to Eq. (2.20). For plane waves, $p \propto e^{-j(\omega/\tilde{c}_{\text{eff}})z}$, where $z$ is the direction of propagation. Thus, the frequency-dependent phase speed and attenuation can be extracted from Eq. (2.31) by

$$c_{\text{eff}}(\omega) = \omega/\text{Re}\,\tilde{k}_{\text{eff}} = 1/\text{Re}\,\tilde{c}_{\text{eff}}^{-1} \tag{2.32}$$

$$\alpha_{\text{eff}}(\omega) = -\text{Im}\,\tilde{k}_{\text{eff}} = -\omega\,\text{Im}\,\tilde{c}_{\text{eff}}^{-1} \tag{2.33}$$

respectively. Equations (2.32) and (2.33) are plotted in Fig. 2.5.

Figure 2.5 shows the effect of the damping factor $\delta'$ on the dispersion and attenuation in the bubbly liquid. If no damping effects are included, there is a stop band near bubble resonance in the region

$$1 < \frac{\omega}{\omega_0} < \sqrt{1 + \phi\frac{K_{\text{liq}}}{K_{\text{bub}}}}, \tag{2.34}$$

in which only evanescent waves can exist; see Fig. 2.5(a). The stop band arises because in this frequency range, the right-hand side of Eq. (2.31) is a pure imaginary quantity for $\delta' = 0$. However, as the damping coefficient is increased from zero, propagation occurs around $\omega = \omega_0$, albeit highly attenuated; see Fig. 2.5(b).

While Zabolotskaya and Soluyan specified only viscous damping,[†] contemporary models offered more general treatments of damping mechanisms. Devin had derived

[†]Radiation effects could be included by accounting for fluid compressibility in Eq. (2.27) that governs the motion of the bubble.[33]

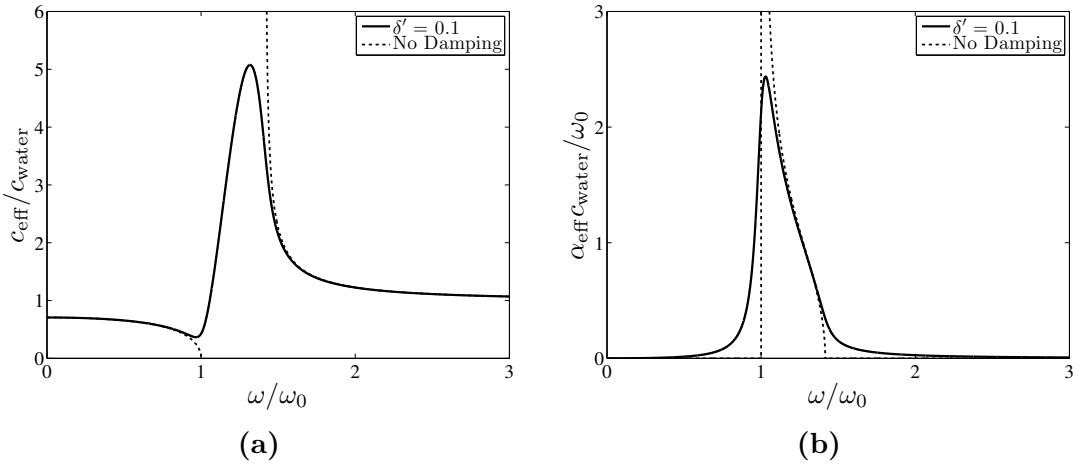


**Figure 2.5:** Predictions of (a) the phase speed and (b) attenuation implied by Eq. (2.30), with no damping (dotted line), and with $\delta' = 0.1$ (solid line). Parameters chosen such that $\phi K_{\rm liq}/K_{\rm bub} = 1$; see Eq. (2.31). After Figs. 6(a) and (b) in Ref. 30.

in 1959 expressions for viscous, thermal, and radiation losses at the natural frequency of the bubble.[34] Eller extended these damping constants to off-resonant behavior in 1970,[28] expressing the result as

$$\delta = \delta_{\rm vis} + \delta_{\rm th} + \delta_{\rm rad}, \tag{2.35}$$

where

$$\delta_{\rm vis} = \frac{4\eta\omega}{3\kappa P_0} = \frac{1}{3}\frac{K_{\rm liq}}{K_{\rm bub}}(k_{\rm liq}R_0)^3 \tag{2.36}$$

$$\delta_{\rm th} = \frac{3(\gamma-1)\left[(R_0/l_D)\left(\sinh R_0/l_D + \sin R_0/l_D\right) - 2\left(\cosh R_0/l_D - \cos R_0/l_D\right)\right]}{(R_0/l_D)^2\left(\cosh R_0/l_D - \cos R_0/l_D\right) + 3(\gamma-1)(R_0/l_D)\left(\sinh R_0/l_D - \sin R_0/l_D\right)} \tag{2.37}$$

$$\delta_{\rm rad} = \frac{\rho_{\rm liq}}{3\kappa P_0}\frac{(R_0\omega)^3}{c_0}. \tag{2.38}$$

In Eqs. (2.36)–(2.38), $l_D = \sqrt{D/2\omega}$ is the thickness of the thermal boundary layer in the bubble, where $D$ is the thermal diffusivity of the gas. The expression in Eq. (2.36), when evaluated at $\omega = \omega_0$, reduces to the quantity $\delta'$ that appears in Eqs. (2.28), (2.30), and (2.31).

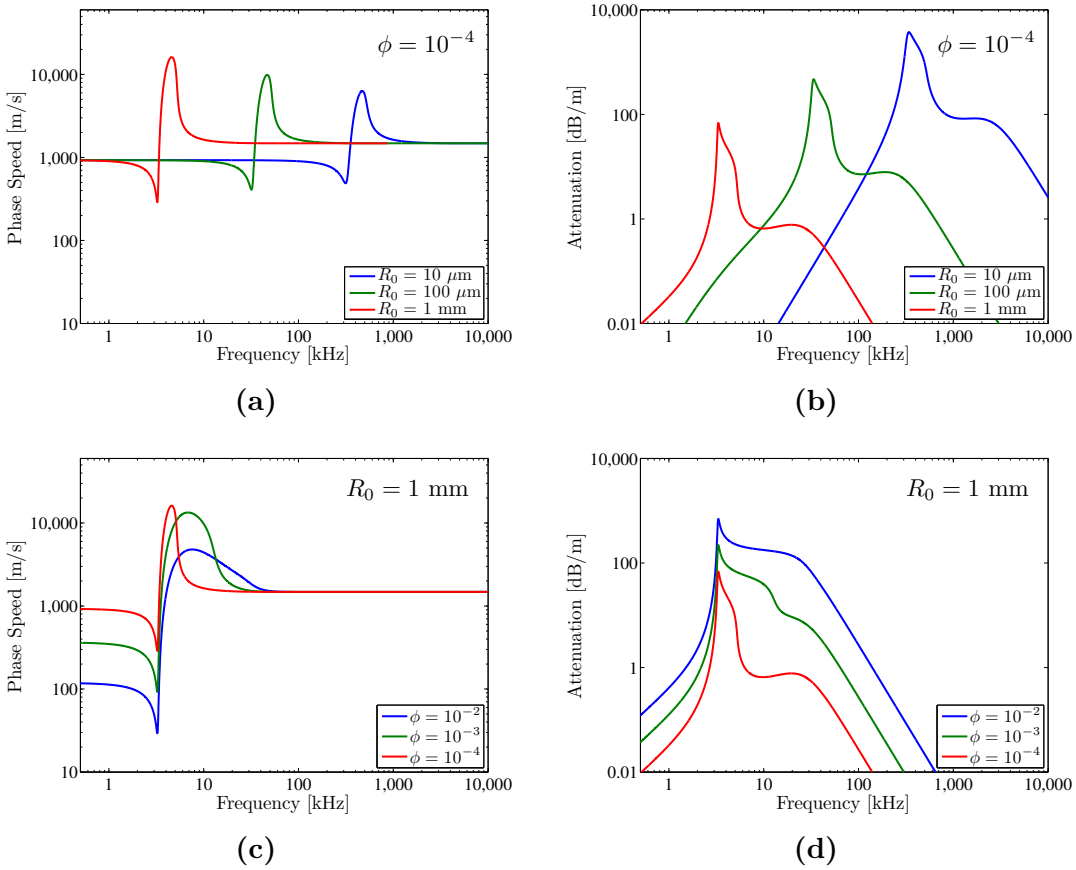


**Figure 2.6:** Predictions of the sound speed and attenuation in bubbly water based on the 1973 effective medium theory of Zabolotskaya and Soluyan with the loss factors as given in the 1970 paper by Eller. For (a) and (b) $\phi = 10^{-4}$ and the indicated bubble radius was used; for (c) and (d) $R_0 = 1$ mm and the indicated void fraction was used.

Use of Eller's damping coefficients, Eqs.(2.36)–(2.38), in conjunction with Zabolotskaya and Soluyan's dispersion relation, Eq. (2.30), will be hereafter referred to as the Zabolotskaya-Soluyan model. Figure 2.6 shows the predictions of the model for effective sound speed and attenuation for several void fractions and bubble radii.

#### 2.2.3.3 Commander-Prosperetti Model

Building on developments by Foldy, van Wijngaarden, and Caflisch et al.,[35–37] Commander and Prosperetti[29] presented a linear model for sound waves in a bubbly

liquid. Using the Keller-Miksis model of radial pulsation[38] as the governing equation for bubble oscillations, they determined

$$\tilde{k}_{\text{eff}}^2 = k_{\text{liq}}^2 + 4\pi\omega^2 \int_0^\infty \frac{R_0/\omega_0^2}{1 - \omega^2/\omega_0^2 + j\delta\omega/\omega_0} n_b(R_0)\, dR_0. \tag{2.39}$$

Here $n_b(R_0)\, dR_0$ is the number of bubbles having equilibrium radii between $R_0$ and $R_0 + dR_0$. The dispersion relation is quite similar to that of Zabolotskaya and Soluyan, Eq. (2.30), except now a distribution of bubble sizes is allowed. However, Zabolotskaya and Soluyan did account for a distribution of bubble sizes in Eqs. (20) and (21) of their 1967 paper,[25] even if their application was specific to parametric amplification of sound waves by way of three-wave nonlinear interaction.

The loss factor $\delta$ is again divided into three terms. While the viscous and thermal damping expressions are quite similar to those of Eller,[24] Eqs. (2.36) and (2.38), the thermal damping term differs more significantly. These terms and the natural frequency $\omega_0$ are calculated in terms of $\Phi$:[†]

$$\delta_{\text{vis}} = \frac{4\eta}{\omega_0 \rho_{\text{liq}} R_0^2} \tag{2.40}$$

$$\delta_{\text{th}} = \frac{(P_0 + 2\sigma/R_0)\text{Im}\,\Phi}{2\omega\omega_0 \rho_{\text{liq}} R_0^2} \tag{2.41}$$

$$\delta_{\text{rad}} = \frac{\omega^2 R_0}{\omega_0 c_0}, \tag{2.42}$$

and

$$\omega_0^2 = \frac{1}{\rho_{\text{liq}} R_0^2} \left[ (P_0 + 2\sigma/R_0)\text{Re}\,\Phi - \frac{2\sigma}{R_0} \right]. \tag{2.43}$$

The authors employ the dimensionless quantity

$$\Phi = \frac{3\gamma}{1 - 3j\chi(\gamma - 1)\left(\sqrt{\frac{j}{\chi}} \coth\sqrt{\frac{j}{\chi}} - 1\right)}, \tag{2.44}$$

[†]Reference 29 uses a dimensional damping term $b = \delta\omega_0/2$, so the form of the dispersion relation appearing here, Eq. (2.39), and damping terms, Eqs. (2.40)–(2.42), have been modified to agree with Eq. (2.30).

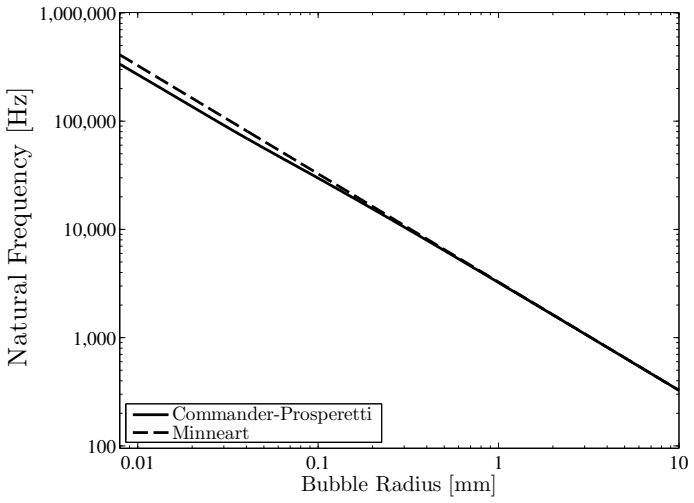


**Figure 2.7:** Comparison of Commander and Prosperetti's expression for the natural frequency of the bubble, Eq. (2.43), to the Minnaert frequency, Eq. (2.23). Calculations are for air bubbles in water.

where $\gamma$ is the ratio of specific heats for the gas in the bubbles, and $\chi$ is defined in terms of the thermal diffusivity $D$ of the gas in the bubbles:

$$\chi \equiv \frac{D}{\omega R_0^2}. \tag{2.45}$$

The form of Eq. (2.43) reflects that fuller treatments result in a more sophisticated model of bubble resonance than Minneart's model. Note that for bubbles with radii larger than 100 $\mu$m, the effects of surface tension are negligible. In this limit, since $\kappa = \mathrm{Re}\,\frac{1}{3}\Phi$, Eq. (2.43) reduces to Minneart's expression, Eq. (2.23) for isothermal (i.e., $\kappa = \gamma$) pulsation. Figure 2.7 shows how these two models differ for air bubbles in water at atmospheric pressure. The differences are most pronounced for small bubbles, where viscous effects and surface tension become important. For millimeter-sized bubbles, which are on the order of the size of the gas bubbles of interest in Chapter 3, the discrepancy between the two models is on the order of a few percent, and thus the Minneart frequency is a reasonable estimate for the onset of highly dispersive behavior.

In this thesis only monodisperse bubble populations are considered, i.e., containing bubbles of one radius $R_0$. In this case, let the variable representing the equilibrium bubble radius be $R_0'$, such that $n_b(R_0') = N_b\delta(R_0' - R_0)$, where $N_b$ is the total bubble density (i.e., the number of bubbles per unit volume). Equation (2.39) thus reduces as follows:

$$\begin{aligned}\tilde{k}_{\text{eff}}^2 &= k_{\text{liq}}^2 + 4\pi\omega^2 \int_0^\infty \frac{R_0'/\omega_0^2}{1 - \omega^2/\omega_0^2 + j\delta\omega/\omega_0} n_b(R_0')\, dR_0' \\ &= k_{\text{liq}}^2 + 4\pi\omega^2 \int_0^\infty \frac{R_0'/\omega_0^2}{1 - \omega^2/\omega_0^2 + j\delta\omega/\omega_0} \left[N_b\delta(R_0' - R_0)\right]\, dR_0' \\ &= k_{\text{liq}}^2 + 4\pi N_b \left(\frac{\omega^2}{\omega_0^2}\right) \frac{R_0}{1 - \omega^2/\omega_0^2 + j\delta\omega/\omega_0}. \end{aligned} \tag{2.46}$$

Since $N_b = \phi \left(\frac{4\pi}{3} R_0^3\right)^{-1}$, and from the Minneart relation, $\omega_0^2 = 3K_{\text{bub}}/\rho_{\text{liq}}R_0^2$, the predicted effective phase speed can be written

$$\tilde{c}_{\text{eff}} = c_{\text{liq}} \left[1 + \left(\frac{K_{\text{liq}}}{K_{\text{bub}}}\right) \frac{\phi}{1 - \omega^2/\omega_0^2 + j\delta\omega/\omega_0}\right]^{-\frac{1}{2}}, \tag{2.47}$$

which is identical to Zabolotskaya and Soluyan's result, Eq. (2.31). The differences between the two models are simply differences in the precise form of $\delta$. Commander and Prosperetti's result includes the effects of surface tension, but this effect is not large for bubbles with radii greater than 100 $\mu$m. Moreover, this difference is a minor detail taken into account through the definition of $\omega_0$

The two models are thus fundamentally the same. To emphasize this point, in Fig. 2.8 are shown the phase speed and attenuation calculated with the 1973 model of Zabolotskaya and Soluyan incorporating the then available 1970 damping coefficients provided by Eller (solid lines). The dashed lines are calculations made with the 1989 model of Commander and Prosperetti. The discrepancies in both the phase speed and attenuation curves are within the scatter in the measurements reported in Commander and Prosperetti. In particular, their reported phase speed measurements are below and above resonance, where there is agreement in the two theories, and their reported attenuation measurements are above 1 dB/m at frequencies below resonance, or in the region of strong attenuation at frequencies near resonance, where the theories are

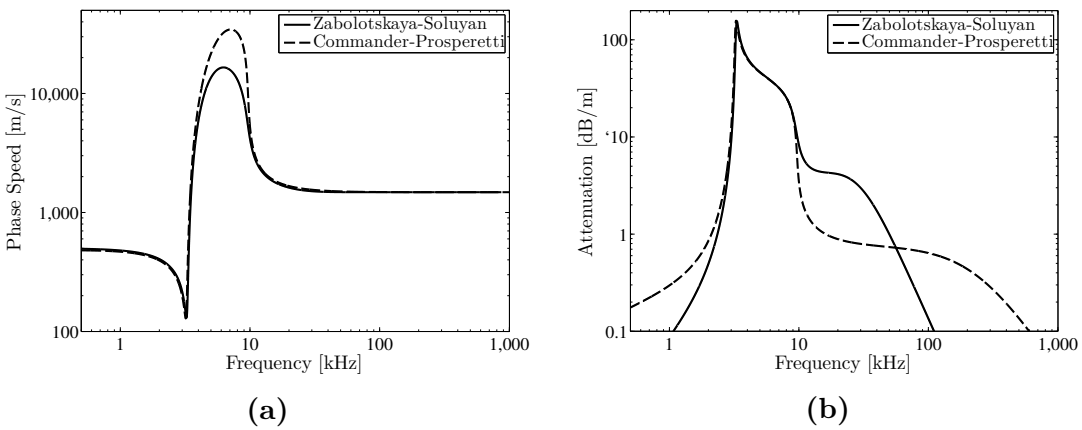


**Figure 2.8:** (a) Predictions of the phase speed given by Eq. (2.31), with Eller's damping coefficients, and Eq. (2.47); (b) Predictions of the attenuation given by the indicated models. For both cases, calculations were made for uniform, 1 mm-diameter air bubbles in water, with a void fraction of $\phi = 10^{-4}$.

in generally good agreement. The discrepancies in the predicted attenuation curves far below and far above resonance are attributed to the advances made in modeling thermal losses since the early work by Devin[34] and Eller.[28] As there appears to be no particular advantage for practical purposes of one model over the other, it is a mystery why the model developed by Zabolotskaya and Soluyan is rarely cited in the western literature, particularly given the widespread acknowledgment of their pioneering contribution in the Russian acoustics literature. The elegant simplicity of their derivation should also be noted.

While use of contrast agents (encapsulated microbubbles) for seismic imaging falls in a frequency range well below any conceivable resonance frequency, where Wood's law is sufficient, a dynamical model is required to interpret results of the resonance tube measurements of bubble compressibility.

### 2.2.4 Reflection from a Layer of Bubbly Liquid

As an example of how gas bubbles affect the reflection of acoustic waves, consider a layer of water with thickness $d$, and containing air bubbles with uniform radii $R_0$

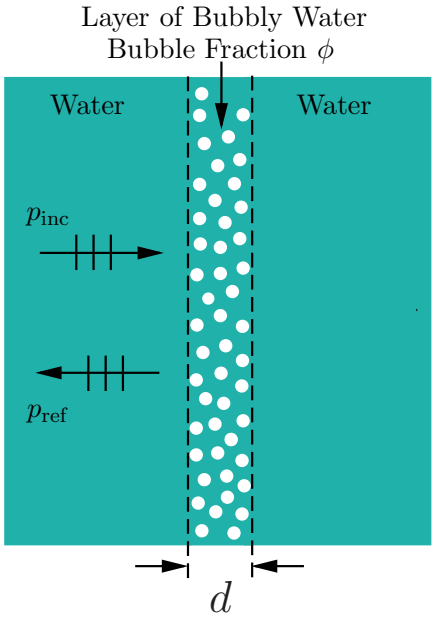


**Figure 2.9:** Assumed geometery of a bubbly-water layer between two half-spaces of water without bubbles. A comparison between expected reflections based on various models is presented in Fig. 2.10.

and void fraction $\phi$. The layer is the region containing bubbles, and the expanses of water on either side of the bubbly layer are taken to be half-spaces; see Fig. 2.9.

The reflection coefficient for a layer between two half-spaces is given by[11]

$$\mathcal{R} = \frac{(1 - Z_1/Z_3)\cos k_{\text{layer}}d + j(Z_2/Z_3 - Z_1/Z_2)\sin k_{\text{layer}}d}{(1 + Z_1/Z_3)\cos k_{\text{layer}}d + j(Z_2/Z_3 + Z_1/Z_2)\sin k_{\text{layer}}d}, \tag{2.48}$$

where $k_{\text{layer}}$ is the wavenumber in the layer, and $Z_i$ is the characteristic impedance of the $i^{\text{th}}$ medium; $Z_2$ is the layer impedance, and $Z_1 = Z_3 = \rho_{\text{water}}c_{\text{water}}$ is the impedance of the water in the two half-spaces.

Two cases are now considered: First, bubble dynamics are ignored, and Wood's law is used to compute the properties of the layer. That is, in Eq. (2.48) set $Z_2 = \rho_{\text{eff}}c_{\text{eff}}$ and $k_{\text{layer}} = \omega/c_{\text{eff}}$, where $\rho_{\text{eff}}$ and $c_{\text{eff}}$ are given by Eqs. (2.14) and (2.17), respectively; the result is indicated by the dashed line in Fig. 2.10. Second, the sound speed and wavenumber in this case are allowed to be complex. Equation (2.48) is evaluated with $\tilde{c}_{\text{eff}}$ given by Eq. (2.31) and $\tilde{k}_{\text{layer}}$ by Eq. (2.30), with Eller's loss factors in Eqs. (2.36)–(2.38), which results in the solid curve in Fig. 2.10. Note that the frequency is normalized by the natural (Minneart) frequency.

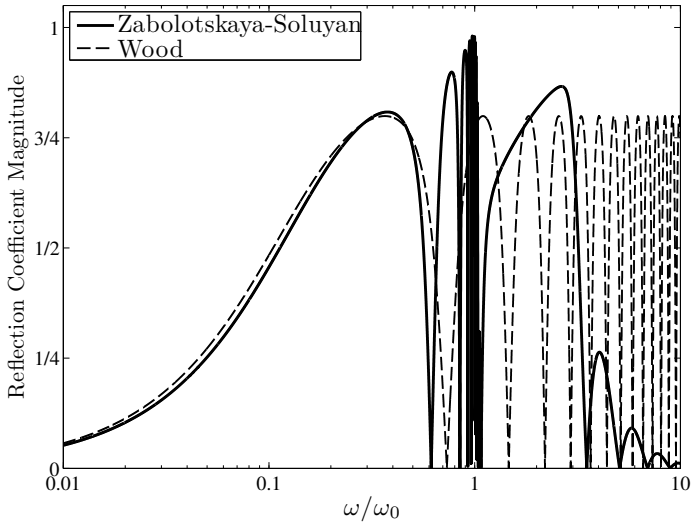


**Figure 2.10:** Pressure reflection coefficient magnitude for a bubbly layer with width $d = 10$ cm, $R_0 = 1$ mm and $\phi = 5 \times 10^{-4}$ as a function of frequency. The dotted line is the result of Eq. (2.48) with Wood's law, and the solid line is that using the Zabolotskaya-Soluyan model with Eller's loss factors.

As expected, at lower frequencies (well below bubble resonance), the two models predict very similar behavior. However, as the wavelength within the layer approaches the width of the layer, two phenomena are seen. First, when an integer number of half-wavelengths have length $d$, the layer becomes effectively invisible. This accounts for the periodic dips seen in the dashed line in Fig. 2.10 representing the Wood's law result. Since according to this model the layer properties are independent of frequency, these areas of zero reflection will persist to indefinitely high frequencies. These nulls are visible in the Zabolotskaya-Soluyan result as well (solid line in Fig. 2.10). However, the dependence of the reflection coefficient on frequency is far more complicated. Very erratic behavior is seen right around bubble resonance, and the reflection coefficient approaches unity near $\omega/\omega_0 = 1$.

### 2.2.5 Effects of Pressure

Downhole environments where acoustic contrast is desired usually do not have atmospheric (ground-level) conditions. Thus the effect of pressure on the gas bubbles

is now considered, namely how the pressure alters the volume of the bubble. If the ambient pressure is increased, the gas in the bubble is compressed, causing the bubble to become both smaller and stiffer, and to occupy a smaller portion of the total volume. Thus, the values $K_{\text{bub}}$, $\rho_{\text{bub}}$, and $\phi$ must be altered to account for this compression.

#### 2.2.5.1 Wood's Law at Elevated Pressure

As shown in Appendix A, expressions for the bulk modulus, density, and void fraction of the gas bubbles[†] are conveniently written as functions of the compression ratio $\beta \equiv v/v_0 = (R/R_0)^3$:

$$K_{\text{bub}} = \frac{1}{\beta} K_{\text{bub},0} \tag{2.49}$$

$$\rho_{\text{bub}} = \frac{1}{\beta} \rho_{\text{bub},0} \tag{2.50}$$

$$\phi = \beta \phi_0, \tag{2.51}$$

where

$$\beta = \frac{1}{1 + \Delta P / K_{\text{bub},0}}. \tag{2.52}$$

Here, $\Delta P = P - P_0$ is the hydrostatic pressure increment. In Eqs. (2.49)–(2.52), the 0 subscript indicates the value of the parameter at atmospheric conditions. Isothermal compression of the bubble is assumed, and no diffusion of gas into the surrounding liquid is included.

For frequencies far below bubble resonance, the sound speed is given by Wood's law. Substituting Eqs. (2.49)–(2.51) into Eq. (2.17) gives

$$c_{\text{eff}}(\beta) = \left[ \frac{\left( \frac{\beta^2 \phi_0}{K_{\text{bub},0}} + \frac{1 - \beta\phi_0}{K_{\text{water}}} \right)^{-1}}{\phi_0 \rho_{\text{bub},0} + (1 - \beta\phi_0)\rho_{\text{water}}} \right]^{\frac{1}{2}}. \tag{2.53}$$

[†]These expressions also hold for bubbles with a shell (contrast agents), provided the material properties of the shell do not vary with pressure; see Appendix A.

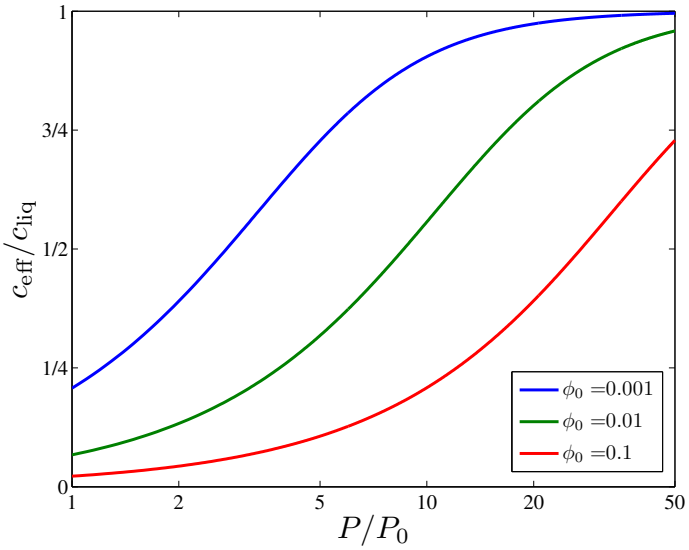


**Figure 2.11:** Effective sound speed, given by Eq. (2.53) for air bubbles in water with various initial void fractions. The compression factor $\beta$ is given by Eq. (2.52).

Equation (2.53) is plotted in Fig. 2.11 for various initial void fractions. As the hydrostatic pressure increases, the gas bubbles are compressed, making them both smaller and stiffer. These two effects conspire to cause the reduction in sound speed from that of the liquid to become smaller as the pressure is increased significantly.

#### 2.2.5.2 Sound Speed Dependence on Depth and Void Fraction

As an exploration of the parameter space, Fig. 2.12 shows low-frequency sound speed in bubbly water as a function of both depth and void fraction. Here, the void fraction at that pressure is specified, rather than computed from Eq. (2.51) from an initial void fraction. The pressure is taken to be that expected at the indicated depth $z$ under water:

$$P = P_0 + \rho_{\rm water} g z, \tag{2.54}$$

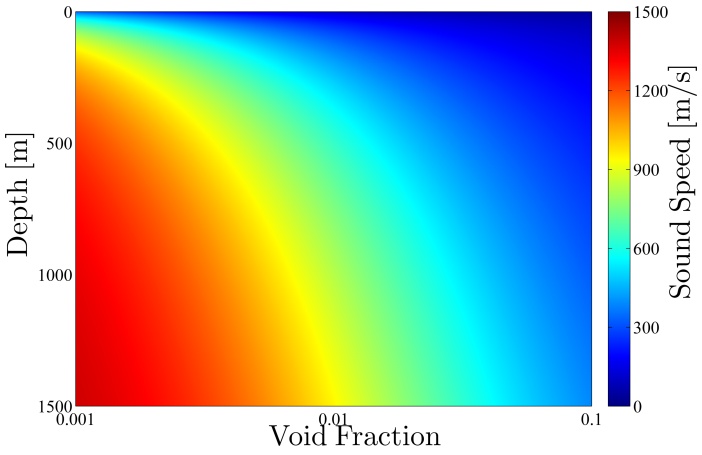


**Figure 2.12:** Effective sound speed, given by Eq. (2.53) for air bubbles in water. The depth is taken to be under water, such that pressure above ambient is given by $\Delta P = \rho_{\text{water}} g z$.

where the atmospheric pressure $P_0 = 1.01 \times 10^5$ Pa, and $g = 9.81$ m/s$^2$ is the acceleration due to gravity. The properties of water[†] were taken to be invariant with depth. At atmospheric pressure, the sound speed is reduced from that of water to below 300 m/s for all void fractions between $10^{-3}$ and $10^{-1}$. However, as the depth, and thus the hydrosatic pressure increases, the change in sound speed is much less at those same void fractions. For example, from Fig. 2.12 at 1 km depth, for a void fraction of 0.01, Eq. (2.53) predicts a sound speed of about 900 m/s, whereas the predicted sound speed for a void fraction of 0.01 at atmospheric presure is close to 150 m/s.

#### 2.2.5.3 Reflection from a Bubbly Layer at Depth

The bubbly layer calculation in Section 2.2.4 is now repeated with the effects of the elevated hydrostatic pressure at depth included in the layer properties. The geometery is again that shown in Fig. 2.9. The layer thickness is 10 cm, the frequency fixed at 2 kHz, and the void fraction is varied. The reflection coefficient is computed

[†]All water properties for these calculations were those in Table 2.1, which are the values for fresh water. For calculations under an equivalent depth of salt water, the water properties need to be adjusted accordingly.

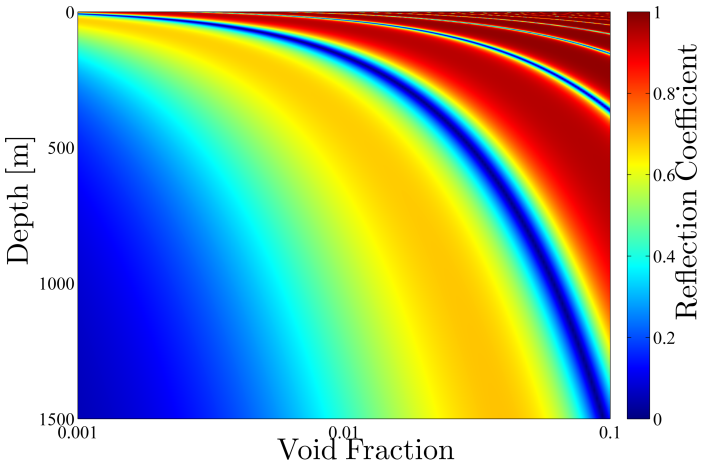


**Figure 2.13:** Reflection coeficient magnitude from a bubbly layer, from Eqs. (2.48) and (2.53), for air bubbles in water. The depth is taken to be under water, such that pressure above ambient is given by $\Delta P = \rho_{\text{water}} g z$. The layer thickness is taken to be 10 cm, and the frequency is taken to be $f = 2$ kHz.

from Eq. (2.48), and no bubble dynamics are considered. That is, the wavenumber in the layer is calculated from $k_{\text{layer}} = \omega / c_{\text{eff}}$, where $c_{\text{eff}}$ is given by Eq. (2.53). Since the interrogation frequency is 2 kHz, Wood's law, and thus the results shown in Fig. 2.13, is applicable provided the bubble radius is less than 1 mm at atmospheric pressure.

As the magnitude of the reflection coefficient nears unity (red) at atmospheric pressure (the top of Fig. 2.13), it becomes much smaller as the depth increases. The blue striations are due to the half-wavelength effect that was seen in Fig. 2.10; that is, the reflection coefficient vanishes (dark blue) when $k_{\text{layer}} = n\pi$ as the layer becomes trasnparent. As the depth increases, the bubbles become stiffer, and, since the frequency is fixed, a larger void fraction is needed to provide the same effective sound speed (wavenumber) in the layer. Thus, the void fractions at which the reflection coefficent becomes 0 become larger as the depth increases.

#### 2.2.5.4 Reflection from a Bubbly Water/Oil Interface at Depth

With the density and sound speed in bubbly water having been determined as a function of pressure, an estimation is made of the effect of the bubbly water on

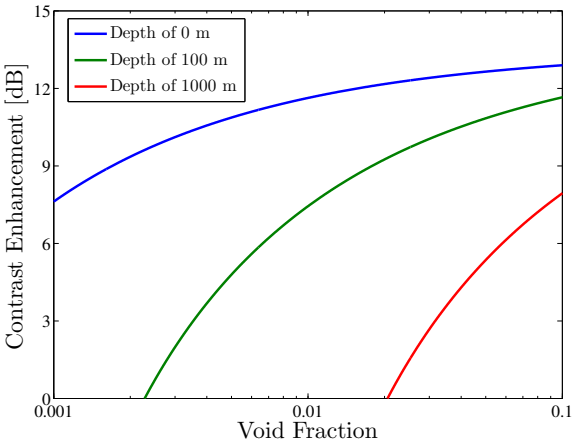


**Figure 2.14:** Contrast enhancement due to gas bubbles from an oil/water interface, as a function of the void fraction in the water. Here the contrast enhancement is the difference between the reflection coefficient with bubbles in the water and with no bubbles, expressed in decibels.

reflection from an oil/water interface. The reflection coefficient from the interface between two half-spaces is[11]

$$\mathcal{R} = \frac{Z_2 - Z_1}{Z_2 + Z_1}, \tag{2.55}$$

where $Z_1$ is the specific acoustic impedance of the half-space in which the incident wave is travelling, and $Z_2$ is that of the half-space from which reflection is sought. In decibels, the reflection coefficient is expressed as $\mathcal{R}_{\text{dB}} = 20 \log_{10} |\mathcal{R}|$. For the interface between half-spaces of water and oil this quantity is about $\mathcal{R}_{\text{dB}} \simeq -13$ dB, meaning the reflected signal will be about 13 dB lower than the incident signal. Thus contrast enhancement of 13 dB would indicate a reflection coefficient of unity. Plotted in Fig. 2.14 is the contrast enhancement, defined as the level of the signal reflected from the oil/bubbly water interface above what it would be with no gas bubbles in the water. Again, no bubble dynamics are considered, and so the result is valid for $\omega \ll \omega_0$.

It can be seen that at atmospheric pressure (blue line) the reflection from the oil/bubbly water interface is about 10 dB higher when the water contains 1% bubbles than when the water does not contain bubbles. Although unrealistic in practice, note

that the blue curve reaches 13 dB for a void fraction of 10%. This comes about because in this case the magnitude of the reflection coefficient is approximately unity, and the bubbles thus compensate completely for the low reflectivity of a water/oil interface. At depths of 100 m and 1,000 m (green and red lines, respectively) the contrast enhancement becomes negative at lower void fractions. Because the addition of bubbles lowers the bulk modulus of the water, and since the bulk modulus of water is slightly higher than that of oil, for smaller void fractions and at higher pressures, the bubbles make the impedance of the bubbly water closer to that of oil. As the void fraction becomes large ($\phi \simeq 0.1$), the impedance of water becomes significantly less than that of oil for all depths shown, and the reflection coefficient magnitude becomes larger.

## 2.3 Fluid-Saturated Rock

Since the effective properties of a bubbly liquid may be determined using the models discussed in Section 2.2.3, it remains to find an applicable model for how acoustic disturbances propagate in the fluid-saturated rock, and how the presence of bubbles affects this propagation.

Much like the fluid case, the approach will be to derive effective properties for the entire rock/fluid/bubble structure. For an infinite, homogeneous, elastic solid, the compressional waves, or P waves, travel with velocity[39]

$$V_P = \sqrt{\frac{K + \frac{4}{3}\mu}{\rho}}, \tag{2.56}$$

where $\mu$ is the shear modulus of the material. The introduction of a shear modulus allows for independent transverse motion. These S waves propagate with velocity

$$V_S = \sqrt{\frac{\mu}{\rho}}. \tag{2.57}$$

Since bubbles affect only the properties of the fluid in the pores of the rock, the shear modulus $\mu$ is unchanged by the bubbles. Therefore, the alteration of $K$ due to the

bubbles is the dominant effect. The relevant impedance is the P-wave impedance, defined by[40]

$$Z = \rho V_P. \tag{2.58}$$

### 2.3.1 Biot Theory

Much like the effective medium models discussed in Section 2.2.3, Biot theory relies on statistical averaging. Porous rock generally has complex internal structure, and modeling these complexities would require knowlege of pore shapes, mineral grain stucture, and pore fluid distributions, among other parameters. Even if this information is known *a priori* (and in practice it is not), the computational expense of using such a model would likely be prohibitive.

Instead, Biot considered a statistically isotropic porous solid volume element.[†] Analysis is restricted to low frequencies, such that the wavelengths are much longer than the pore size.[‡] By calcuating the stresses and strains on each face of the element, on both the solid and fluid elements, and then decoupling the rotational (shear) and compressional parts of the field, Biot found two wave equations for compressional elastic motion [Eq. (6.7) in Ref. 41]. The two wave equations correspond to two distinct modes of propagation. By assuming time-harmonic planar motion, Biot shows that these compressional waves travel with velocities

$$V_{P,1} = \frac{V_B}{\left|\mathrm{Re}\,\sqrt{z_1}\right|} \tag{2.59}$$

and

$$V_{P,2} = \frac{V_B}{\left|\mathrm{Re}\,\sqrt{z_2}\right|}, \tag{2.60}$$

[†]In this case, "statistically isotropic" means that the relative volume of the pores in a cross-sectional slab of the porous solid of thickness $dx$ would be equal to the porosity ($\Omega$), regardless of where along $x$ the slab was taken

[‡]Biot's explicit frequency limit is $f < \pi\eta_f/4\rho_f d_{\mathrm{pore}}^2$, where $d_{\mathrm{pore}}$ is the pore diameter, $\rho_f$ and $\eta_f$ are the density and viscosity of the pore fluid, respectively, such that turbulent and nonlinear flow may be neglected. For reference, if the pore fluid is water and the pore diameter is $\sim 100$ $\mu$m, then the model requires $f \lesssim 8$ kHz.

where $V_B$ is a reference velocity given by

$$V_B = \sqrt{\frac{\lambda + 2\mu + R_B + Q_B}{\rho_{\text{eff}}}}, \tag{2.61}$$

and $R_B$ and $Q_B$ describe the coupling between the two media. The quantities $z_1$ and $z_2$ are the complex roots to a characteristic equation [Eq. (7.22) in Ref. 41], and depend on the solid and fluid properties of the medium.

Since $z_1$ is chosen to be the smaller of the two roots, such that $|z_1| < |z_2|$, the disturbance that travels with speed $V_{P,1}$ is termed the compressional wave of the first kind (or fast compressional wave). Similarly the disturbance that travels with speed $V_{P,2}$ is termed the compressional wave of the second kind (or slow compressional wave). The slow compressional wave describes motion in the solid where the solid frame and pore fluid move out of phase with each other. The slow wave corresponds to antiphase motion. It is severly attenuated, even at relatively low frequencies, and was not detected experimentally until nearly a quarter of a century after Biot's theory was published.[42†]

Figure 2.15 shows plots of the normalized velocity and attenuation for the fast and slow waves (solid and dashed lines, respectively). The solid is taken to have porosity of $\Omega = 0.2$, which is a typical value for the rock types considered in Section 2.3.2, and to be water-saturated. For very low frequencies, the fast wave travels at nearly exactly $V_B$ and the velocity of the slow wave approaches zero. Similarly, the fast wave is attenuated negligibly at lower frequencies, whereas the slow wave experiences appreciable attenuation at relatively low frequencies. The plots use normalized parameters: $V_B$ for velocity from Eq. (2.61); $f_B$ for frequency from Eq. (7.4)

[†]Biot predicts no second shear wave. While no shear motion is considered here, calculations will involve the shear modulus and shear wave velocity of the saturated rock. These values have their usual connotations and do not change due to the addition of bubbles to the pore fluid, which itself is assumed to have a negligible shear modulus. Other models extend Biot's theory to higher frequencies by acounting for local flow of the fluid between the pores. These so-called "squirt models" do predict a slow S-wave whose dissipative effects are typically more important than those of the slow P wave.[40, 43]

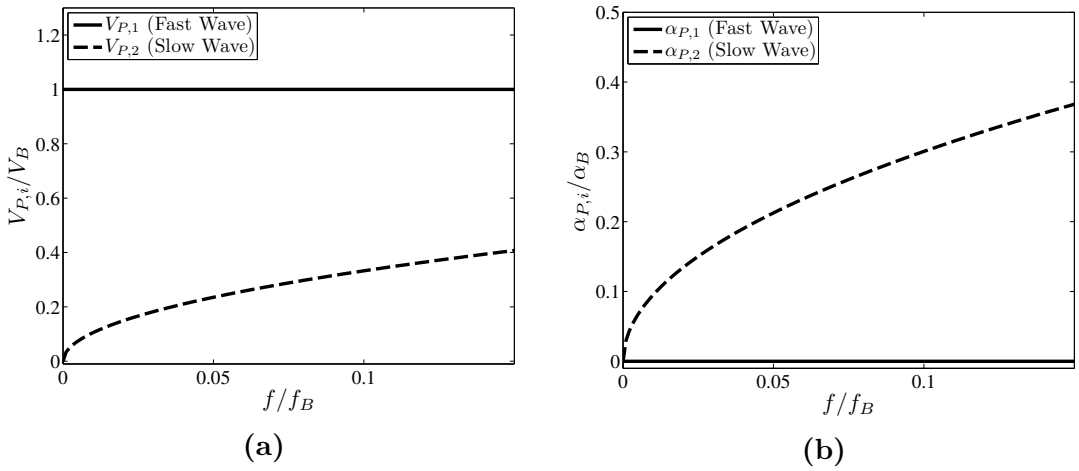


**Figure 2.15:** (a) The normalized propagation velocity and (b) normalized attenuation of the fast and slow waves that satisfy Eq. (6.7) in Ref. 41. The plots are for a water-filled elastic solid with porosity $\Omega = 0.2$, corresponding to a typical stress profile given by Case 1 in Table 1 of Ref. 41.

of Ref. 41; and a characteristic attenuation $\alpha_B = 2\pi f_B/V_B$. The nature of the propagation depends on many properties of the solid and fluid phases, which have been estimated and applied mostly for convenience. Thus Fig. 2.15 represents only the general behavior of such waves, and not any specific numerical prediction.

The remainder of this thesis is concerned only with the fast compressional waves, which correspond to in-phase motion of the fluid and solid components, and so the subscipt will henceforth be implicit, i.e.,

$$V_P = V_{P,1}. \tag{2.62}$$

In other words, limiting behavior is now assumed, such that the coupled fluid and elastic phases behave as a single medium with effective properties (much as was done for bubbly water).

### 2.3.2 Gassmann's Equation

A quasi-static treatment of poroelastic behavior was published by Gassmann in 1951. The expressions below are a zero-frequency limit of Biot's more general model.

The so-called Gassmann-Biot equation gives the bulk modulus of saturated rock with a known pore fluid:[44–46]

$$\frac{K_r}{K_{\text{min}} - K_r} = \frac{K_{\text{dry}}}{K_{\text{min}} - K_{\text{dry}}} + \frac{K_f}{\Omega(K_{\text{min}} - K_f)}, \tag{2.63}$$

where $K_r$ is the bulk modulus of the saturated rock, $K_{\text{min}}$ is the mineral bulk modulus (i.e., the rock material itself without pores), $K_f$ is the bulk modulus of the pore fluid, $\Omega$ is the porosity of the rock, and $K_{\text{dry}}$ is the bulk modulus of the dry rock frame. Since extracting an effective bulk modulus for the entire saturated porous medium necessarily requires simplifications to be made, Eq. (2.63) is valid only with several caveats:[40]

1. Acoustic propagation is at low frequencies, such that the pore fluid has time to equilibrate, and there is effectively no pressure gradient within the pores.
2. The rock medium is homogeneous, isotropic, and linearly elastic.
3. The pores are statistically isotropic.
4. The pores are uniformly and completely saturated with the pore fluid.

For seismic imaging, the first condition is met. The further restrictions are generally valid assumptions, at least to a degree that Eq. (2.63) becomes a useful approximation. It is also worth noting that no knowledge of the specific pore geometery is required. That is, as long as the pores are relatively uniform on average, their shapes and sizes may be arbitrary.[40]

#### 2.3.2.1 Fluid Substitution

While the dry frame bulk modulus $K_{\text{dry}}$ may be calculated, available parameters often make it easier, and more useful, to perform a fluid substitution and calculate the predicted change in the bulk modulus of the saturated rock instead. That is, $K_{\text{dry}}$ in Eq. (2.63) is eliminated by substituting moduli for two different fluids ($K_{f1}$ and $K_{f2}$)

and two resulting bulk moduli of the saturated rock ($K_{r1}$ and $K_{r2}$). Doing so and equating (since $K_{\rm dry}$ and $K_{\rm min}$ do not depend on the pore fluid) gives the following relation for the bulk modulus of the rock saturated with the second fluid:

$$K_{r2} = K_{\rm min}\left\{1 + \left[\frac{1}{\Omega}\left(\frac{1}{K_{\rm min}/K_{f2} - 1} - \frac{1}{K_{\rm min}/K_{f1} - 1}\right) + \frac{1}{K_{\rm min}/K_{r1} - 1}\right]^{-1}\right\}^{-1}. \tag{2.64}$$

At low frequencies, the bulk modulus of the new pore fluid (bubbly water) is given by Wood's law[14] (see Section 2.2.1). For a given void fraction $\phi$, the effective bulk modulus of the gas-fluid mixture is

$$K_{f2} = \left(\frac{\phi}{K_{\rm bub}} + \frac{1-\phi}{K_{f1}}\right)^{-1}. \tag{2.65}$$

Equation (2.64) thus becomes

$$K_{r2} = K_{\rm min}\left\{1 + \left[\frac{1}{\Omega}\left(\frac{1}{(1-\phi)K_{\rm min}/K_{f1} + \phi K_{\rm min}/K_{\rm bub} - 1} - \frac{1}{K_{\rm min}/K_{f1} - 1}\right) + \frac{1}{K_{\rm min}/K_{r1} - 1}\right]^{-1}\right\}^{-1}. \tag{2.66}$$

See Appendix B for derivations of Eqs. (2.64) and (2.66).

### 2.3.3 Air Bubbles in Water-Saturated Limestone

Equation (2.66) gives the effective bulk modulus of the bubbly-liquid saturated rock as a function of the bulk modulus of the liquid and bubbles inside its pores. If the water-saturated bulk modulus is known (i.e., the bulk modulus with no bubbles in the pore liquid), then a comparison between the two provides a reasonable estimation of the degree to which the bubbles change the specific acoustic impedance of the rock-water-bubble medium. As an example, the contrast provided by air bubbles in limestone[†] is calculated.

[†]Limestone was chosen for example calculations because it has a mineral bulk modulus ($K_{\rm min} \simeq$ 70 GPa) that is near the average of typical values. The relative changes in bulk modulus $K_r$ are larger for a harder mineral, such as dolomite ($K_{\rm min} \simeq$ 95 GPa), and smaller for a softer mineral such as sandstone ($K_{\rm min} \simeq$ 35 GPa).

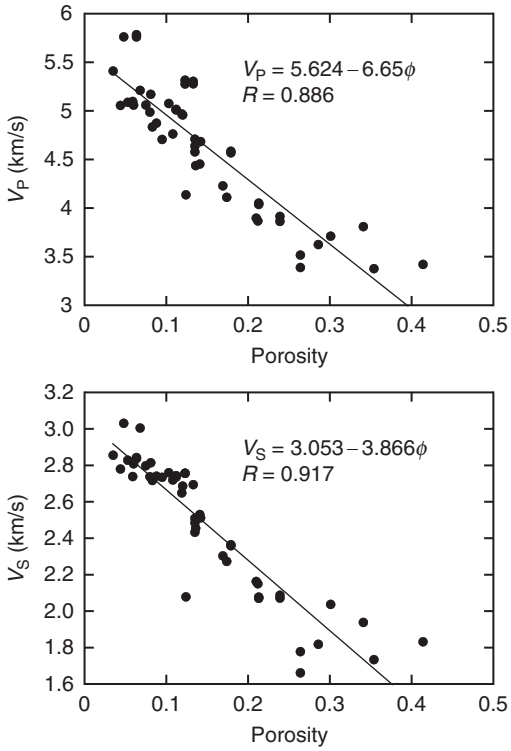


**Figure 2.16:** Plot of measured P- and S-wave speeds for water-saturated limestone, and the empirical fit used for the calculations in this section. Plot reprinted from Ref. 40.

Empirical formulas for the saturated P-wave velocities for various rock types ($V_P^{r1}$) are given in Ref. 40 as functions of porosity, and it was from these values that $K_{r1}$ was extracted;[†] see Fig. 2.16. For limestone, the P-wave velocity is given by

$$V_P^{r1} = 5624 - 6650\,\Omega \text{ m/s}. \tag{2.67}$$

Assuming that the bubbles cause no change in shear modulus, then the new P-wave velocity is given by[44]

$$V_P^{r2} = \sqrt{\frac{K_{r2} + \frac{4}{3}\mu_r}{\rho_{r2}}}. \tag{2.68}$$

Here, $\mu_r$ is the shear modulus of the rock, and $\rho_{\text{eff}}$ is an effective density acounting for the pore fluid content.[47,48] Empirical data for the correlation between the water-saturated density $\rho_{r1}$ and P-wave velocity in Ref. 40 are also available. Thus, $\rho_{r1}$ is

[†]Since $K_{r1} = \rho_{\text{r1}} \left(V_P^{r1}\right)^2 - \frac{4}{3}\mu_r$, where $\mu_r = \rho_{\text{r1}} \left(V_S^{r1}\right)^2$. The S-wave speed was taken from a similar relation, $V_S^{r1} = 3053 - 3866\,\Omega$ m/s for limestone.

used for the water-saturated case, and the effective density, accounting for the density of the bubbles, is

$$\rho_{r2} = \rho_{r1} - \Omega\phi(\rho_f - \rho_{\text{bub}}), \tag{2.69}$$

where $\rho_f$ is density of the original pore fluid (water in this case).

The sequence of calculations is as follows:

1. With the empirical data from Ref. 40 for $V_P^{r1}$, $V_S^{r1}$, and $\rho_{r1}$, the water-saturated bulk modulus $K_{r1}$ can be calculated from Eq. (2.56).

2. Equations (2.66) and (2.65) are used to find $K_{r2}$, the bulk modulus of the rock saturated with the bubbly liquid.

3. The effective density for the rock with bubbly liquid, $\rho_{r2}$, is given by Eq. (2.69).

4. Once $K_{r2}$ and $\rho_{r2}$ are known, the P-wave velocity $V_{r2}$ and impedance $Z_{r2}$ can be determined and compared with the corresponding no-bubble cases.

The effective bulk modulus of the rock saturated with bubbly water has a lower limit, reached when $\phi = 1$. In this limit, the pores are filled entirely with air, and so $K_{r2} \simeq K_{\text{dry}}$.[†] An explicit expression for the dry frame modulus can be found from Biot theory:[49]

$$K_{\text{dry}} = \frac{K_{r1}\left[(1-\Omega) + \Omega K_{\text{min}}/K_{f1}\right] - K_{\text{min}}}{\Omega K_{\text{min}}/K_{f1} + K_{r1}/K_{\text{min}} - (1+\Omega)}. \tag{2.70}$$

With the current parameters for limestone, Eq. (2.70) gives $K_{\text{dry}} = 23.6$ GPa. Comparing this result with Eq. (2.66) yields good agreement: for a porosity of $\Omega = 0.2$, $K_{r1} = 27.9$ GPa, and in Fig. 2.17, a gas fraction of $\phi = 1$ indicates a resultant bulk modulus about 15% lower than $K_{r1}$ (green curve). This gives $(1 - 0.15)K_{r1} = 23.7$ GPa, which is very close to the result obtained for $K_{\text{dry}}$ from Eq. (2.70).

[†]It is important to note that the bulk modulus of the rock with gas-filled pores is not the same as the dry frame modulus. As the pores are deformed, there will be some stiffness due to the air. At atmospheric pressures, this air stiffness is negligible, and so $K_{r2}(\phi = 1) \simeq K_{\text{dry}}$. However, in general, and especially at higher pressures, gas-filled pores may well contribute to the overall stiffness.

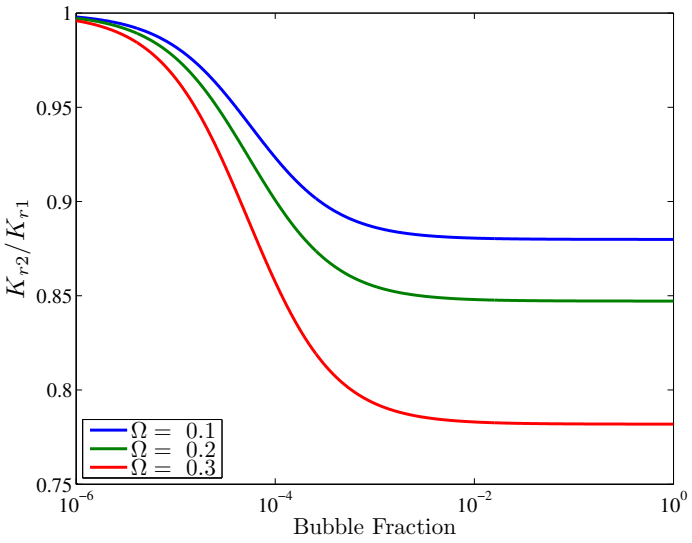


**Figure 2.17:** Plot of the bulk modulus of saturated limestone with bubbly water as the pore fluid, $K_{r2}$, normalized by the bulk modulus of the saturated rock with no bubbles, $K_{r1}$. Calculations are for air bubbles under atmospheric conditions, with $K_{\text{bub}} = 101$ kPa.

The value of $K_{\text{dry}}$ is also very close to the value calculated in the example above for the case where the pores contain 1% air bubbles and 99% water. This is due to a saturation effect; as can be seen in Fig. 2.17, the minumum modulus, $K_{\text{dry}}$, is reached for relatively low gas fractions at atmospheric pressure. If the pressure were increased, then a larger gas fraction would be required for $K_{r2}$ to approach $K_{\text{dry}}$, since the air is less compliant at higher pressures. While this approach neglects many of the complexities specific to limestone, the calculated values are reasonably close to experimental results.[49–52]

Unlike the bulk modulus, the compressional wave speed (Fig. 2.18) is not bounded by $V_P^{r1}$ and $V_P^{\text{dry}}$. For $\phi < 10^{-2}$, the density of the pore fluid remains nearly constant. Therefore, the P-wave velocity depends only on the bulk modulus of the saturated rock, $K_{r2}$, and so Figs. 2.17 and 2.18 are similar in this region. However, as the gas fraction $\phi$ increases, the effective density decreases (since air is less dense than water). This causes the P-wave velocity to become larger until the pores are completely air-filled. This limit corresponds to the dry-frame P-wave velocity, $V_P^{\text{dry}}$. Note that the

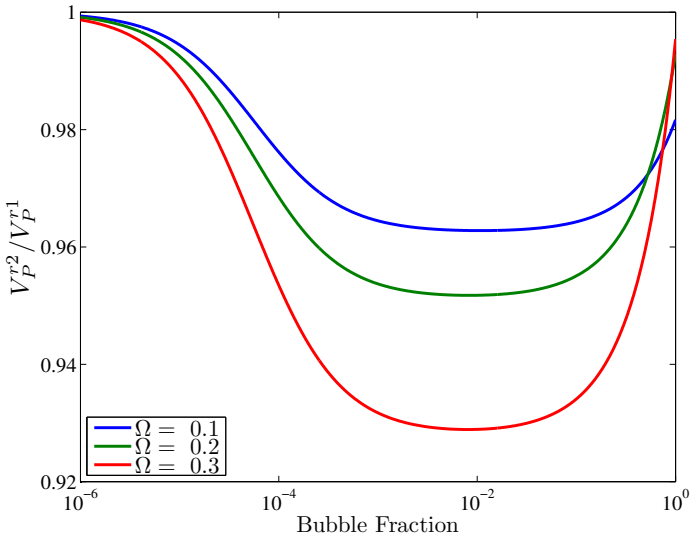


**Figure 2.18:** Plot of the P-wave velocity in limestone with bubbly water as the pore fluid, $V_P^{r2}$, normalized by the velocity in the water-saturated rock with no bubbles, $V_P^{r1}$. Calculations are for air bubbles with $K_{\text{bub}} =$ 101 kPa.

minimum predicted P-wave velocity in the saturated rock is not the dry-frame speed $V_P^{\text{dry}}$. Rather, it occurs at some intermediate point where the gas fraction is large enough to reduce the pore fluid compressibility, but not so large that it begins to significantly reduce the overall density.

Finally, the plane-wave impedance of the saturated rock is given by[40]

$$Z_r = \rho_r V_P^r. \tag{2.71}$$

While $Z_r$ is proportional to the product of the P-wave velocity, which increases as the gas fraction approaches 1, and the density, which decreases over that same interval, the drop in density is faster than the rise in P-wave velocity. Thus the impedance decreases monotonically with $\phi$, though its intermediate behavior is not uniform. Figure 2.19 shows the change in impedance $Z_r$ as a function of the gas fraction, again normalized by the no-bubble case.

From Fig. 2.19, it is clear that the minimum impedance does occur for the case where the pores are completely air filled. That is, the minimum impedance is the

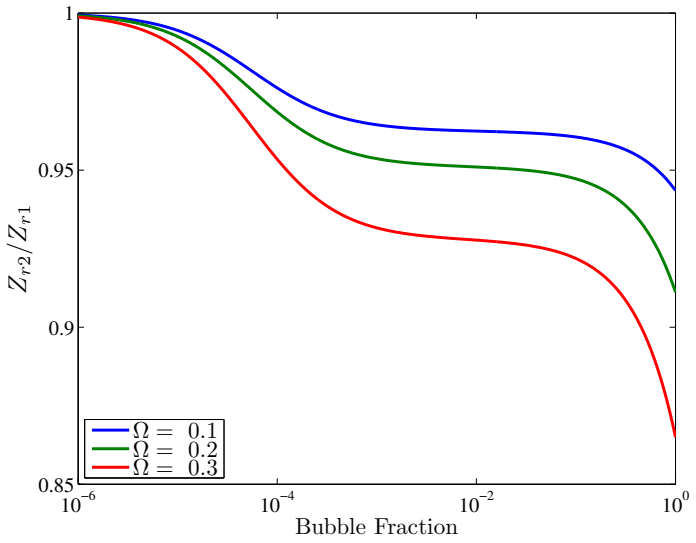


**Figure 2.19:** Plot of the specific acoustic impedance of limestone with bubbly water as the pore fluid, $Z_{r2}$, given by Eq. (2.71), normalized by the saturated rock impedance with no bubbles, $Z_{r1}$. Calculations are for air bubbles with $K_{\text{bub}} = 101$ kPa.

dry-frame case. However, completely filling the pores with bubbles is not practical. If instead it is assumed that the gas bubbles comprise 1% of the pore fluid, then Fig. 2.19 indicates about a 5% decrease in impedance, for a porosity of $\Omega = 0.2$.

#### 2.3.3.1 Validity of Fluid Substitution Results

The complexity of anisotropic, poroelastic materials, coupled with intricacies of real geologic conditions is the motivation for the use of simplified relations like Gassmann's equation. Therefore, results from these calculations must be considered in the context of these limitations. Due to all of the assumptions underlying the fluid-substitution models, an estimate the reasonableness of their results is warrented.

If all particles in a rock/fluid mixture are under the same pressure (stress), then the effective bulk modulus is given by the Reuss average[53]

$$\frac{1}{K_{\text{eff,R}}} = \sum_{i=1}^{N} \frac{\phi_i}{K_i}. \tag{2.72}$$

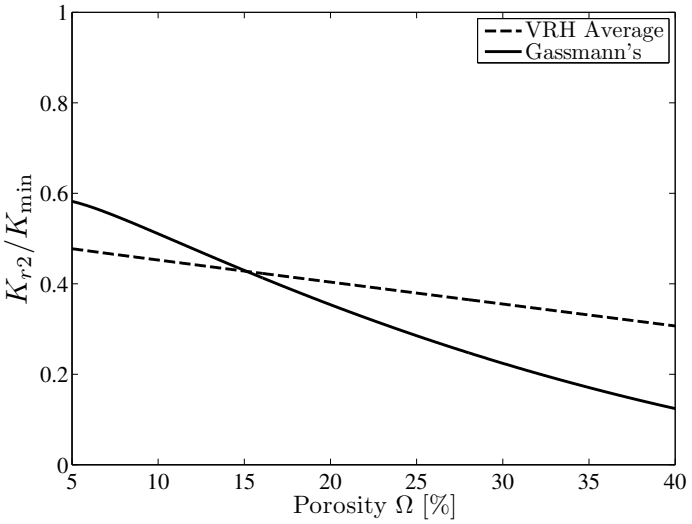


**Figure 2.20:** Plot of the bulk modulus of the rock saturated with bubbly water, $K_{r2}$, computed with both the VRH average, Eq. (2.74), and the fluid substitution method, Eq. (2.64). Plot is for limestone with 1% air bubbles at atmospheric conditions, and $K_{r2}$ is normalized by the mineral bulk modulus. Porosity shown $\Omega \in (5\%, 40\%)$ is in the range over which an empircal fit was made in Fig. 2.16.

If instead all constituents are assumed to have the same resulting displacement, then the effective bulk modulus is given by the Voigt average[54]

$$K_{\text{eff,V}} = \sum_{i=1}^{N} \phi_i K_i. \tag{2.73}$$

In 1952, Hill showed that the Reuss and Voigt averages represent lower and upper bounds, respectively, on the effective modulus of the rock.[55] While either extreme is unlikely, an average of the two, the so-called "Voigt-Reuss-Hill (VRH) average", $K_{\text{eff,VRH}}$, can give a "useful and sometimes accurate estimate of rock properties":[40]

$$K_{\text{eff,VRH}} = \frac{K_{\text{eff,R}} + K_{\text{eff,V}}}{2}. \tag{2.74}$$

If the results from the fluid substitution calculations agree with the corresponding VRH average, it may be concluded that the results are reasonable.

While Fig. 2.20 shows some discrepancy between the Gassmann's and VRH-average results, the two are quite similar, both in absolute value and behavior. This

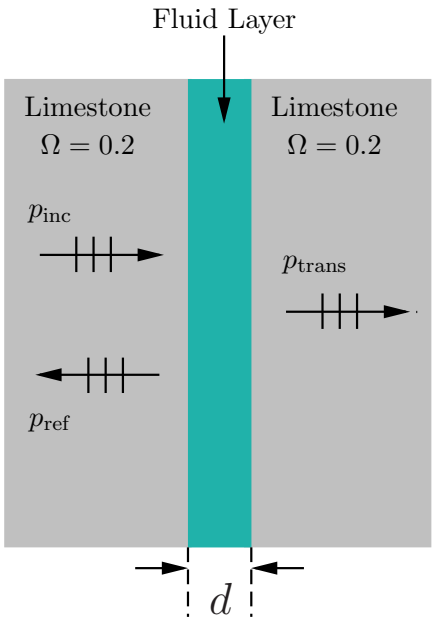


**Figure 2.21:** Geometry of a fluid layer between two half-spaces. A comparison between reflections from a pure water layer and a bubbly water layer is shown in Fig. 2.22. The limestone is taken to be fully saturated with water.

agreement over the porosities of interest indicates that results from use of the fluid substitution technique are not unreasonable.

### 2.3.4 Bubbly Liquid Layer in Rock

It is also of interest to examine how the presence of bubbles affects the propagation of a compressional wave incident upon a fluid layer. The imagined geometry consists of two half-spaces of saturated rock, separated by a fluid layer of width $d$; see Fig. 2.21. For these calculations, the rock is taken to be water-saturated limestone with a porosity of 20% ($\Omega = 0.2$), and the layer to be entirely filled with water, or water containing air bubbles with void fraction of $\phi = 10^{-4}$.

The calculations shown in Fig. 2.22 are performed at atmospheric conditions. As the ambient pressure is elevated, and if all the air remains in the bubbles, the bubbles become smaller. This lowers the void fraction, increases their bulk modulus, and increases their density. These effects are considered in Section 4.3. Additionally, no bubble dynamics are considered, i.e., it is assumed that propagation is at frequencies

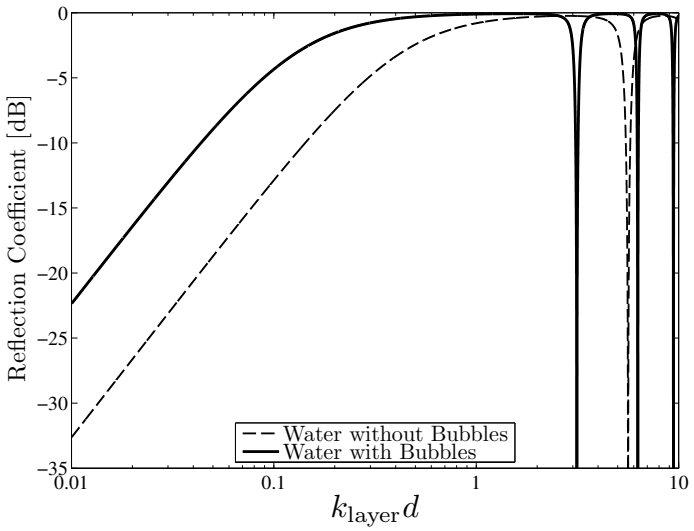


**Figure 2.22:** Plot of the reflection coefficient magnitude in decibels $20\log_{10}|\mathcal{R}|$ for a fluid layer between two limestone half-spaces with $\Omega = 0.2$ and $\phi = 10^{-4}$. Both curves are plotted relative to wavenumber $k_{\text{layer}}$ in the bubbly layer. The rock properties are the same as those used in Section 2.3.3 for Figs. 2.17–2.19.

far below bubble resonance. A consequence of this is that Wood's law may be used to determine the sound speed in the bubbly liquid.

As the frequency of the incident wave is increased, the wavelength in the layer becomes comparable to the thickness of the layer. When an integer number of half wavelengths fits exactly in the layer, and, since it has been assumed that the rock has the same properties on either side, the layer effectively becomes transparent to the incident wave.

### 2.3.5 Gassmann Equations at Elevated Pressure

Assuming that the elastic properties of the rock mineral are invariant with the increased pressure, including the effects of pressure on the volumes and densities of the bubbles allows Gassmann's euqation to be used to estimate the changes in rock properties due to the bubbles at some depth under water. That is, substituting Eq. (2.49) into Eq. (2.66) gives the properties of the rock saturated with water and

bubbles. Once the effective bulk modulus is known, Eq. (2.50) is employed to find the effective density, and the effective P-wave velocity $V_P^{r2}$ and impedance $Z_{r2}$ can be found as outlined in Section 2.3.3. The changes in saturated bulk modulus, P-wave velocity, and impedance are shown in Figs. 2.23–2.25 for varous depths and void fractions.

The change in hydrostatic pressure is again taken to be due to the load of the water, computed from Eq. (2.54). Thus, Figs. 2.23(a)–2.25(a), which correspond to atmpospheric conditions ($z = 0$), are identical to the curves in Figs. 2.17–2.19. The changes in bulk modulus (Fig. 2.23), P-wave velocity (Fig. 2.24), and P-wave impedance (Fig. 2.25) are all normalized by the no-bubble case. Since rock and liquid properties are constant over this pressure range, the normalization is the same for all curves on the plot. At greater depths, the bubbles are more compressed, causing them to become stiffer and provide less contrast.

While the gas bubbles are compressed and become significantly stiffer and denser, the absolute maximum deviations are not lowered substantially from the water-saturated case. However a much greater bubble fraction is needed to acheive that maximum amount of contrast. For example, Fig. 2.23(a) implies that at atmospheric conditions, the effective bulk modulus can be lowered by about 15% with a void fraction of $\phi \simeq 10^{-3}$. At a depth of 1 km [Fig. 2.23(b)], a 15% reduction of $K_r$ is still possible, but would require a much larger void fraction $\phi \simeq 0.1$. At 5 km [Fig. 2.23(c)], such a reduction in the bulk modulus would require a void fraction approaching unity.

The stiffening of the gas bubbles due to the elevated pressures is the dominant effect at most relevant void fractions $\phi \lesssim 10^{-2}$. However, at very high void fractions, the increased density of the bubbles begins to affect the overall effective density of the saturated rock. Figure 2.24 implies that a void fraction of greater than about 20% implies a P-wave velocity at a depth of 5 km than that is actually lower than those at depths of 0 or 1 km. However, the change in impedance $Z_r = \rho_r V_P^r$ monotonically decreases with depth; see Fig. 2.25.

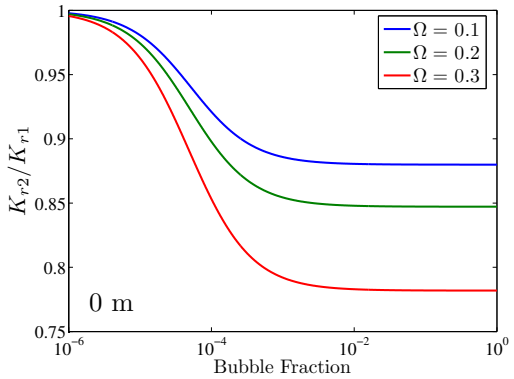


**(a)**

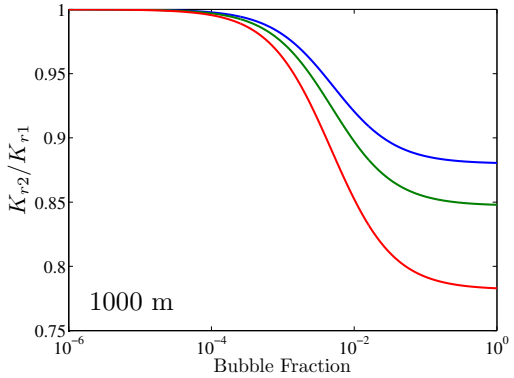


**(b)**

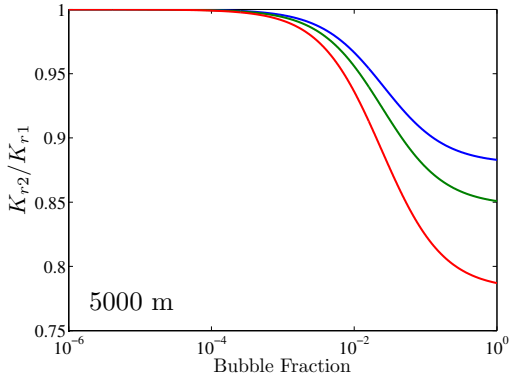


**(c)**

**Figure 2.23:** Changes in bulk modulus of water-saturated limestone $K_r$ as functions of gas fraction in the water $\phi$ (horizontal axes), and rock porosity $\Omega$ (by line color), at various depths. Calculated using Gassmann's relations and the pressure-dependent form of Wood's law.

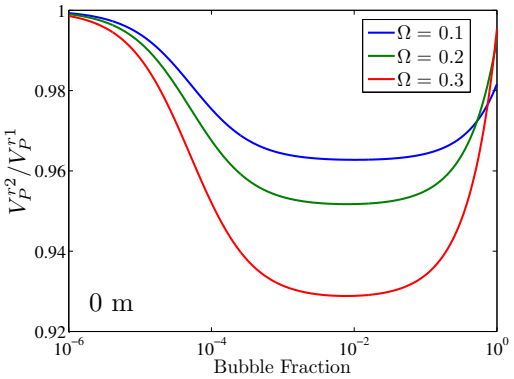


**(a)**

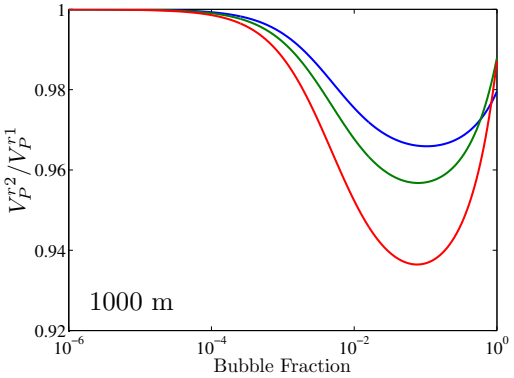


**(b)**

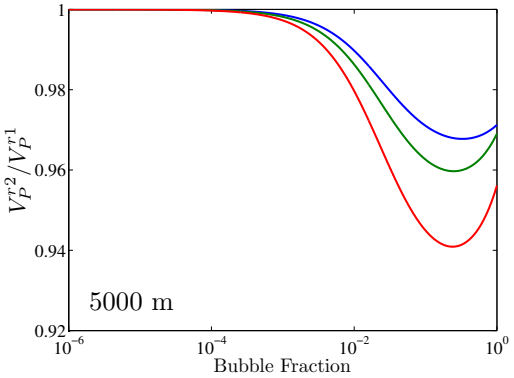


**(c)**

**Figure 2.24:** Changes in P-wave velocity of water-saturated limestone as functions of gas fraction in the water $\phi$ (horizontal axes), and rock porosity $\Omega$ (by line color), at various depths. Calculated using Gassmann's relations and the pressure-dependent form of Wood's law.

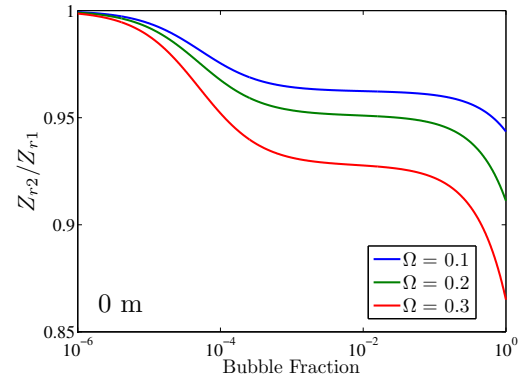


**(a)**

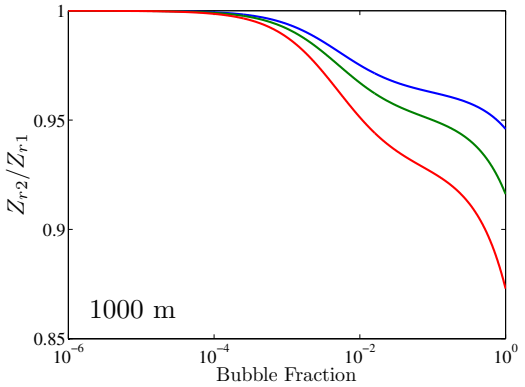


**(b)**

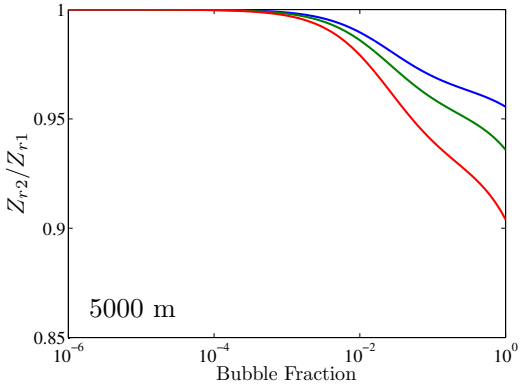


**(c)**

**Figure 2.25:** Changes in specific acoustic impedance $Z_r$ of water-saturated limestone as functions of gas fraction in the water $\phi$ (horizontal axes), and rock porosity $\Omega$ (by line color), at various depths. Calculated using Gassmann's relations and the pressure-dependent form of Wood's law.

A brief overview of the relative changes expected at reference void fractions and depths is compiled in Table 2.2. For reference, the changes in slowness $S = 1/V_P$ corresponding the listed relative P-wave velocity changes are listed in microseconds per foot, a unit common in practical sonic logging.[40]

| Depth [m] | | $\phi = 10^{-3}$ | $\phi = 10^{-2}$ | $\phi = 10^{-1}$ |
|---|---|---|---|---|
| 0 | Change in $K_r$ [%] | 14.6 | 15.2 | 15.3 |
| | Change in $V_p^r$ [%] | 4.6 | 4.8 | 4.5 |
| | Change in slowness [$\mu$s/ft] | 3.4 | 3.6 | 3.6 |
| 1,000 | Change in $K_r$ [%] | 2.6 | 10.3 | 14.6 |
| | Change in $V_p^r$ [%] | 1.0 | 3.2 | 4.3 |
| | Change in slowness [$\mu$s/ft] | 0.7 | 2.3 | 3.2 |
| 5,000 | Change in $K_r$ [%] | 1.0 | 4.0 | 13 |
| | Change in $V_p^r$ [%] | 1.0 | 1.4 | 3.7 |
| | Change in slowness [$\mu$s/ft] | 0.7 | 1.0 | 2.7 |

**Table 2.2:** Change in indicated quantities for gas bubbles in limestone with $\Omega = 0.2$.

## 2.4 Conclusion

The effects of gas bubbles on the bulk acoustic properties of a fluid can be dramatic, even when the bubbles comprise a small portion of the total volume considered. This effect is the motivation for their use as contrast agents. If the properties of a fluid can be so altered by the bubbles, then so too will the properties of an effective poroelastic solid, which contains that fluid. As was seen in Sections 2.2.4, 2.3.3, and 2.3.4, exploiting this effect provides an opportunity for significant contrast enhancement.

The effectiveness of gas bubbles is tied to their significant compressibility compared to the host medium. However, bubbles are not robust, and would not survive conditions of elevated pressure and/or temperature. The recent availability of more stable bubbles, synthesized by Professor Rubinstein's group at the Univeristy of North Carolina, has motivated interest in their potential effectiveness as contrast agents in such conditions. Estimation of their effect on the characteristic impedance of rock at

low frequencies[†] can be evaluated using the Wood's law in conjunction with the fluid substitution relations developed above. However, to obtain reasonable estimates, it is first necessary to determine the contrast agent bulk modulus $K_{\mathrm{CA}}$ at these conditions.

[†]More general models for contrast agents must account for dispersion due to the bubbles which now have an elastic shell. The effect of the shell on effective medium treatment is discussed in Section 4.2.2.

# Chapter 3

# Resonance Tube Calibration

The basic experimental appratus, consisting of a liquid-filled resonator and a distribution of bubbles whose bulk modulus is sought, is described in this chapter. The effects of tube elasticity are considered in Section 3.2, and the results of calibration and validation with air bubbles are presented in Section 3.3. Finally in Section 3.4, a model of a series of fluid layers is developed, and the model's predictions are compared with experimental results. The validated arrangement was used for the experiments described in Chapter 4.

## 3.1 Background

Acoustic resonators have been of significant interest to researchers since the time of Helmholtz and Rayleigh.[56,57] But even by middle of the 20$^{\text{th}}$ century, reconciling some nuances of the models with experimental results remained elusive.[58] The effort to understand the all of the relevant physics has been rightly motivated, as even relatively basic models of resonators have allowed for accurate measurements of sound speed and attenuation.[59–61]

For example, consider a one-dimensional resonator (one in which only plane waves are allowed) of length $L$ with both ends terminated by a pressure-release condition. Requiring the sound pressure to vanish at $z = 0$ and $z = L$ yields the natural frequencies[22]

$$f_n = n\frac{c}{2L}, \tag{3.1}$$

or, rearranging,

$$c = 2L\frac{f_n}{n}. \tag{3.2}$$

If the resonance frequencies of a plane wave resonator are measured, then the sound speed of the medium in the resonater can be deduced from Eq. (3.2). Of course, Eqs. (3.1) and (3.2) describe a highly idealized resonator with no losses and perfect pressure-release end conditions. While corrections must be made to raw data from real resonators, the general principles that lead to Eq. (3.2) hold for the experiments discussed below.

### 3.1.1 Experimental Apparatus

The arrangement has its roots in Wilson's doctoral research on propagation in bubbly fluids.[21] Subsequent modifications and data acquisition techniques were developed by Wilson and Dunton,[62] Greene,[63] and Dolder.[64,65] The apparatus described in this section, depicted in Fig. 3.1, is the result of this work.

For the experiments described, the resonator consists of a borosilicate glass tube, 45.7 cm in length, with an inner diameter of 51.0 mm and an outer diameter of 69.5 mm. The volume of the tube cavity is thus 933.2 mL, and was filled with degassed tap water. The resonance frequencies given by Eq. (3.1) are valid for a tube with pressure-release ($p = 0$) end conditions. The top of the water-filled tube is left open to the air, as the large impedance mismatch between the water and air ($Z_{\text{air}}/Z_{\text{water}} \simeq 2.8 \times 10^{-4}$) causes a near-zero acoustic pressure at the interface. Since the tube is oriented vertically and must contain the fluid, the lower end of the tube was sealed with a thin latex balloon and placed on a stack of Styrofoam blocks. The foam, usually usually about 5 cm thick, was sufficient to support the weight of the tube and fluid, while also simulating a pressure-release condition.[66]

The tube was excited with an LDS V101 vibrator, attached to a 5 cm aluminum stinger (i.e., a narrow rod with a 5 mm conical tip). The stinger was positioned about 2 cm below the surface of the water. To measure the pressure field inside the tube,

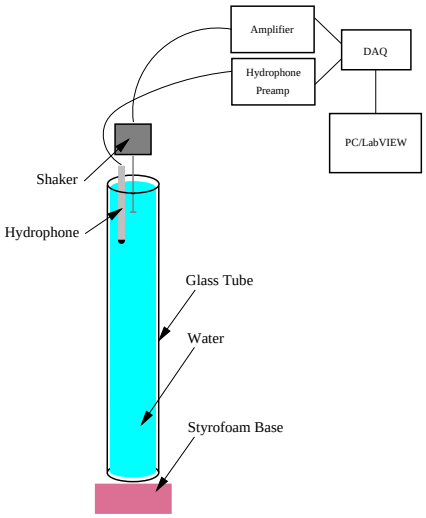


**Figure 3.1:** Experimental arrangement of the resonance tube. The shaker and hydrophone were positioned using a surrounding frame, so as to decouple mechanically the tube, shaker, and hydrophone.

a Brüel and Kjær model 4013 hydrophone was positioned near the top of the tube, also a few centimeters below the water level. Since the hydrophone and its cable have impedances similar to that of water, a water-filled steel sheath was used to surround the portion of the hydrophone cable that was submerged to decouple it from the field within the resonator.[63]

The vibrator was driven by a Crown CE9000 power amplifier, which was controlled by a National Instruments PCI 4461 data acquisition (DAQ) card, which handled the analog-to-digital conversion, and LabVIEW interface to automate and sychronize the equipment. Since the output signal of the hydrophone is very small, it was run to a Brüel and Kjær type 2692-0S4 conditioning amplifier, whose output was in turn connected to the DAQ/LabVIEW connection. Unless otherwise noted, the stinger was driven with a linearly-modulated frequency chirp from 0 to 10 kHz. The field in the resonator was sampled at 20 kHz, and 25 chirps were recorded. A uniform (i.e., rectangle) window was applied to the time-series data for each chirp, and these data were then averaged and a fast Fourier transform was taken of the average. A sample spectrum, for a water-filled resonator, is shown in Fig. 3.2. The peaks occur at the resonance frequencies of the tube, and the sharp dips indicate antiresonances. No

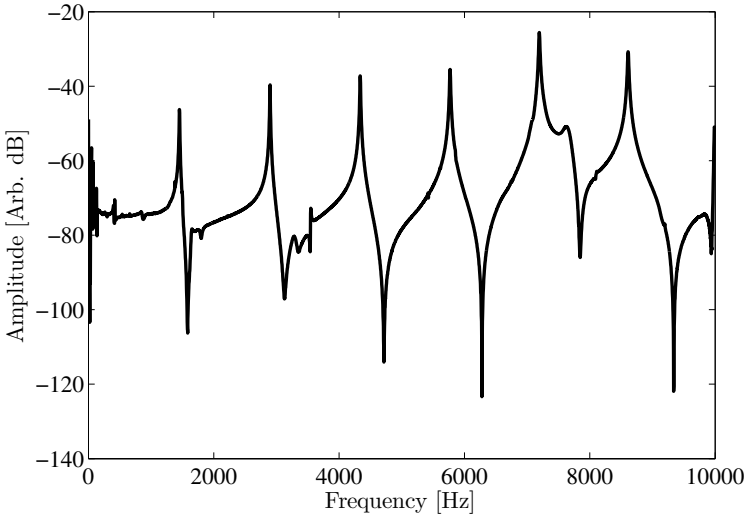


**Figure 3.2:** Typical frequency spectrum measured in a water-filled glass resonator tube with nearly pressure-release ends.

sound pressure level calibration was performed, because only the relative amplitude of the levels are significant.[†]

### 3.1.2 Wood's Law

Resonance tube measurements are capable of yielding very accurate determinations of the sound speed in a liquid, provided major effects such as tube wall elasticity are taken into account (see Section 3.2). The same measurements can be made for effective fluids, whose properties may be described by Wood's law;[14] see Section 2.2.1. If the sound speed in an effective fluid is measured via resonance tube, information about the compressibility, density, and relative volume of each constituent can be inferred using Eqs. (2.14) and (2.15). Wood's law may be extended to mixtures con-

[†]The normalization is made in LabVIEW relative to the maximum voltage sent to the power amplifier, usually 1 volt. However, the amplifier gain was not consistent between measurements, and due to the frequency-dependent impedance seen by the stinger, the piston velocity was not constant. The decibel scale in the recorded spectra gives little information about the absolute pressure level in the tube, but its relative levels are correct, and thus spectra will be normalized hereafter such that the maximum level is 0 dB.

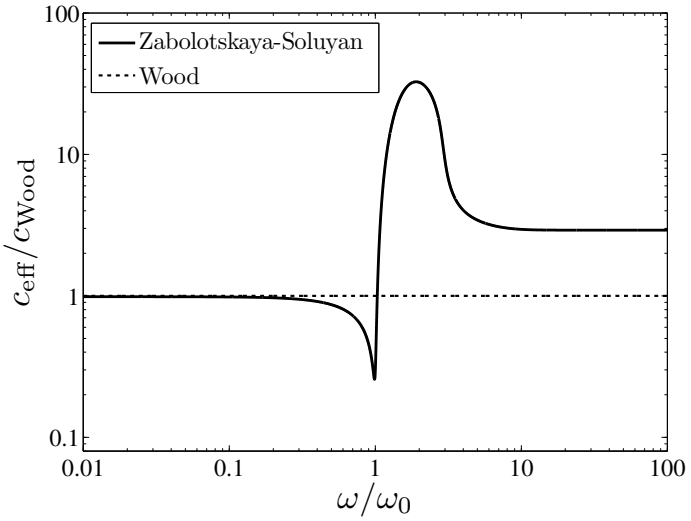


**Figure 3.3:** Comparison of effective medium model sound speed predictions for bubbly water. Bubble radii are uniformly $R_0 = 1$ mm, and the void fraction is taken to be $\phi = 5 \times 10^{-4}$. Frequency is normalized by the natural frequency of the bubbles.

taining elastic solids in liquids, and calculations have yielded measurements of the bulk modulii of solid materials.[63,67]

However, as discussed in Chapter 2, Wood's law does not account for any dispersive effects associated with bubble resonance. Since measurements here are concerned with bubbles, application of Wood's law must be restricted to regimes well below the bubble resonances. Figure 3.3 shows a comparison of two propagation models for a monodisperse distribution of bubbles. In the zero-frequency limit, the bubbles are compressed and decompressed slowly enough to act simply as increased compliance, lowering the bulk modulus of the medium. This is the main assumption made by Wood's law, and as can be seen in Fig. 3.3, it should hold provided $\omega \ll \omega_0$. Failure of assumptions underlying Wood's law are made plain near resonance, where the sound speed prediction can be orders of magnitude from the correct value.

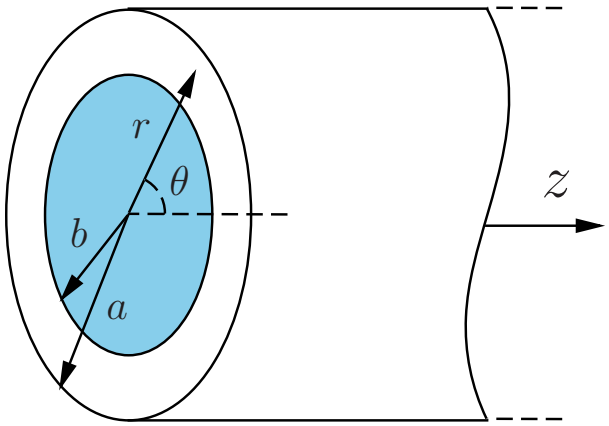


**Figure 3.4:** Coordinate system for an elastic waveguide. Propagation is in the $z$ direction.

## 3.2 Elastic Waveguide Effects

Equations (3.1) and (3.2) are idealized insofar as the following assumptions have been made: perfectly rigid walls, perfectly pressure-release end conditions, and propagation in the fundamental (plane-wave) mode. The assumption of pressure-release end conditions turns out to be sufficiently accurate for the experiments described in this thesis. However, due to the similar acoustic impedances of water and the glass walls of the resonator, the finite wall compliance (elasticity) must be taken into account.

In 1971, Del Grosso[68] published a model for axisymmetric propagation in an elastic tube of finite thickness; see Fig 3.4. Lafleur and Shields[69] gave numerical calculations and verified experimetally Del Grosso's model for several real fluid-tube combinations.[†] For a water-filled glass tube, the impedance ratio is $Z_{\text{water}}/Z_{\text{glass}} \simeq 0.125$. While the properties are relatively disparate, the impedances are sufficiently similar that elastic waves are generated in the walls of the tube. Enforcing the appropri-

[†]Section IA of Lafleur and Shield's paper, Ref. 69, gives a succinct summary of Del Grosso's analysis from Ref. 68, using slightly more intuitive notation. Existing code[21] was implemented following Lafleur and Shield's paper, and its equations are used here. However, the theoretical development is wholly Del Grosso's.

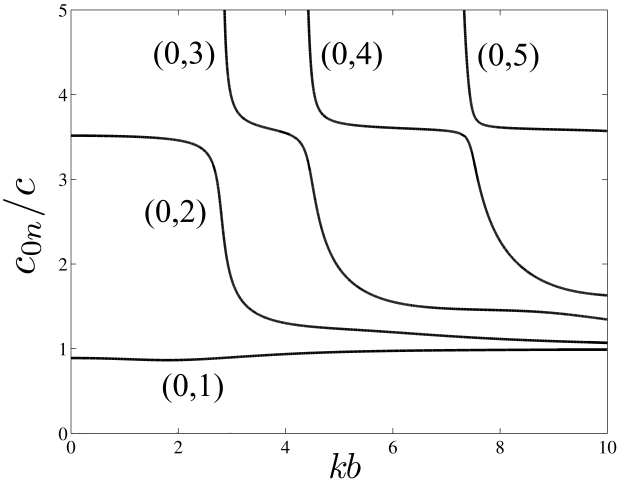


**Figure 3.5:** Axisymmetric mode dispersion curves for a water-filled glass tube. Curves are plotted against dimensionless frequency $kb$, where $k = \omega/c$, $c$ is the sound speed of the liquid in the tube, and $b$ is the inner radius of the tube.

ate boundary conditions leads to an exact, in the linear approximation, dispersion relation [Eq. (5) in Ref. 69], solutions to which are plotted in Figs. 3.5 and 3.6 for the conditions indicated. In both cases the dimensions and material properties of the tube were taken to be that of the tube used in the experiments described in this thesis: the inner radius $b$ is 25.5 mm, the outer radius $a$ is 34.8 mm, and the glass has a bulk modulus $K_{\text{glass}} = 35.2$ GPa, shear modulus $\mu_{\text{glass}} = 25.1$ GPa, and density $\rho_{\text{glass}} = 2230$ kg/m$^3$. Here $c_{0n}$ is the phase speed of the $n^{\text{th}}$ radial mode (the 0 is used to indicate axisymmetric propagation). Therefore the fundamental mode of interest, (0,1), corresponds to $c_{01}$.

The generation of elastic waves in the walls of the resonator tube will generally lower the phase speeds in the tube, such that the sound speed measured will be less than the free-field sound speed in the fluid $c$. The very lowest contour in Fig. 3.5, labeled (0,1), represents the phase speed in the first axisymmetric mode in the tube, that is, the mode in which particle motion is most nearly uniform across the width of the tube. Note that this fundamental mode travels at only about 90% of the free-field

sound speed at low frequencies ($kb < 2$), which is exactly the regime of interest for the measurements. Even if no other modes are present, the measured velocity $c_{01}$ in the fundamental mode must be corrected to obtain the free-field sound speed $c$.

Similarly, the $n^{\text{th}}$ radial, i.e., axisymmetric, mode in a rigid tube with radius $b$ has a cutoff frequency of[11]

$$f_c^{(n)} = \frac{c\alpha'_{0n}}{2\pi b}, \tag{3.3}$$

where $\alpha'_{0n}$ is the $n^{\text{th}}$ root of the first derivative of the $0^{\text{th}}$ order Bessel function of the first kind. That is,

$$J'_0(x)|_{x=\alpha'_{0n}} = 0, \quad n = 1, 2, 3, \ldots, \tag{3.4}$$

where the prime on $J_0$ indicates the derivative with respect to its argument. For the dimensions of the glass tube used, the first of these cutoff frequencies occurs at about 17 kHz. Were the tube rigid, excitation frequencies below this limit would preclude propagation in the first radial mode,[†] and purely planar motion of the fluid would be assured. In Fig. 3.5, this second axisymmetric mode is indicated by the second-lowest contour, labeled (0,2), which flattens out below $kb = \pi$. Again, the rigid tube assumption fails, since rather than cutting off when the width becomes smaller than a half-wavelength in water, this mode exists at all frequencies down to $kb = 0$. Since the low-frequency phase speed for this mode is over 3 times the phase speed for the fundamental, resonances that are due to this mode occur at frequencies well above the first several resonance frequencies of the (0,1) mode.[‡]

The elasticity of the tube wall does not always have such drastic effects on the velocity of the fundamental mode. As the sound speed (and thus the characteristic impedance) of the fluid contained in the tube is lowered, the glass wall begins to appear comparatively rigid. Figure 3.6 shows the dispersion of the (0,1) mode for

[†]Below its respective cutoff frequency, each mode is evanescent. If the tube length is on the order of a characteristic decay length of this evanescent mode, then a significant amount of energy can propagate in that mode, even at frequencies below its cutoff.

[‡]The first resonance of the tube due to this (0,2) mode occurs at $f_n = c_{02}/2L \simeq 3.5c/0.95$ m = 5.7 kHz. The first tube resonance for the fundamental mode occurs near 1.45 kHz.

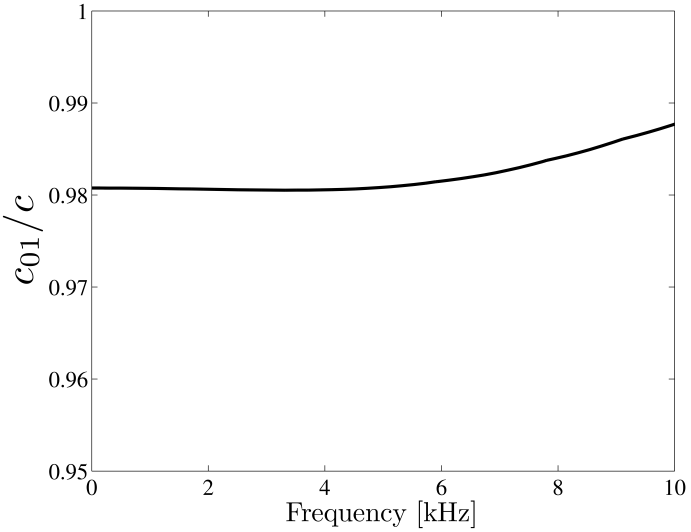


**Figure 3.6:** Phase speed of the fundamental axisymmetric mode for a glass tube containing water with void fraction $\phi = 5 \times 10^{-4}$, and thus $c = 431$ m/s. The parameters for the tube are the same as those used for Fig. 3.5

bubbly water containing 0.05% air bubbles. Bubble resonances are ignored, and therefore Wood's law is used for the fluid in the tube, which gives $c = 431$ m/s. This means that the phase speed in the fluid in the tube is non-dispersive.[†] The tube properties used are the same as those used in Fig. 3.5, and the phase speed is now plotted against frequency in the range of measurements, up to 10 kHz. Unlike the pure water case, the phase speed of the fundamental mode $c_{01}$ is within about two percent of the free-field sound speed $c$. In this case a rigid-tube assumption induces significantly less error in sound speed measurements. Elastic waveguide effects were nevertheless considered for all measurements, even though the correction may be small for some cases (as they are in Fig. 3.6).

[†]This implies that bubbles must be taken to be very small. For the case of water containing air bubbles in the tube whose properties were used for Figs. 3.5 and 3.6, requiring non-dispersive effective medium theory to hold below $f = 10$ kHz requires $R_0 < 300$ $\mu$m

## 3.3 Air Bubble Calibration

The main challange in measuring the compressibility of a mixture in a resonance tube is ensuring that the mixture of liquid and particles, namely, pure gas bubbles or contrast agents, is sufficiently homogeneous for Wood's law to be applicable. The compressibility of air bubbles has been measured with very good accuracy both by impedance tube measurements[21,70,71] and by resonance tube methods described above.[21,59,63,72,73] These experiments used a gas flux method, where gas bubbles were injected into the water column and allowed to rise freely to the surface. By controlling the gas flow rate, the volume fraction $\phi$ in the tube could be controlled.

However, using this technique for a resonance tube with contrast agents requires the fluid to be circulated, since a continuous supply of contrast agents cannot be achieved as it can be with gas bubbles. Compounding this difficulty is the need to measure a rapidly varying volume fraction of contrast agents. Since contrast agents are constantly entering and leaving the water column, determining the precise volume of contrast agents in the tube at the time of measurement becomes challenging. While optical methods have been used to this effect for gas bubbles,[16] the two-fold challenge motivated a different approach.

Effective medium theories such as Wood's law are valid if the mixture of the liquid and the contrast agents is acoustically homogeneous. The precise limits of what constitutes an acoustically homogeneous medium for a layered medium are investigated in Section 3.4, but results are not directly applicable since the samples will not be planar layers. However, known material properties have been recovered by using a discrete series of samples spaced along the tube, provided there are at least four samples per half wavelength.[63] Following this approach, a metal frame was constructed to support samples spaced approximately evenly along the water column. The frame was constructed such that no sample would be located exactly halfway along the tube, as this point is a pressure null for all even-numbered longitudinal modes in the tube. The frame was 2.8 cm in diameter and rested on the foam at the termination of the tube, and it did not contact the tube walls.

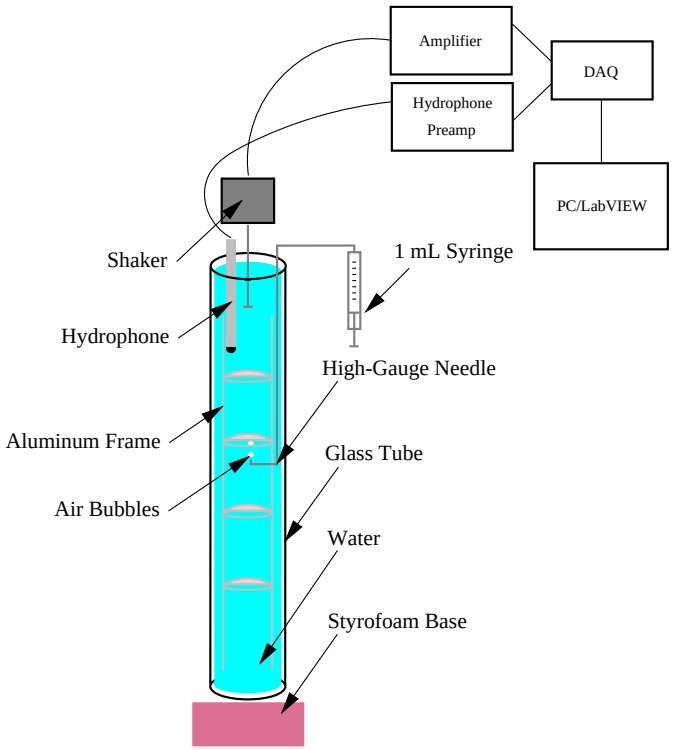


**Figure 3.7:** Diagram of the experimental apparatus used for the air bubble calibration measurements.

### 3.3.1 Experimental Apparatus

The arrangement for the air bubble measurements was largely the same as that described in Section 3.1.1, except for the inclusion of an apparatus to trap the air bubbles; see Fig. 3.7. Four traps were constructed, each consisting of a metal ring to which was affixed a dome-shaped segment of latex; see Fig. 3.8. Similar sample holders are used commonly in ultrasonic measurements since the impedance of latex is close to that of water and because it is readily available in thin sheets.[74,75] As was seen in Section 2.2.1, metal frames produce negligible changes in sound speed compared to those caused by the gas bubbles. This is especially true due to the very small fraction of the volume (less than 0.1%) occupied by the metal components. Resonance tube measurements were performed with the frame alone, and with the frame and traps together, and the discrepancy was less than 1%; see Appendix C.

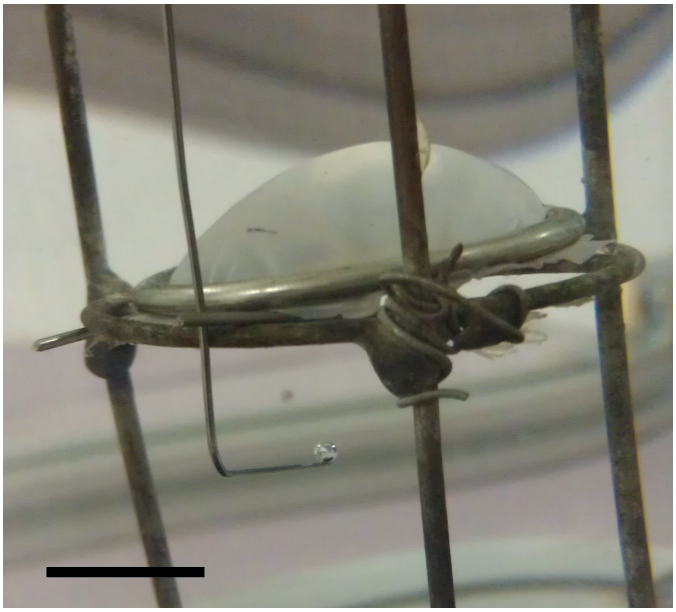

**Figure 3.8:** Air being injected into water column. A bubble can be seen clinging to the needle. The latex trap and metal frame are shown. Scale bar is 1 cm.

The traps were affixed to the four levels of the frame using copper wire, so as to leave the bottoms of the barriers mostly accessible to rising bubbles. The 46 cm glass tube was filled to the top with degassed water. The traps were inserted as the frame was lowered into the water-filled resonator, and then agitated below surface of the water to expel any clinging air bubbles. The whole assembly was left to rest for several hours to allow any remaining air bubbles to dissolve into the degassed water. Since the latex was slack, and therefore vibrational (drum head) modes were avoided, the traps did not appreciably affect the sound speed in the tube.

A 1 mL syringe with 10 $\mu$L gradations was then connected to a 61 cm flexible PVC syringe extension with an inner diameter of 16.5 mm (recall Fig. 3.7). Finally, a 10 cm high-gauge needle was connected to the extender and positioned under each barrier. The syringe plunger was carefully depressed to inject a known amount of air into the column. Many (10–20) bubbles were expelled from the needle tip and were quite small (see Fig. 3.8). As the bubbles floated upward and reached the latex trap, they would coalesce into one to three bubbles having diameters of less than 6 mm,

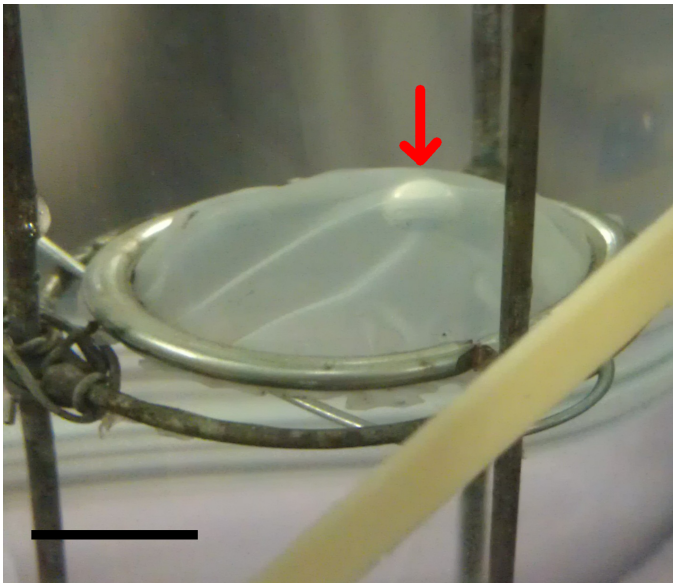

**Figure 3.9:** Air bubble (marked by red arrow) contained beneath one of the bubble traps. Scale bar is 1 cm.

depending on how much air was injected. The process was repeated at each trap (four in total). A bubble contained beneath a trap is shown in Fig. 3.9.

Once a known amount of air was contained beneath the traps, the tube was excited and the resulting spectrum was obtained. Once the measurement was taken, the injection syringe was again lowered into the resonator and more air was injected beneath each trap. The spectrum was again recorded. This procedure was repeated several times. As more air was injected underneath each trap, the resulting bubble would become larger. High attenuation near the resonance frequencies of these larger bubbles would begin to obscure the tube resonances, and thus measurements could be made with a maximum void fraction of about $\phi = 10^{-3}$ using this approach.

### 3.3.2 Sources of Uncertainty

Probably the largest source of uncertainty for the apparatus described in Section 3.3.1 was due to measurement of the air volume injected into the water column. While the gradations on the syringe allow very precise volumes to be measured, the air did not exit the needle in exact proportion to the compressions of the syringe

plunger. Hydrostatic loading on the opening of the needle due to the weight of the water column meant that an equivalent pressure needed to be created within the syringe before any air would be expelled. This meant the syringe plunger would be compressed about 0.1 mL before any bubbles escaped.

Similarly, while moving the needle away from the trap so that it could be raised to be positioned under the other traps, an air bubble would occasionally break off from the needle and escape to the open top of the water-filled resonator. These escaping bubbles were very small,[†] however, and while factored into the error bars, are certainly secondary to the first issue.

Also mentioned before was the fact that these relatively large air bubbles have natural frequencies near some of the tube resonance frequencies. As more air was injected, the resulting trapped bubbles became larger, and the resonance frequencies of those bubbles became lower. For the measurements with void fractions on the order of $10^{-3}$, attenuation due to the bubbles made the tube resonance peaks difficult or impossible to discern. This introduced some uncertainty in the sound speed measurement, up to $\pm 25$ m/s for higher void fractions. Figure 3.10(a) shows a typical spectrum measured with four bubbles in the tube. In this case the void fraction was $\phi = 4.8 \times 10^{-4}$, and the bubbles were about 6 mm in diameter. Figure 3.10(b) shows the prediction of the Zabolotskaya-Soluyan model (see Sec. 2.2.3.2) of attenuation due to air bubbles of the same size and comprising the same void fraction as was used during the measurement. The massive attenuation spike near bubble resonance, $f_0 \simeq 1080$ Hz, demonstrates why the spectrum in Fig. 3.10(a) is virtually flat in this region: enormous attenuation near the bubble resonance frequency means that propagation at these frequencies decays very quickly, standing waves cannot develop, and the resonances and antiresonances seen for the water spectra disappear. While the first two peaks visible in Fig. 3.10(a) are not very far below resonance, they do lie in the relatively flat region of Fig. 3.3. Therefore, these deviations of the peaks from the

[†]By a very rough estimation, a single bubble corresponds to about 20 $\mu$L, or a void fraction difference of $2 \times 10^{-5}$.

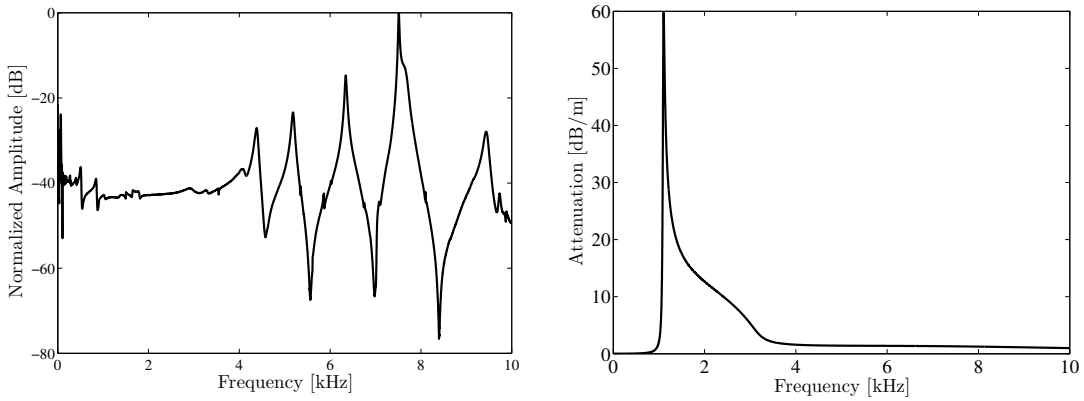


**Figure 3.10:** (a) Measured spectrum of water with air bubbles and (b) predicted attenuation calculated from the Zabolotskaya-Soluyan model. Here $\phi = 4.8 \times 10^{-4}$ and $R_0 = 3$ mm, approximating the measurement conditions.

non-dispersive Wood's law regime are on the order of a few percent. This discrepancy is included in the vertical error bars of Fig. 3.10(a). All effective sound speeds were calculated using the Lafleur and Shields correction described in Section 3.2.

Lastly, no effects of the tube walls on bubble behavior was considered. While the effects of elastic and rigid boundaries on bubble pulsations have been considered (see, e.g., Refs. 76, 77, 78, and 79), this effect was ignored since no appreciable shift in bubble resonance was observed. That is, the attenuation region predicted by Fig. 3.10(b) aligns closely with the areas of high attenuation seen in the measured spectrum in Fig. 3.10(a). While a significant shift in resonance frequency was not observed for the air bubbles considered, and is unlikely for bubbles as small as those discussed in Chapter 4, the effect of finite wall compliance may need to be considered should larger bubbles or narrower tubes be used.

### 3.3.3 Results

Once spectra had been recorded for several void fractions, the observed tube resonances $f_n$ and their corresponding phase speeds $c_n = 2Lf_n/n$ were found. Each

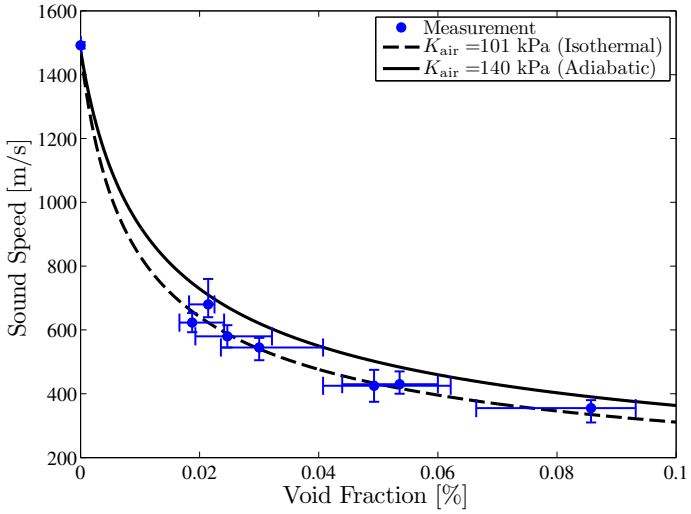


**Figure 3.11:** Measured sound speeds compared to Wood's law predictions.

phase speed was matched to a free-field sound speed such that it fell along the Lafleur and Shields prediction for the tube (e.g., Fig. 3.6). The mean of these free-field sound speeds was taken to be the effective sound speed of the bubbly water in the resonator. The results are plotted in Fig. 3.11, with the error bars representing the uncertainties discussed in Section 3.3.2. Also plotted with dashed lines are the Wood's law predictions for the sound speed as a function of void fraction with a given bulk modulus from Eq. (2.17).

The bulk modulus of air at atmospheric pressure is between 101 kPa and 140 kPa, depending on whether the compression is isothermal or adiabatic, respectively. While the data tend toward the isothermal limit ($\kappa = 1$), Fig. 2.4 suggests bubbles of their sizes, which were estimated to be 1 to 3 mm, ought to oscillate nearly adiabatically ($\kappa = 1.35$ to 1.37). For the void fractions above $\phi = 5 \times 10^{-4}$, the bubble radii were about 2 to 3 mm, and in this region, the tube resonance frequencies begin to encroach on the frequency range where dispersion becomes more important. Immediately below bubble resonance ($\omega/\omega_0 \simeq 0.5$), the phase speed in the bubbly water becomes appreciably smaller than the Wood's law result; see Fig. 3.3.

Since no dispersion due to the bubbles is accounted for by Wood's law, the results seem to indicate a lower than expected polytropic index. More likely, the calculated sound speeds in Fig. 3.11 are lower than the Wood's law result due to negative dispersion for frequencies near bubble resonance. Indeed, the lowering of phase speeds below resonance is predicted by dynamical models, which themselves are derived for effective media. Even though dispersion was ignored, the arrangement of four individual air bubbles recovers the known compliance of air to with sufficient accuracy. Further, substantially dispersive behavior is not expected in this frequency range for the microbubbles discussed in Chapter 4, which have resonance frequencies on the order of several megahertz.

## 3.4 Layered Medium Resonator Model

As discussed in Sections 3.1–3.3, recovery of properties from sound speed measurements relies on the fluid's responding to the sound field as a homogeneous effective medium. It was found during calibration that just four air bubbles distributed along the resonator tube were sufficient to approximate an effective medium for these purposes. While this validated apparatus will be used for the remaining bubble compressibility measurements, it is also useful to consider how the number of samples and their spacing affects the resonant behavior of the tube.

The model developed below allows the pressure field in the tube to be calculated by approximating the distributed samples as a series of fluid layers with differing acoustic properties. This field can then be compared to the result obtained by treating the layered structure as a fully homogeneous mixture.

### 3.4.1 Assumptions in Modeling a Resonance Tube with Discrete Layers

A major difference between the model presented here and the real resonance tube used in this research is that the model allows only plane-wave motion. As was seen in Section 3.2, nearly planar motion does dominate in the tube, especially

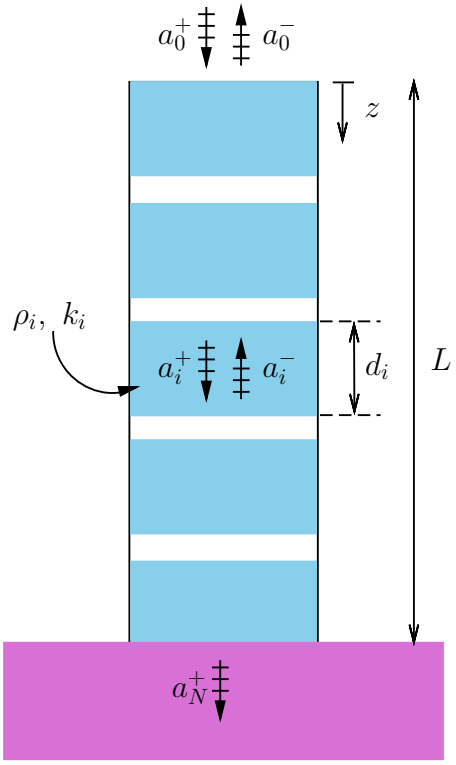


**Figure 3.12:** Geometry of the model described in Section 3.4. White space represents air and blue space represents water. The top ($0^{\text{th}}$) and bottom ($N^{\text{th}}$, pink to represent Styrofoam base used in practice) layers are treated as half-spaces with impedance $Z = Z_{\text{air}}$.

as bubbles are introduced and the sound speed in the effective medium is lowered. Whereas the gas bubbles which occupied some finite portion of the width of the tube, the one-dimensional model employs thin layers of air spanning the entire width of the tube; see Fig. 3.12. A general understanding is sought of how many levels of trapped gas bubbles (or encapsulated bubbles) are required, and where they should be placed in the tube, for the tube resonances to predict a sound speed in agreement with effective medium theory for a liquid containing the same amount of gas, but uniformly distributed.

Lastly, it is important to note that in the model, the tube is driven by a plane wave incident on the upper water surface. Likewise, radiation out from the lower water surface and into a Styrofoam half-space is assumed. Consequently, real air/water and water/Styrofoam interface conditions are imposed at the top and bottom of the tube, rather than the idealized pressure-release conditions discussed up to this point. Since the purpose of the model is to find the resonances and antiresonances of the system, the exact nature of the source is not important, and therefore no special effort was made to model the actual source condition used in the experiments, which was described in Section 3.3 and is located a few centimeters below the upper surface.

### 3.4.2 Method of Calculation[†]

The field in each layer $i$ is expressed as the superposition of two oppositely traveling plane waves:

$$p_i = a_i^+ e^{-jk_i z} + a_i^- e^{jk_i z}, \tag{3.5}$$

where $a_i^+$ is the acoustic pressure amplitude of the downward traveling wave in the $i^{\text{th}}$ layer, $a_i^-$ that of the upward-traveling wave in that layer, and the time-dependence

[†]This transfer matrix method follows the approach laid out for several analogous systems described in Refs. 80–83, and is in essence application of the impedance-translation theorem.[84,85] The code is essentially the same as was developed originally by Craig Dolder, only recoded by the author for convenience. This code was in turn validated by comparison with one written independently, based on a different approach, by Dr. Yurii Ilinskii. Models for elastic wave propagation in layered media are given in Refs. 86 and 87.

$e^{j\omega t}$ has been suppressed. Propagation has been taken to be positive downward ($z$ direction). The $i^{\text{th}}$ layer is defined by $z_i - d_i \leq z < z_i$, where $z_i$ is the vertical position of the interface between the $i^{\text{th}}$ and $(i+1)^{\text{th}}$ layer, and $d_i$ is the thickness of the $i^{\text{th}}$ layer. The field is determined by applying the appropriate boundary conditions.

1. The pressure must remain continuous across each interface:

$$p_i(z_i) = p_{i+1}(z_i). \tag{3.6}$$

2. The normal particle velocity must be continuous across each interface:

$$u_i(z_i) = u_{i+1}(z_i). \tag{3.7}$$

Taking the topmost surface of the water to be the first interface, the field in the $0^{\text{th}}$ layer above the top of the tube is $p_0 = a_0^+ e^{-jk_0 z} + a_0^- e^{jk_0 z}$. The coefficient $a_0^+$ of the wave incident on the upper water surface is known and serves as the source condition. The coefficients of the upward and downward traveling waves in each layer $i$ can be related to the coefficients in the subsequent layer $(i+1)$ by use of the continuity relations for pressure and particle velocity, Eqs. (3.6) and (3.7):

$$a_i^+ e^{-jk_i d_i} + a_i^- e^{jk_i d_i} = a_{i+1}^+ + a_{i+1}^-, \tag{3.8}$$

and

$$\frac{a_i^+ e^{-jk_i d_i}}{Z_i} - \frac{a_i^- e^{jk_i d_i}}{Z_i} = \frac{a_{i+1}^+}{Z_{i+1}} - \frac{a_{i+1}^-}{Z_{i+1}}, \tag{3.9}$$

where $Z_i$ is the characteristic impedance of the $i^{\text{th}}$ layer. The final layer, representing the Styrofoam termination of the resonance tube, is assumed to be a half-space, such that there is no upward-travelling wave incident on the $(N-1)^{\text{th}}$ boundary: $a_N^- = 0$. Then, the conditions at the final boundary can be expressed as

$$a_{N-1}^+ e^{-jk_{N-1} d_{N-1}} + a_{N-1}^- e^{jk_{N-1} d_{N-1}} = a_N^+, \tag{3.10}$$

and

$$\frac{a_{N-1}^{+}e^{-jk_{N-1}d_{N-1}}}{Z_{N-1}} - \frac{a_{N-1}^{-}e^{jk_{N-1}d_{N-1}}}{Z_{N-1}} = \frac{a_N^{+}}{Z_N}. \tag{3.11}$$

Now, Eqs. (3.8)–(3.11) can be written as matrix equations:

$$\begin{pmatrix} e^{-jk_id_i} & e^{jk_id_i} \\ \frac{e^{-jk_id_i}}{Z_i} & -\frac{e^{jk_id_i}}{Z_i} \end{pmatrix} \begin{pmatrix} a_i^{+} \\ a_i^{-} \end{pmatrix} = \begin{pmatrix} 1 & 1 \\ \frac{1}{Z_{i+1}} & -\frac{1}{Z_{i+1}} \end{pmatrix} \begin{pmatrix} a_{i+1}^{+} \\ a_{i+1}^{-} \end{pmatrix}, \tag{3.12}$$

$$\begin{pmatrix} e^{-jk_{N-1}d_{N-1}} & e^{jk_{N-1}d_{N-1}} \\ \frac{e^{-jk_{N-1}d_{N-1}}}{Z_{N-1}} & -\frac{e^{jk_{N-1}d_{N-1}}}{Z_{N-1}} \end{pmatrix} \begin{pmatrix} a_{N-1}^{+} \\ a_{N-1}^{-} \end{pmatrix} = \begin{pmatrix} 1 & 1 \\ \frac{1}{Z_N} & -\frac{1}{Z_N} \end{pmatrix} \begin{pmatrix} a_N^{+} \\ 0 \end{pmatrix}. \tag{3.13}$$

To solve for the incident and reflected amplitudes, Eqs. (3.12) and (3.13) are expressed as

$$T_i\mathbf{a}_i = T_{i+1}\mathbf{a}_{i+1}, \tag{3.14}$$

$$F_0\mathbf{a}_{N-1} = F_1\mathbf{a}_N, \tag{3.15}$$

where

$$\mathbf{a}_i \equiv \begin{pmatrix} a_i^{+} \\ a_i^{-} \end{pmatrix}. \tag{3.16}$$

The coefficient vector $\mathbf{a}_i$ gives the amplitude of the downward and upward traveling waves in the $i^{\text{th}}$ layer. Next, for convenience, the following transfer matrices are defined:

$$M_i \equiv T_{i+1}^{-1}T_i \tag{3.17}$$

$$F \equiv F_0^{-1}F_1. \tag{3.18}$$

The above matrices allow the coeffcient vector $\mathbf{a}_i$ to be found if the coefficients in the previous layer ($\mathbf{a}_{i-1}$) are known. Applying each matrix $M_i$ gives the coefficients as the wave propagates from the $i^{\text{th}}$ to the $(i+1)^{\text{th}}$ layer, and applying $F$ gives the coefficients as the wave enters the final half-space. Since the incident amplitude $a_0^{+}$ is known, application of the transfer matrix corresponding to each layer gives an expression for the pressure amplitude in the $N^{\text{th}}$ layer, $\mathbf{a}_N$:

$$\begin{pmatrix} a_0^{+} \\ a_0^{-} \end{pmatrix} = \left(\prod_{i=0}^{N-1} M_i\right) F \begin{pmatrix} a_N^{+} \\ 0 \end{pmatrix}. \tag{3.19}$$

The input reflection and transmission coefficients, $\mathcal{R}$ and $\mathcal{T}$, respectively, will describe reflection and transmission from the entire layered medium:

$$\mathcal{R} \equiv \frac{a_0^-}{a_0^+} \tag{3.20}$$

$$\mathcal{T} \equiv \frac{a_N^+}{a_0^+}. \tag{3.21}$$

Then, by Eq. (3.19),

$$\begin{pmatrix} 1 \\ \mathcal{R} \end{pmatrix} = \left( \prod_{i=0}^{N-1} M_i \right) F \begin{pmatrix} \mathcal{T} \\ 0 \end{pmatrix}. \tag{3.22}$$

Use of Eq. (3.19) yields an expression for $a_N^+$ in terms of the incident pressure coefficient $a_0^+$. Finally, from the definition of $\mathcal{T}$, the reflection coefficient $\mathcal{R}$ can be obtained using Eq. (3.22). Once $\mathcal{R}$ is determined, the pressure coefficients in each layer can be found by application of the transfer matrices, Eqs. (3.17) and (3.18), to the appropriate layer.

### 3.4.3 Results

The model above was applied for several cases to investigate behavior of the layered tube and the effects of the positions of the bubbles. First, each bubble was represented as a thin layer of pure air. Next, a layer with a thickness several bubble radii was designated about each bubble, and that layer was taken to have properties of an effective medium. Finally, the positioning of the layers is varied to estimate the importance of the distribution of layers within the tube.

#### 3.4.3.1 Air Layers

Since the air bubbles in the tube are to be modeled first as thin layers of air, analyses must be limited to very low void fractions ($\phi \lesssim 10^{-4}$). If the void fraction becomes large, so too does the thickness of the layers. Due to the large impedance difference between air and water, even a moderately thin layer of air can create a nearly pressure-release boundary. As an example, results are shown in Fig. 3.13 for

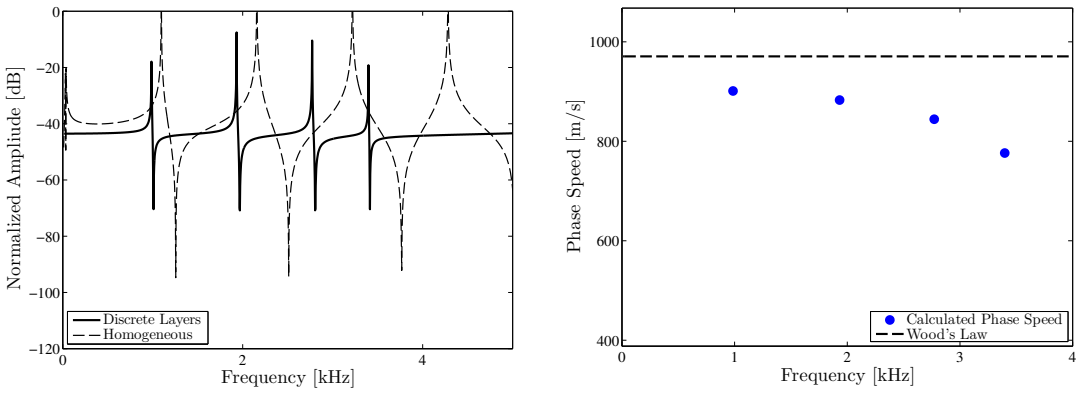


**(a)** **(b)**

**Figure 3.13:** (a) Predicted spectra for a resonator containing gas bubbles with $\phi = 10^{-4}$ when the mixture is fully homogeneous (dashed line) and when they are treated as four pure air layers with thickness given by Eq. (3.23), evenly-spaced along the length of the tube (solid line). (b) Phase speeds for the fully homogeneous case (dashed line), and for the discrete layer case (blue dots), from the resonance peaks of the dashed and solid spectra, respectively, in (a).

four equal layers of air, which together produce a void fraction of $\phi = 10^{-4}$. To distribute the air volume evenly among the layers, the thickness of each air layer $d$ is given by

$$d = \frac{\phi L}{N}, \tag{3.23}$$

where $N$ is the total number of layers and $L$ is the length of the tube. By default, the layers were positioned evenly along the length of the tube. That is, the center of the $n^{\text{th}}$ air layer was positioned at $z = nL/(N+1)$, where $N = 4$ for Fig. 3.13, $L$ was taken to be 45.7 cm, the length of the tube used for the gas bubble experiments, and the spectra were taken at $z/L = 0.05$, the approximate position of the hyrdophone during experiments.

For a void fraction of $\phi = 10^{-4}$, the model predicts the spectrum plotted with a solid line in Fig. 3.13(a). For reference, the spectrum that would be expected for a fully homogeneous effective medium with properties given by Wood's law is indicated by the dashed line in Fig. 3.13(a). The first four resonance peaks predicted by the

model are reasonably clear and close to evenly spaced. However, above the fourth tube resonance the peaks cease to be close to uniformly seperated, and there appears to be a stop band in which no tube resonances or antiresonances appear. Since the air and water layers form a periodic structure, certain resonances will occur between the layers, leading to stop band phenomena. There is a wealth of literature on the effects of periodic waveguides and the resulting Bloch waves for acoustic propagation.[88–90†] The result of taking these first four resonances and calculating the implied phase speed $c_n = 2Lf_n/n$ of the $n^{\text{th}}$ mode in the tube is indicated by blue dots in Fig. 3.13(b). The model predicts phase speeds that are about 10–12% lower than the sound speed predicted by Wood's law for the homogeneous case indicated by the dashed line in Fig. 3.13(b). While a 10% error is substantial, it is not significantly larger than the uncertainty in the measurements that allowed for recovery of the bulk modulus of gas bubbles in Section 3.3; it is encouraging that the beharior of just a few discrete layers is reasonably similar to that of a fully homogeneous mixture.

Calculations are now made for several void fractions with varying numbers of evenly-spaced layers, with the $n^{\text{th}}$ air layer centered at $z = nL/(N+1)$. Figure 3.14 shows the average deviation of the phase speeds from the fully homogeneous case, found for a given number of layers and at a particular void fraction. For each number of layers $N$, the first $N$ tube resonances were found from the spectrum, and each corresponding phase speed $c_n = 2Lf_n/n$ $(n = 1, 2, ..., N)$ was calculated. The mean of these $N$ phase speeds, $c_n^{\text{avg}}$ was then taken and its absolute difference from the Wood's law prediction $c_{\text{Wood}}$ was plotted. That is, the vertical axis of Fig. 3.14 represents the quantity

$$\text{Mean Error} = \frac{c_n^{\text{avg}} - c_{\text{Wood}}}{c_{\text{Wood}}} \times 100\%. \tag{3.24}$$

As expected, larger void fractions produce much larger errors, since the air layers must be thicker and the impedance change seen at the interface becomes larger. For

†"Bloch waves" were first described by Felix Bloch in 1928 in the context of particle wavefuntions in periodic potentials. His doctoral thesis *Über die Quantenmechanik der Elektronen in Kristallgittern* is considered a foundational work in condensed matter physics.[91]

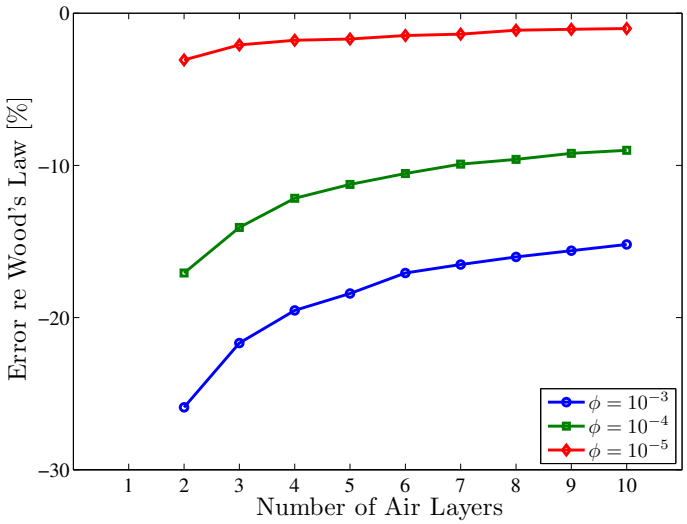


**Figure 3.14:** Plot of the error $(c_n^{\text{avg}} - c_{\text{Wood}})/c_{\text{Wood}}$ in percent as a function of the number of air layers used. For $N$ layers, the first $N$ tube resonances were used to calculate $N$ phase speeds. The mean of these phase speeds was used as $c_n^{\text{avg}}$. The layers were evenly spaced.

a void fraction of $10^{-4}$, the error is about 12% for four layers (green squares), which corresponds to the case shown in Fig. 3.13. It also seems reasonable that as more layers are used, the error is decreased. This is partly due to the layers' becoming thinner, as the same amount of air is distributed over more layers. But intuitively, it would seem that more layers are simply a better approximation of an effective medium.

#### 3.4.3.2 Effective Medium Layers

As an approximation of the conditions of the measurements performed as described in Section 3.3, the pure air layers are replaced by a demarcated multi-bubble layer in the immediate vicinity of each bubble trap. The properties of the layers are computed by assuming that the layer with the bubble acts as an effective medium, with the effective density of the layer given by Wood's law, and the effective wavenumber in the layer given by Eq. (2.46). Since the wavenumber is now complex, attenuation near the resonance frequency of the bubbles is expected. The void fraction

within each layer is

$$\phi_i = \frac{\phi L}{Nd}. \tag{3.25}$$

Since the layer is no longer purely air, the layer thickness $d$ now must be specified.[†]

To match conditions of the measurement, the bubble radii were specified to be 3 mm, and the void fraction with respect to the entire tube was set to $4.85 \times 10^{-4}$. The layers are taken to be 5 bubble radii (15 mm) thick, and the layer positions for the model were shifted slightly toward the center of the tube, namely, at $z/L = 0.244$, 0.422, 0.578, and 0.756. Figure 3.15 shows the computed spectrum (dashed line) of the model; for comparison, the spectrum recorded during the measurement is plotted with a solid line.

The model recovers some the main features of the actual measurement. Two of the tube resonance peaks are relatively clear below 2 kHz, and their positions are within a few tens of hertz of each other.[‡] The model predicts the stop-band region due to high attenuation near bubble resonance between 1–2 kHz. The measurement clearly shows recovery of tube resonances above bubble resonance beginning at about 4 kHz, when the attenuation becomes small again. However, the model predicts no tube resonances until well above 6 kHz. This difference is due to the modelling of the localized bubbles as effective medium layers. The broad frequency range in Fig. 3.15 between 1.5 and 6 kHz, in which the model predicts no tube resonances or antiresonances, is partly due to attenuation due to the bubbles, but likely also due

[†]While this choice is arbitrary, the layer thickness was restricted to the immediate vicinity (less than $10R_0$) of the layer center. It was found that varying this thickness within a factor of 2 affected the amplitudes of the predicted spectral peaks, but did not change appreciably the frequencies of the peaks.

[‡]The layered medium model does not account for the elastic waveguide effect discussed in Section 3.2. But since the sound speed has been lowered significantly by the air in the tube, the model and measurement should not differ substantially due to this particular effect.

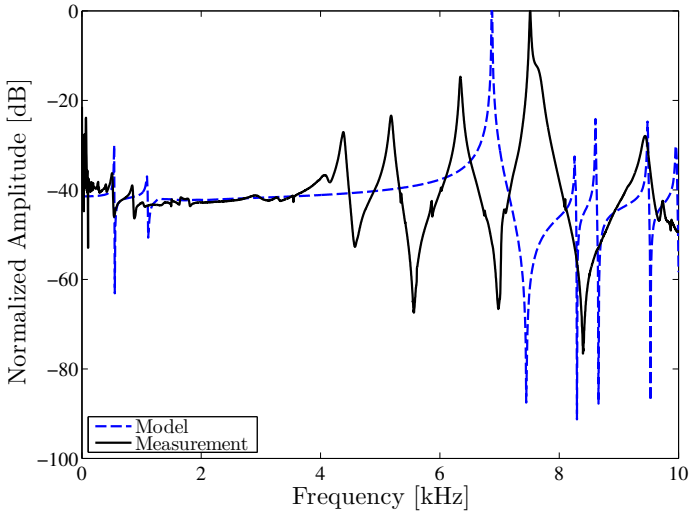


**Figure 3.15:** Layered-medium model prediction (dashed line) of the spectrum that would be measured with four bubbles with $R_0 = 3$ mm spaced approximately how they were for the measurement (solid line). The measured spectrum alone is plotted in Fig. 3.10(a). A dynamical effective medium model, taking bubble resonance into account, was used when calculating the dashed line.

to the stop band behavior of the periodic structure assumed. The latter effect is not one that exists, at least as it was modeled, in the actual resonator tube.[†]

#### 3.4.3.3 Bubble Positioning

Now calculated from the model is the effect of shifting the vertical positions of the layers from an evenly-spaced configuration. A single layer, with properties given by Wood's law (i.e., no dispersion or attenuation), was taken to be $d = 1$ cm thick. The void fraction in the tube was chosen to be $\phi = 10^{-4}$, and so the void fraction

[†]For a periodic medium consisting of a water column subdivided by thin layers of air, the ratio $K_{\text{water}}/K_{\text{air}}$ is so large, of order $10^4$, that the dispersion relation for the Bloch wavenumber reveals that the pass bands have all but disappeared, such that there is essentially no propagation at any frequency. So the question arises as to why the dashed line in Fig. 3.15 predicts propagation at frequencies above 6 kHz. One possible explanation is that far above bubble resonance, dynamical models predict the effective phase speed to equal the phase speed in the liquid without bubbles [recall Fig. 2.5(a)]. Therefore the layers become acoustically transparent well above bubble resonance, causing any stop band behavior to disappear as well.

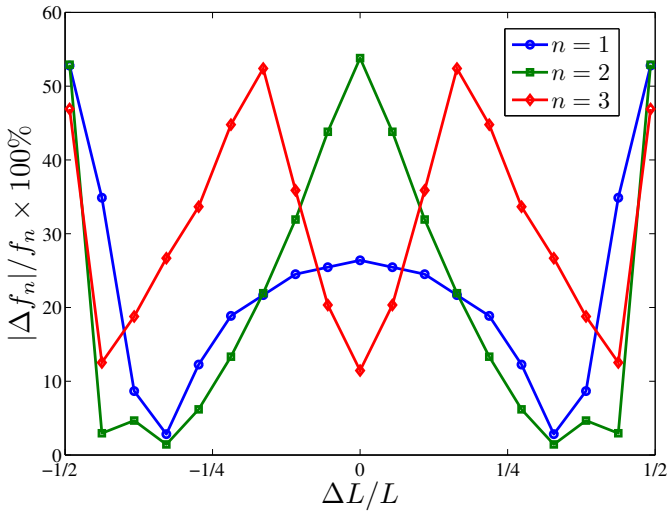


**Figure 3.16:** Effect of the position a single effective medium layer of thickness $d = 1$ cm on the first several resonance frequencies of the tube. The displacement $\Delta L$ here represents the distance of the layer's center from $L/2$, and $f_n$ is the frequency of the $n^{th}$ tube mode predicted by Wood's law (i.e., by assuming the entire tube contains one effective medium).

within the layer is $\phi_{\text{layer}} = \phi L/d = 4.57 \times 10^{-3}$. The position of the layer within the tube was varied along the length of the tube, and the first three tube resonances predicted by the model were recorded. These were then compared with the first three resonances, $f_1$, $f_2$, and $f_3$, that would be expected for a totally homogeneous water/air mixture with $\phi = 10^{-4}$. The relative magnitude of the difference $|\Delta f_n|/f_n$ is plotted in Fig. 3.16.

Figure 3.16 shows that placing the layer at the center of the tube causes the first three tube resonances to differ substantially from an effective medium result. The second resonance (green squares) differs by over 50% for a layer at that position. This is because the second tube mode has a null at $z = L/2$; the added compliance of the air will not be seen by this mode, and the resonance of this mode occurs very near the pure-water position. As the layer moves toward $\Delta L/L = \pm 0.3$, the first two mode resonances (blue circles and green squares, respectively) tend to within a few percent of those that would be expected if the fluid were a true effective medium. Finally, if

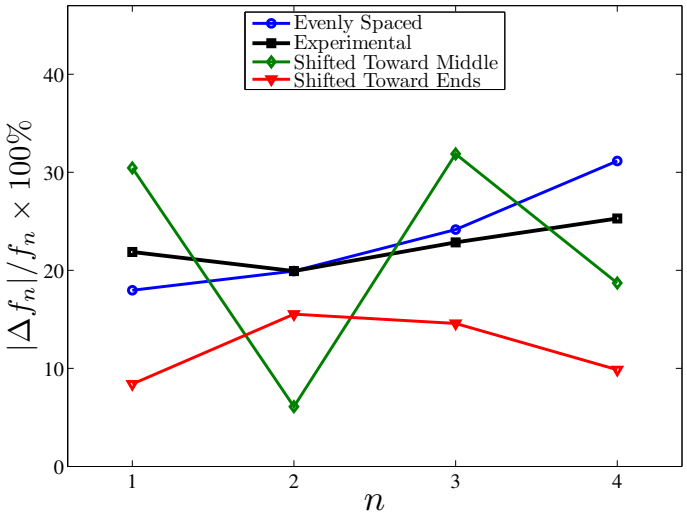


**Figure 3.17:** Effect of the position four effective medium layers of thickness $d = 1$ cm on the first four resonance frequencies of the tube. The four layers were positioned in the indicated arrangements, and the deviation of the first four resonance peaks from those expected for a fully homogeneous medium were calculated.

the layer is positioned at either end of the tube, where $\Delta L/L \simeq \pm 1/2$, the effect of the compliance of the air is negated, since the layer is very near a pressure null for all modes. Hence the spectrum for this case resembles that of water with no air.

As an estimate of how well chosen the positions of the samples in the experimental apparatus were, the layer positioning for four layers is varied, and the discrepancies of the first four resonance frequencies predicted by the model are again compared with the first four resonance frequencies ($f_1$, $f_2$, $f_3$, and $f_4$) that would be expected for a tube with a totally homogeneous effective fluid. The results are plotted in Fig. 3.17.

First, the layers were distributed evenly, such that their centers were located at $\frac{1}{5}L$, $\frac{2}{5}L$, $\frac{3}{5}L$, and $\frac{4}{5}L$ (blue circles in Fig. 3.17). Then, the layers were shifted slightly to correspond to the positions of the gas bubbles during measurements (black squares). The deviation of the first resonance frequency from $f_1$ for the homogeneous case is smaller for the evenly spaced layers than for the experimental positions. The difference for both spacings from $f_2$ is about 20%, and the differences from $f_3$ and $f_4$ are slightly less for the experimental spacing than for the uniform spacing. The

model would imply that the positions used for the experiment are a marginally better approximation of an effective medium.

Next the layers were shifted by $\frac{1}{6}L$ from their evenly spaced positions. That is, the each layer was shifted toward the middle of the tube (green diamonds), such that they were located at $z/L = 0.367$, 0.433, 0.567, and 0.633.[†] Then each layer was shifted toward the top and bottom of the tube (red triangles), such that they were positioned at $z/L = 0.033$, 0.233, 0.767, and 0.967. When shifted toward the center of the tube, $z = \frac{1}{2}L$, the expected resonances vary more erratically. However, as the layers are shifted away from the center, toward the top and bottom of the tube, the deviation from the fully homogeneous case is smallest. This effect was also seen for a single layer in Fig. 3.16, where placing the layer nearer the ends of the tube caused smaller deviations from the effective medium resonances.

The model confirms what might be intuited: that many, thinner layers are a better approximation of an effective medium than are a few, thicker layers. It also suggests that the resonances of the tube will be closest to the corresponding effective medium tube resonances when the layers are located away from the center of the tube. Of course placing the layers at either termination of the tube, where a pressure null always occurs, negates any change in sound speed, and the spectrum will be that of a water-filled resonator. While the model is capable of capturing some of the behavior seen during measurements, differences from experimental conditions were introduced via the assumption of discrete layers.

Finite element modeling has shown that perturbations in bubble size and position can have easily observable effects on resonator measurements when there is a small number of bubbles per wavelength. For example, Lee et al.[92] showed that $\pm 8\%$ sound speed variations were produced by random perturbation of bubble size and position,

[†]The shifting of the second and third layers by $L/6$ toward the center causes their sequence to change. That is, the original third layer becomes the second from the top of the tube, and the original second layer becomes the third layer from the top of the tube. Since the layers are identical they are listed in order of position for simplicity.

similar to what might be found in a typical experiment ($\pm 10\%$ in the bubble radius, and $\pm 1.3\%$ of tube length in the individual bubble position along the waveguide axis).

## 3.5 Conclusion

When the elastic behavior of the resonator tube is included, very accurate measurements of the sound speed in the fluid it contains can be made. Further, the ability of the glass resonator apparatus described in this chapter to recover known compliances makes it a useful tool to measure and corroborate unknown and known material properties. And its relative compactness allows the experiment to be placed in a pressure apparatus and pressure-dependent effects to be determined. An exact quantification of the number and positions of the layers within the tube that are required such that the discretization of samples in the real resonator approximates an effective medium was not obtained. However, consistent results and calibration indicate the current experimental arrangement satisfies the current needs.

# Chapter 4

# Contrast Agent Characterization

In this chapter, basic models developed in Chapter 2 are extended to include the effects of bubble shells and the impact of elevated pressures on the bubble properties. Measurements using the basic experimental apparatus described in Chapter 3 at atmospheric conditions (Section 4.2), elevated pressure (Section 4.3), and elevated temperatures (Section 4.4) are performed on encapsualted microbubbles. Results of these measurements are then used to predict the effects of these contrast agents in saturated rock.

## 4.1 Background

Gas bubbles are of significant interest due to their ability to provide acoustic contrast to the surrounding medium. However, the interface at the surface of the bubble allows for diffusion of air out from the bubble and into the surrounding liquid. This means that, even if unperturbed, the gas bubble shrink and eventually disappear completely.[†] For milllimeter-sized air bubbles in water, this process takes a few hours (depending on saturation conditions), and this lifetime is reduced to a few seconds or less for bubbles with radii of tens of microns;[93] see Fig. 4.1.

The presence of an encapsulating shell is primarily motivated by this problem of diffusion. As the pressure increases, gas bubbles are compressed and diffuse ever more quickly. However, if the shell can mitigate (or ideally stop entirely) the transport of

[†]This is the case if the water is undersaturated. If the air concentration exceeds the saturation concentration, then gas bubbles will nucleate spontaneously and grow until they reach some equilibrium state.

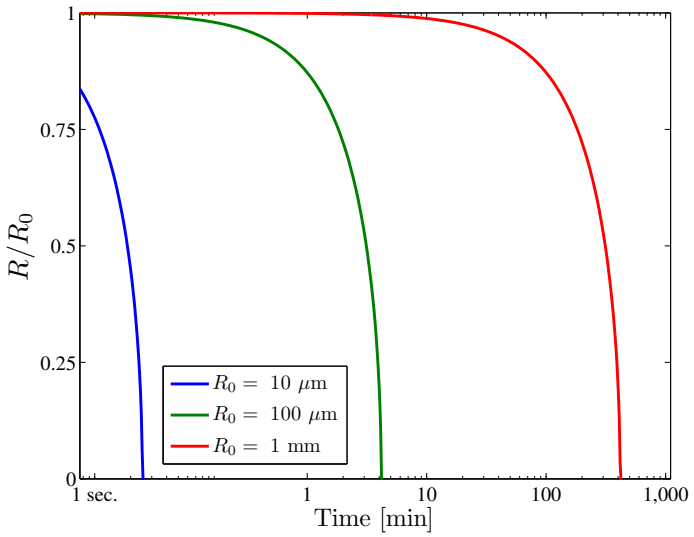


**Figure 4.1:** Dependence of bubble radius on time, given by Epstein and Plesset's approximate solution, Eq. (16) in Ref. 93. The result is for a single bubble in a large expanse, such that the concentration is not altered by the diffusing gas. The air concentration was taken to be half of the saturation concentration of 2 kg/m$^3$, and the diffusion coefficient was taken for air in water at 22°C to be $2 \times 10^{-9}$ m$^2$/s.

the contained gas into the surrounding liquid, then ability of the bubbles to provide contrast persists. While the shell adds significantly to the robustness of the bubble, this improvement comes at the cost of compliance; a shell with any foreseeable material properties will necessarily stiffen the bubble, and therefore cause a smaller reduction of the effective impedance of the bubbly liquid.

The effect of gas bubbles on the sound speed in an effective fluid, as was seen in Chapters 2 and 3, is extreme. While a shelled bubble may affect propagation less drastically, even effects that are scaled down from those seen previously should produce measureable effects. And given the increased survivability a shell provides, such bubbles are promising candidates for use as acoustic contrast agents.

### 4.1.1 Encapsulated Bubble Structure

The specifics of the structures and compositions of the contrast agents are not presented in detail here. Broadly speaking however, these bubbles fall into two general categories:

1. Pre-expanded bubbles: These contrast agents have a polymeric or surfactant outer shell around a gas core. The bubbles tested in Sections 4.2.3 and 4.3.2 had stiffer polymer outer shells, which reduced the amount of compression seen when subjected to an increased pressure. However, these stiffer shells are prone to sudden buckling and collapse under these loads. The softer-shelled surfactant bubbles compress more quickly, and any loss of contrast is caused by the much slowed diffusion of the gas from the core, unlike the sudden collapse of the harder shelled bubbles.

2. Thermally-controlled bubbles: These bubbles have a polymeric shell surrounding a gas or fluid-gas mixture. At a certain temperature, the contained fluid expands rapidly. Since this process occurs against the constraining ambient pressure, the expansion is such that the load does not crush the gas core. By controlling the properties of the mixture within the bubble, the expansion temperature can be controlled. These contrast agents were used for the measurements described in Section 4.4.

While the contrast agents shared some general structural similarities, the varieties tested were prototypes. Thus the results are taken to characterize the general behavior of these shelled bubbles as contrast agents, rather than the exact material properties of each type of contrast agent tested.

## 4.2 Ambient Conditions

The performance of encapsulated bubbles as acoustic contrast agents in real conditions motivates these measurements. It is first necessary to determine the properties

of these contrast agents at atmospheric conditions, such that this baseline may be extended by compression models to be compared with current measurements and eventually *in situ* behavior.

### 4.2.1 Estimate of Bulk Modulus

Beginning with Church's model[94] for elastic-shelled bubbles, Hoff et al.[95] present an expression for the bulk modulus of a thin-shelled bubble, valid for small perturbations of the bubble wall, i.e., $(|v'|/v_0)^{\frac{1}{3}} \ll 1$:

$$K_{\mathrm{CA}} = K_{\mathrm{gas}} + 4\mu\frac{h}{R_0}. \tag{4.1}$$

Equation (4.1) indicates that the shell increases the overall stiffness of the bubble, and that this increase in stiffness is greater for shell materials that have a higher shear modulus $\mu$, and those shells that are thicker compared to the radius of the bubble (larger $h/R_0$).

### 4.2.2 Encapsulated Bubble Dispersion

Church presents an effective medium model to account for the elastic shell.[94] The predicted sound speed in the effective medium is

$$\tilde{c}_{\mathrm{eff}} = c_{\mathrm{liq}}\left[1 + \left(1 + \frac{h}{R_0}\right)\left(\alpha_C\frac{\rho_{\mathrm{liq}}}{\rho_{\mathrm{sh}}}\right)\frac{K_{\mathrm{liq}}}{K_{\mathrm{CA}}}\frac{\phi}{1 - \omega^2/\omega_0^2 + j\delta_{\mathrm{sh}}\omega/\omega_0}\right]^{-\frac{1}{2}}, \tag{4.2}$$

where the viscous damping $\delta_{\mathrm{sh}}$ includes the effects of the elastic shell and is calculated from[†]

$$\delta_{\mathrm{sh}} = \left(\frac{4}{\rho_{\mathrm{sh}}\alpha_C\omega_0 R_0^2}\right)\frac{\eta_{\mathrm{sh}} - (1 - h/R_0)^3(\eta_{\mathrm{liq}} - \eta_{\mathrm{sh}})}{(1 - h/R_0)^2}, \tag{4.3}$$

and

$$\alpha_C = 1 + \left(1 - \frac{\rho_{\mathrm{liq}}}{\rho_{\mathrm{sh}}}\right)\left(1 - \frac{h}{R_0}\right) \tag{4.4}$$

[†]Church also uses a dimensional damping constant, which he denotes $\delta_d$. Thus the damping constant in Eq. (4.2) has been redefined with $\delta_{\mathrm{sh}} = \delta_d/\omega_0$.

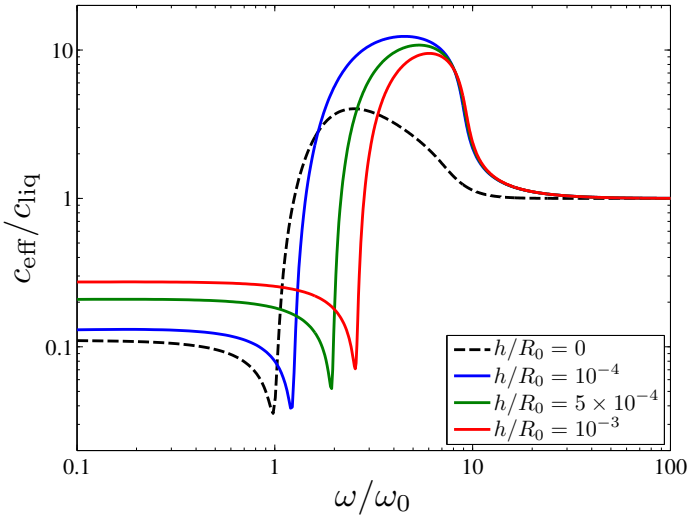


**Figure 4.2:** Phase speed predicted by Church's model, calculated from Eq. (4.2). The bubble radius is taken to be $R_0 = 200$ $\mu$m and the volume fraction is $\phi = 5 \times 10^{-3}$. Values for shell properties and the interfacial surface tensions are taken from Ref. 94, which used values for Albunex® ultrasonic contrast agents. The frequency is normalized to the Minneart frequency of a bubble with no shell (i.e., a free gas bubble).

is a density coupling term. Note that if there is no shell, then $h/R_0 \to 0$, $\alpha_C \to 1$, and Eq. (4.2) becomes Eq. (2.31) exactly. A monodisperse bubble population is assumed, such that all bubbles have the same inner radius and shell properties. The phase speed given by Eq. (4.2) is plotted in Fig. 4.2 for various shell thicknesses.

While the addition of the shell introduces a myriad of parameters that affect the effective sound speed, a few general qualifications can be made for typical shells:

1. The shell makes the bubble stiffer overall, thus increasing the resonance frequency; see Fig. 4.2.

2. Thicker shells (larger $h/R_0$) cause slightly higher resonance frequencies and smaller deviations from $c_{\mathrm{liq}}$ within the sub-resonance frequency range; see Fig. 4.2.

3. Shells with higher shear moduli $\mu$ cause slightly higher resonance frequencies and smaller deviations from $c_{\mathrm{liq}}$.

Since a shell increases the natural frequency of a gas bubble, if the frequencies of interest are below the natural frequency for a gas bubble of the same size, then they are guaranteed to be below the natural frequency of the shelled bubble. The largest encapsulated bubbles considered in this chapter have radii of 100 $\mu$m, and the Minneart frequencies of gas bubbles of that size are about 30 kHz. Even for the largest bubbles used, resonance phenomena of the bubbles should not be encountered in the measurement regime (0–10 kHz), and so the effective properties of a liquid containing these contrast agents are given by Wood's law.

### 4.2.3 Ambient Measurements

First, the bulk modulus of pre-expanded (that is, having gas cores that were at approximately atmospheric pressure) contrast agents was measured via resonance tube. These microbubbles were not designed to withstand elevated pressures, but measurement of their properties at atmospheric conditions determines the degree of stiffening due to the addition of the shell, when compared with the gas bubbles measured previously.

#### 4.2.3.1 Microbubble Preparation

An attempt was made first to perform the resonance tube experiment in the same manner as the air bubble calibration made in Section 3.3. However, several difficulties arose due to the nature of the encapsulated bubbles as first prepared. The contrast agents were originally shipped in a solution, and their bouyancy caused them to amass at the top of the container by the time of arrival. Because of the enormous effect of air bubbles on sound speed, great care had to be taken to avoid entraining any air in the syringe, syringe extender, or needle used to inject the microbubbles beneath the latex traps.

While it was managed to collect a small number of contrast agents without entraining any significant amount of air, two further complications arose. First, the total volume of the microbubbles injected into the water column was quite small with

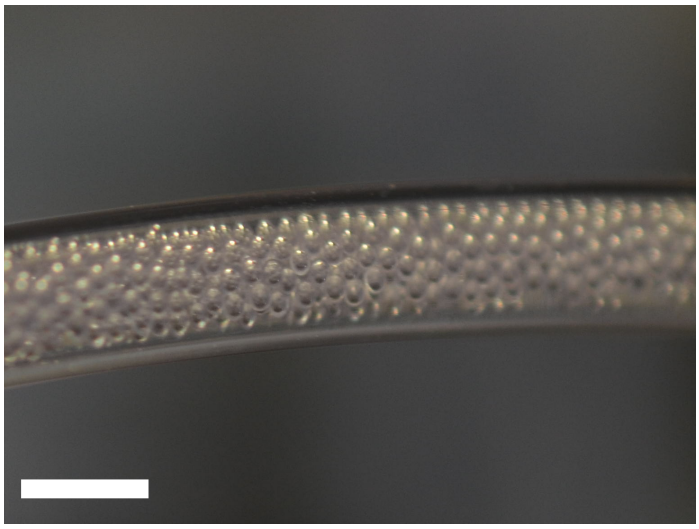

**Figure 4.3:** Photograph of large ($R_0 \sim 100$ $\mu$m) microbubbles in the syringe extender tube. Estimating the volume fraction of the contrast agents was difficult, since the microbubbles did not pack uniformly in the tube. Scale bar is 15 mm.

respect to the volume of the tube, on the order of $10^{-6}$. With such small volume fractions, and given the experimental uncertainty, a possible range of bulk moduli of $K_{\mathrm{CA}} \in (10^5, 10^{10})$ Pa was allowed.

Determining the precise volume fraction $\phi$ was also problematic. While the number of contrast agents in the shipping container was known fairly well from synthesis, not all of these microbubbles could be drawn into the syringe without also drawing in air bubbles. This meant the contrast agents needed to be counted in some manner. An estimate was achieved by measuring the length of syringe extender tube occupied by the microbubbles, and since the inner diameter of the extender was known, the volume of the tube where bubbles were present could be calculated. However, the buoyancy of the contrast agents caused them to collect more at the top of the tube than at the bottom. Further, they did not pack uniformly; see Fig. 4.3. While an assumption of random packing could be made, the uncertainty introduced proved problematic due to the relatively small volume of contrast agents.

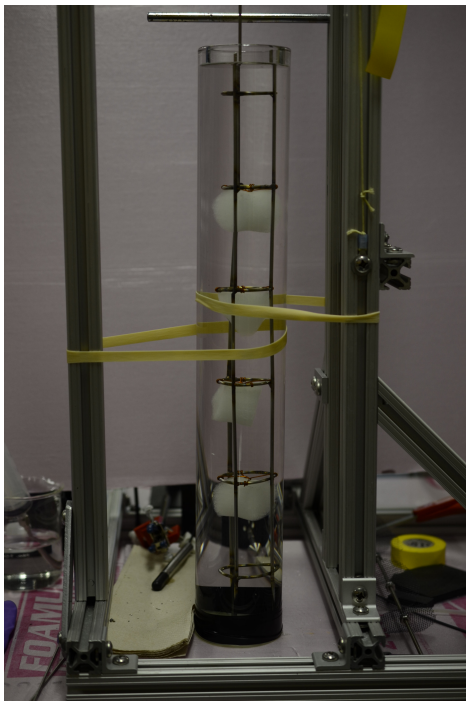

**Figure 4.4:** The divided polyacrylamide samples inside the resonator. The shaker and hydrophone are not in measurement positions.

To remedy these issues of air bubble entrapment, obtaining sufficient volume fractions, and accurately measuring these volume fractions, the microbubbles were placed in an acoustically transparent polyacrylamide gel by the synthesis group at University of North Carolina (UNC). This approach made several very substantial improvements, noteably that the contrast agent samples could now be reused, handled more easily, and the contrast agents could now comprise a significant portion of the total volume. Further, since polycrylamide has a very similar specific acoustic impedance to that of water,[96] the gels had virtually no effect on propagation, and all sound speed changes could be attributed to that of the microbubbles within the gel.

#### 4.2.3.2 Experimental Apparatus

Once the microbubbles had been incorporated into the polyacrylamide gel, the sample was divided into four pieces which were placed in the water column using the

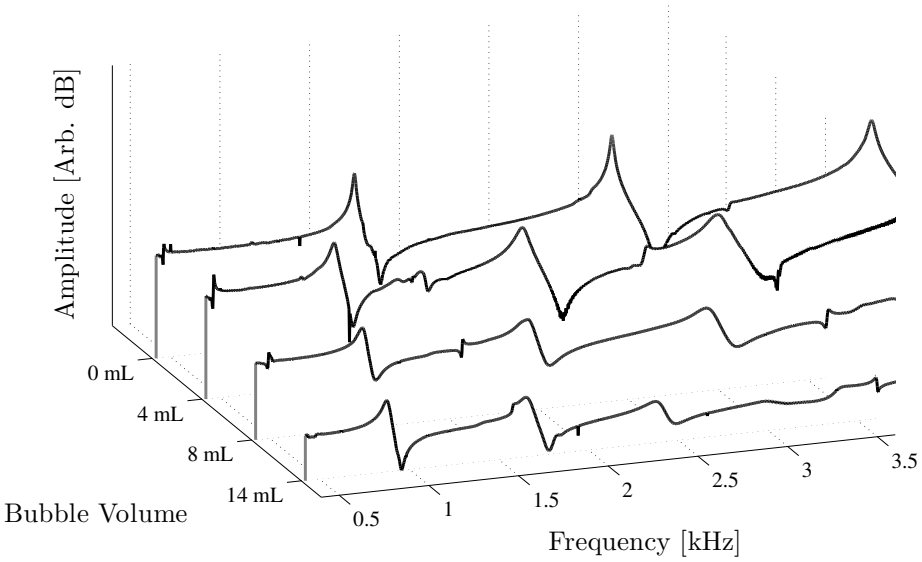


**Figure 4.5:** Raw spectra measured in the resonance tube with various quantities of microbubbles. The tube volume is about 933 mL, and so these correspond to microbubble volume fractions of $\phi = 0, 0.0043, 0.0086, \text{and } 0.0150$. The first three peaks of each spectrum are visible, and occur at lower frequencies as the volume fraction increases.

frame made for the air calibration measurements.[†] The procedure was then identical to that described in Sections 3.1–3.3: the resonator was excited and a spectrum was taken of its measured response. The resonance frequencies were then fit with the elastic waveguide model, and the best-fit $c_{\text{eff}}$ was taken to be the free-field sound speed of the effective medium. The raw data, which show the tube resonance peaks shifting to lower and lower frequencies as the number of microbubbles increases, are plotted in Fig. 4.5.

[†]The latex traps were removed, as the gel samples were sufficiently large to be held in place by the copper supports. The blank polyacrilamide (i.e., those containing no microbubbles) gels and some of the samples with smaller numbers of contrast agents were placed on top of the supports, but those with more bubbles were placed beneath, as they were buoyant.

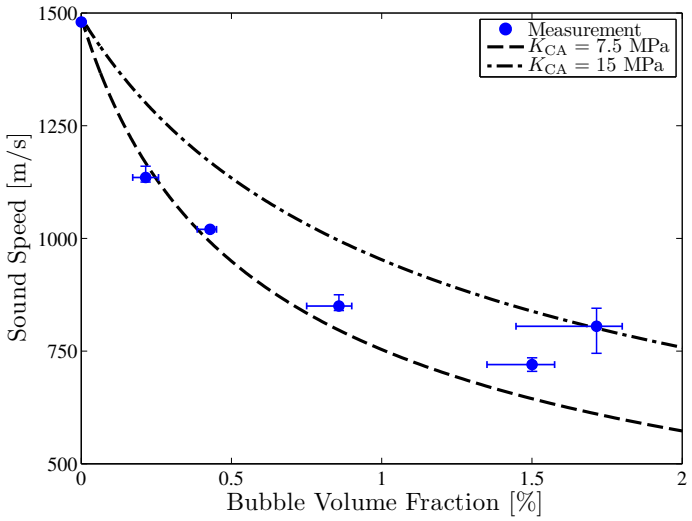


**Figure 4.6:** Measured sound speeds as a function of microbubble volume fraction. The solid and dashed reference lines are the Wood's law predictions for the indicated contrast agent bulk modulus $K_{\mathrm{CA}}$.

#### 4.2.3.3 Results

The results of these measurements are shown in Fig. 4.6. The leftmost data point indicates a measurement made with a blank gel, and demonstrates that even when occupying a significant volume ($v_{\mathrm{gel}}/v_{\mathrm{water}} \simeq 0.05$), there is no discernable effect on sound speed. However, as the volume of contrast agents is increased, the sound speed drops markedly. For comparison with these measurements is plotted the Wood's law prediction for the indicated contrast agent bulk modulus. The density of the microbubbles was stated by the synthesis team to be 24 kg/m$^3$, but with such low volume fractions, a very precise contrast agent density is not necessary.

The results imply that the contrast agents have a bulk modulus of about 10 MPa. While they are significantly stiffer than air bubbles ($K_{\mathrm{air}} \simeq 0.1$ MPa), the encapsulated microbubbles are still much more compliant than the surrounding liquid ($K_{\mathrm{water}} \simeq 2.2$ GPa). While the contrast is lessened from the results seen in Section 3.3.3 since the contrast agents are stiffer than air bubbles, even a volume fraction of a few percent was sufficient to reduce the effective sound speed by up to 50%.

#### 4.2.3.4 Sources of Uncertainty

The contrast agents were prepared and a stated volume fraction of the contrast agents, with respect to the volume of the gel, was given. While this relative volume of the bubbles was quite accurate, the volume of the gels themselves needed to be measured. A displacement measurement was made of each sample, with uncertainty on the order of 1 mL. Since the samples were further subdivided, occasionally small pieces would detatch from a section of the gel and float to the top of the water column. The contrast agents contained in this small amount of gel would not affect the measured spectrum (since they were then at a pressure null), but the volume fraction in the tube was now potentially less. The uncertainty in volume is represented by the horizontal error bars in Fig. 4.6.

While the spectra were generally very clear, there was some deviation of the phase speeds implied by the measured resonance peaks and those predicted using Lafleur and Shields' model. These deviations are represented by the vertical error bars in Fig. 4.6. Typically, these errors were on the order of a few percent. Overall, results indicate fairly consistently that the contrast agents have a bulk modulus of about 10 MPa.

### 4.2.4 Reflection due to Contrast Agents

Since the bulk modulus of the pre-expanded contrast agent was found to be about 10 MPa in Section 4.2.3, an estimate of the magnitude of the contrast that these contrast agents might provide in rock can be made. The impedance $Z_r$ of saturated limestone is computed both with and without contrast agents. By assuming that the expanses of water-saturated limestone and water-saturated limestone with contrast agents may be taken to be half-spaces, the reflection coefficient from the interface between the two can be calculated from Eq. (2.55), where $Z_1$ is the saturated rock impedance with no contrast agents, and $Z_2$ is the impedance with contrast agents.

Figure 4.7 shows the result of Eq. (2.55) for contrast agents with bulk moduli found from measurement ($K_{\mathrm{CA}} = 10$ MPa), at atmospheric pressure. The reflection

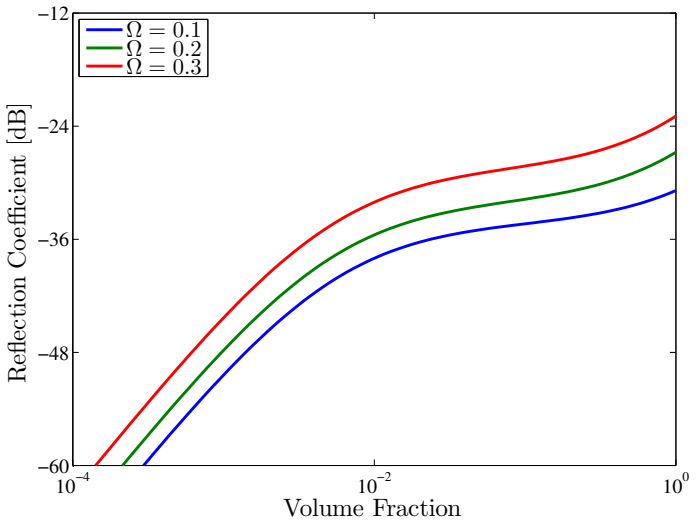


**Figure 4.7:** Plot of the reflection coefficient from the interface between water-saturated limestone and water-saturated limestone with contrast agents. The contrast agents are taken to have properties found in Section 4.2.3, namely $K_{\mathrm{CA}} = 10$ MPa and $\rho_{\mathrm{CA}} = 24$ kg/m$^3$. The volume fraction is with respect to the liquid in the pores.

coefficient is in decibels, where $\mathcal{R}_{\mathrm{dB}} = 20 \log_{10} |\mathcal{R}|$. Thus the reflection coefficient here represents the number of decibels below the incident signal the reflected signal will be. For example, for a porosity of $\Omega = 0.2$ and with a volume fraction of contrast agents of 1%, Fig. 4.7 predicts a reflected signal about 36 dB lower than the incident signal. While this is substantially lower than the incident signal, if the level of the incident signal is sufficiently high, detection of a reflected signal would be reasonable. Further, if there are no contrast agents, no reflection would be generated, since there is no change in acoustic properties of the rock. In this case $\mathcal{R}_{\mathrm{dB}} \to -\infty$.

## 4.3 Elevated Pressure

The pre-expanded contrast agents measured in the previous section are signficantly more compliant than water, and were seen to markedly reduce the sound speed in the resonator. However, this contrast must persist to higher pressures if they are to be viable contrast agents for seismic imaging. In this section, the effects

of pressure on the bulk modulus of the contrast agents is estimated and measured, and results from an ultrasonic measurement at University of North Carolina are compared to Gassmann's model, with compression of the contrast agents included.

### 4.3.1 Calculation Estimate of Bulk Modulus at Elevated Pressure

The bubble bulk modulus for a thin-shelled bubble is given by Eq. (4.1). Since $K_{\text{gas}} = \kappa P$, where $\kappa \in (1, \gamma)$ is the polytropic index, by estimating how the parameters in Eq. (4.1) change with increased pressure, it can then be estimated what the bubble modulus will be at those high-pressure conditions. Most generally,

$$K_{\text{CA}} = \frac{1}{\beta}\left(\frac{\kappa P_0}{\beta^{\kappa-1}} + 4\mu\frac{h}{R_0}\right), \tag{4.5}$$

where $\beta \equiv v/v_0 = (R/R_0)^3$ and the "0" indices indicate values at ambient conditions (or some other reference condition). In the case where the compression is isothermal, i.e., $\kappa = 1$, this expression reduces to

$$K_{\text{CA}} = \frac{1}{\beta}K_{\text{CA},0}, \tag{4.6}$$

where $K_{\text{CA},0} = P_0 + 4\mu h/R_0$. See Appendix A for derivation of Eqs. (4.5) and (4.6). If the shell thickness is set to 0, then one recovers the result for isothermal gas bubbles. The shell properties were assumed not to vary with the increased pressure.

It is important to note that Eq. (4.5) accounts only for ideal gas behavior within the bubble. Shells with variable properties and effects of condensation or mixed states in the bubble core are not considered.

### 4.3.2 Measurements at Elevated Pressure

Since the bulk modulus of the contrast agents has been measured at atmospheric conditions, it is desired to determine how this stiffness would vary with increased pressure. Indeed, the chief advantage of contrast agents with an encapsulating shell is their stability and longevity compared to pure gas bubbles. The measurements described in this section were performed with the same variety of microbubbles as those in Section 4.2.3.

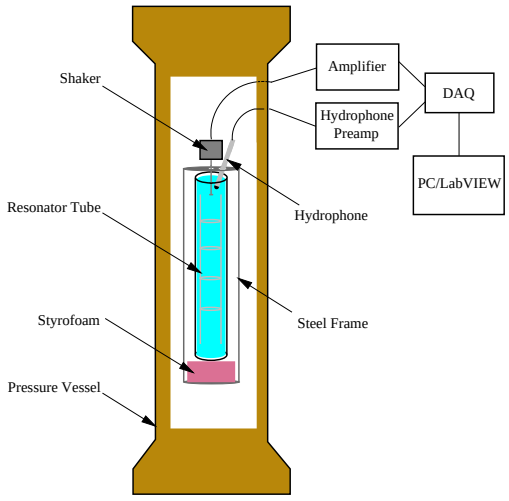


**Figure 4.8:** Experimental apparatus for measurements at elevated pressure. The chamber was pressurized by a compressed air cylinder. A photograph of the pressure vessel is shown in Fig. 4.9(b).

#### 4.3.2.1 Experimental Apparatus

The relatively compact aparatus used for the atmospheric measurements of gas and encapsulated bubbles was readily adapted to an existing on-site pressure vessel. A diagram of the experimental apparatus is shown in Fig. 4.8. The pressure vessel is made of grade 316 stainless steel, and the chamber itself has an inner diameter of 14 cm and length of about 1 m. The vessel was pressurized using medical-grade breathing air from a compressed air cylinder, which was passed through an emergency relief valve and control valves to allow the airflow into the chamber to be monitored and controlled.

To fit and position the resonator, shaker, and hydrophone into the chamber and allow the appropriate connections to be made, a steel frame was fabricated to be placed in the vessel. The steel frame is shown in see Fig. 4.9(a), and the pressure vessel in which it was placed is shown in Fig. 4.9(b). The top and bottom of the stand were 1 cm thick steel disks, connected by four vertical steel dowels. Several inches of Styrofoam were placed on the bottom disk to support the resonator tube and to provide an approximate pressure-release surface. The top disk had two holes, one each to support the hydrophone and the shaker. This had the unfortunate drawback of mechanically coupling the source and receiver. While the two had been separately supported for atmospheric measurements, space constraints did not allow for a simple

**(a)** **(b)**

**Figure 4.9:** (a) Steel frame fabricated for use in pressure vessel. Shaker and hydrophone sheath are positioned as they were during measurements. (b) Photograph of the pressure vessel. The entire vessel measures 1.3 m from top to bottom. Photograph in (b) courtesy of Preston Wilson.

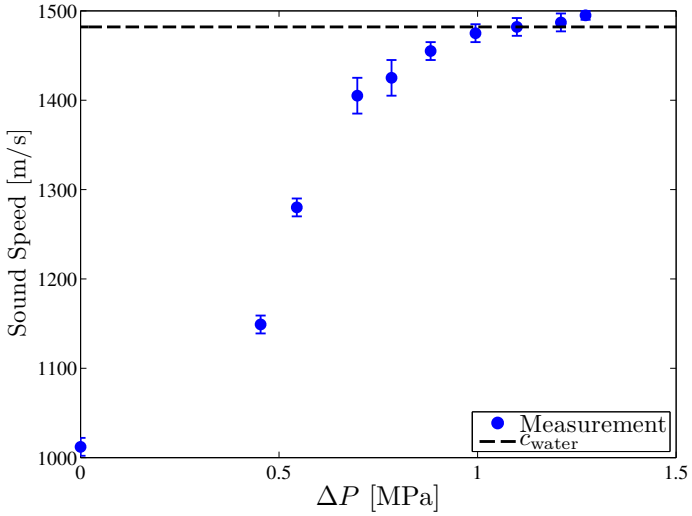


**Figure 4.10:** Measured sound speeds as a function of pressure for the same pre-expanded contrast agents used in Section 4.2.3. Dotted reference line is the sound speed in pure water, which is effectively invariant over this pressure range.

or consistent isolated arrangement to be achieved within the chamber. However, foam was placed around the supports of each, and calibration showed no discernible effect of this connection. The frame, together with the resonator tube, hydrophone, and shaker were placed inside the pressure vessel, and the electrical connections were made through hermetically sealed BNC connectors to the data collection system used for atmospheric measurements.

#### 4.3.2.2 Results

The same bubble samples as those used to generate Fig. 4.6 were placed in the resonator within the pressure vessel, the pressure was increased, allowed to fully equilibrate for several minutes, and then a spectrum was recorded in the same manner described in Chapter 3. After correcting for the elasticity of the glass tube, inferred sound speeds were plotted in Fig. 4.10. The effect of elevated pressure acting on compliant microbubbles becomes clear very quickly. The contrast agents used in these measurements and in those described in Section 4.2.3 contained a gas at approxi-

mately atmospheric pressure. As the pressure increases above several atmospheres, despite the reinforcement of the elastic shell, the external pressure causes the contast agents to compress substantially. As the pressure exceeds $0.5 - 1$ MPa, or about $5 - 10$ atm, the contrast agents are compressed enough to effectively negate their ability to provide contrast.

Computing the dependence of the bulk modulus of the contrast agents $K_{\mathrm{CA}}$ on pressure is more ambiguous, as extraction of this parameter from Wood's law requires knowledge of the bubble fraction $\phi$. If the bubble size as a function of pressure is known (i.e., if $\beta$ is known), then this calculation can be made. However, since the contrast agents could not be observed during measurement, estimating their volume fraction or bulk modulus accurately becomes impossible.

### 4.3.3 Comparison of Ultrasonic Measurements with Gassmann Prediction

The synthesis group at University of North Carolina had the facility to make preliminary ultrasonic measurements of the sound speed through a porous rock sample. Unlike the resonance tube measurements, their experiment sought to compute the speed of sound from a time-of-flight calculation. If $\Delta t$ is the time interval between the transmission and reception of an ultrasonic pulse, then the sound speed through the sample of width $d$ is simply $c = d/\Delta t$. Their experimental apparatus is shown in Fig. 4.11. The center frequency of the pulse used was 1 MHz. While this is significantly higher than the kilohertz-range frequencies used for resonance tube measurements, it is still expected to be below the resonance frequencies of the microbubbles. The expected bubble resonance frequency $f_0 = \frac{1}{2\pi}(3K_{\mathrm{CA}}/\rho_{\mathrm{liq}}R_0^2)^{1/2}$ is on the order of $10^7$ Hz, which is an order of magnitude above the interrogation frequencies. First a pulse was sent through a sample of water-saturated rock. Contrast agents, with a relative volume of $\phi_0 = 0.02$ with respect to the liquid in the pores at atmospheric pressure, were then added to the rock. In both cases, the rock was placed within a pressure chamber, allowing a pressure-dependent sound speed

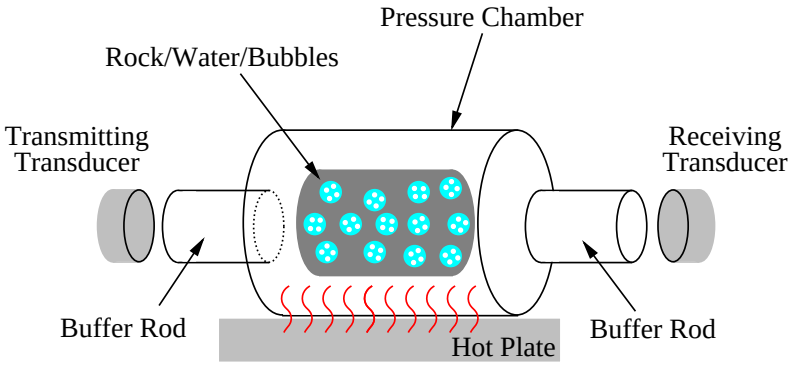


**Figure 4.11:** Experimental apparatus for ultrasonic measurements performed at UNC. The rock was filled with either water or a water/microbubble mixture. The porosity was $\Omega = 0.8$, and the initial bubble volume fraction was $\phi_0 = 0.02$. The pulse center frequency was 1 MHz.

to be measured. The sound speed through the rock with and without the contrast agents was measured as a function of pressure. The parameters for the experiment are UNC are now used for a Gassmann's equation calculation, the specifics of which are described below.

#### 4.3.3.1 Rock Properties

The rock used for measurements, which is shown in Fig. 4.12, was highly porous and had no empirical data available for computations. Instead, since the individual mineral components and their relative volumes were known, effective properties of the rock mineral could be estimated by basic mixture laws. Due to the very large porosity, the mineral bulk modulus was taken to be given by the Reuss average[40,53]

$$\frac{1}{K_{\min}} = \sum_{i=1}^{N} \frac{\varphi_i}{K_i}, \tag{4.7}$$

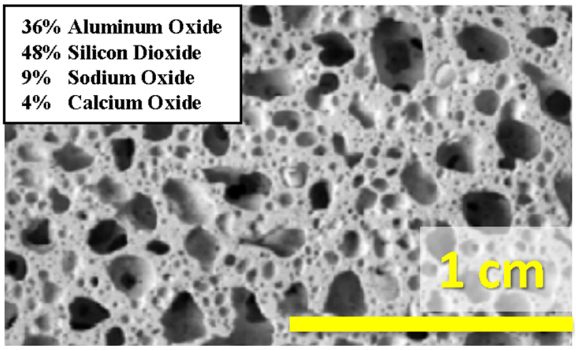


**Figure 4.12:** Close-up photograph of the porous rock used for the ultrasonic measurements. Photograph courtesy of UNC.

where $\varphi_i = v_i/v_{\text{tot}}$ is the relative volume of the component with respect to the entire volume.[†] The mineral density was calculated with the parameters from Table 4.1:

$$\rho_{\text{min}} = \sum_{i=1}^{N} \varphi_i \rho_i = 3040 \text{ kg/m}^3. \tag{4.8}$$

| Component | $\varphi$ | $K_{\text{min}}$ [GPa] | $\rho_{\text{min}}$ [kg/m$^3$] |
|---|---|---|---|
| Aluminum Oxide[97] | 0.36 | 226 | 3970 |
| Silicon Dioxide[97] | 0.48 | 30 | 2200 |
| Sodium Oxide[98, 99] | 0.09 | 60 | 2270 |
| Calcium Oxide[99, 100] | 0.04 | 105 | 3350 |

**Table 4.1:** Mineral properties assumed for the Gassmann's equation calculations. Relative volumes $\varphi$ taken from stated values. The material properties (and their dependencies on conditions) are themselves as nuanced as that of the contrast agents. However, these values are taken to be reasonable estimates.

The effective density of the of the water-saturated rock is then

$$\rho_{r1} = (1 - \Omega)\rho_{\text{min}} + \Omega\rho_{f1} = 1808 \text{ kg/m}^3, \tag{4.9}$$

and for the case of water with contrast agents, the pore fluid density is computed from Wood's law, Eq. (2.14).

[†]The symbols $\varphi$ and $\phi$ represent the same property. However, $\varphi$ will be used for the rock volume fraction and $\phi$ for the bubble volume fraction

Measurements showed a P-wave velocity of $V_P^{r1} = 1520$ m/s for the rock saturated with only water.[†] Since $V_P^{r1} \simeq c_{\text{water}}$, it was assumed that the dry frame stiffness was negligible compared to that of the water. Setting $K_{\text{dry}}$ in Eq. (2.63) to zero gives

$$K_{r1} = \frac{K_{\min}}{\Omega\left(K_{\min}/K_{f1} - 1\right) + 1} = 2.79 \text{ GPa}. \tag{4.10}$$

The shear modulus of the saturated rock was then found from

$$\mu_r = \frac{3}{4}\left[\rho_{r1}\left(V_P^{r1}\right)^2 - K_{r1}\right] = 348 \text{ MPa}. \tag{4.11}$$

The addition of contrast agents is assumed not to alter the shear modulus, which is not appreciably affected by the pore fluid.[40] For these calculations, the porosity was taken to be $\Omega = 0.8$, which was the stated value for the measurements.

Now that the water-saturated rock properties are known, the bulk modulus of the rock saturated with water and contrast agents is calculated from Eq. (2.66). With the expressions for the density, bulk modulus, and shear modulus, the P-wave velocity through the rock with water and contrast agents is calculated from Eq. (2.56), and compared with experimental results obtained by UNC.

#### 4.3.3.2 Contrast Agent Properties

The unknown parameter for this measurement was the bulk modulus of the contrast agents, since those used for this experiment were not the same variety as those measured in Section 4.2.3. An initial bulk modulus of the contrast agents was estimated to be $K_{\text{CA},0} = 30$ MPa, and the initial volume fraction was reported as $\phi_0 = 0.02$. While the density of the contrast agents was accounted for with $\rho_{\text{CA},0} = 24$ kg/m$^3$, the effect of density is very small for the small volume fractions relevant to the measurement. The pressure-dependent bulk modulus, density, and volume fraction of the contrast agents were then computed by Eqs. (2.49), (2.50), and (2.51), respectively.

[†]It was assumed that this P-wave velocity was independent of pressure. Although UNC's measurements did show a small pressure dependence, fluid and rock compression are not accounted for in the substitution relation used, and so $V_P^{r1}$ was assumed constant.

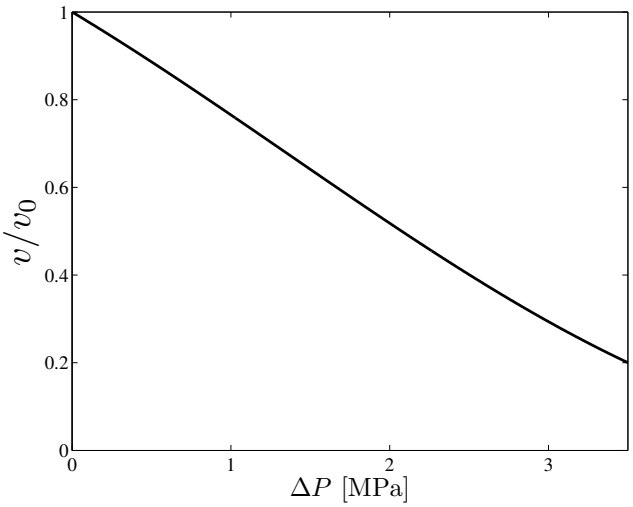


**Figure 4.13:** Compression factor $\beta = v/v_0$ assumed for the calculations, given by Eq. (4.12). Note that this is an empirical fit, not based on any measurement of the variance of the size of the contrast agents with pressure.

All that remains is to define how the volume of the microbubbles changes as a function of the pressure. Since the contrast agents were embedded in the rock, they could not be observed during the measurement. Instead, $\beta$ was estimated to fit the measured data, and a reasonable fit was achieved with

$$\beta = [1 - B_1(\Delta P) - B_2(\Delta P)^2 - B_3(\Delta P)^3]^{\frac{1}{3}}, \tag{4.12}$$

where $\Delta P$ is the pressure in megapascals above ambient, $B_1 = 0.15$ MPa$^{-1}$, $B_2 = 87$ MPa$^{-2}$, and $B_3 = 7.3 \times 10^3$ MPa$^{-3}$. The relative volume of the contrast agents as a function of pressure, given by Eq. (4.12), is plotted in Fig. 4.13.

#### 4.3.3.3 Results

At each pressure, $K_{\mathrm{CA}}$ was calculated from Eq. (2.49), and then substituted into Eq. (2.64) to find the bulk modulus of the saturated rock with contrast agents in the pore fluid. Then the saturated rock density was calculated from from Eq. (4.9), where the pore fluid density $\rho_{f2}$ was calculated from Wood's law, with the compressed density of the contrast agent taken into account. Finally these values were used to

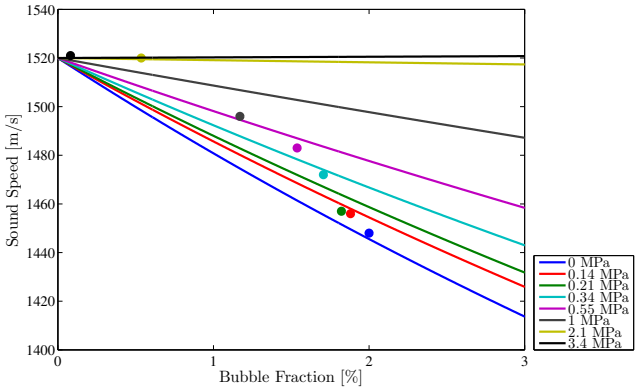


**Figure 4.14:** The colored lines represent computed sound speed curves at the indicated pressure, as a function of bubble fraction, computed using the method described in Section 4.3.3.3. The dots indicate the sound speed measured by UNC, and the bubble fraction is obtained from Eq. 4.12.

calculate the predicted P-wave velocity of the rock saturated with water and contrast agents using Eq. (2.56).

As the pressure increases, the decrease in sound speed is smaller for a fixed bubble fraction, since the bubbles are stiffer. If the match were perfect, each colored line in Fig. 4.14 would intersect the corresponding circle of the same color. For each of the colored circles in Fig. 4.14, the sound speed for the correspondingly colored Gassmann's equation prediction at that bubble fraction was recorded. These sound speeds are plotted in Fig. 4.15 (blue circles) for comparison with the actual results (red squares) measured by the group at UNC. The results show reasonable agreement up to 3.5 MPa.

While the form of $\beta$ was estimated to match the measurements, its form does not seem unreasonable. Indeed, Fig. 4.16 shows the prediction of the pressure-dependent sound speed with the assumed $\beta$, compared with the measurement of similar bubbles from Section 4.2.3.3. As the pressure increases, the bubbles are compressed, and near 3 MPa, their total volume, and thus $\phi$, are reduced by a factor of 4. This means that as the pressure is increased, the change in sound speed due to the bubbles becomes smaller and smaller. While the fit is not a perfect match, Eq. (2.53) is applicable for an isothermal ideal gas and invariant shell properties, conditions which may not have

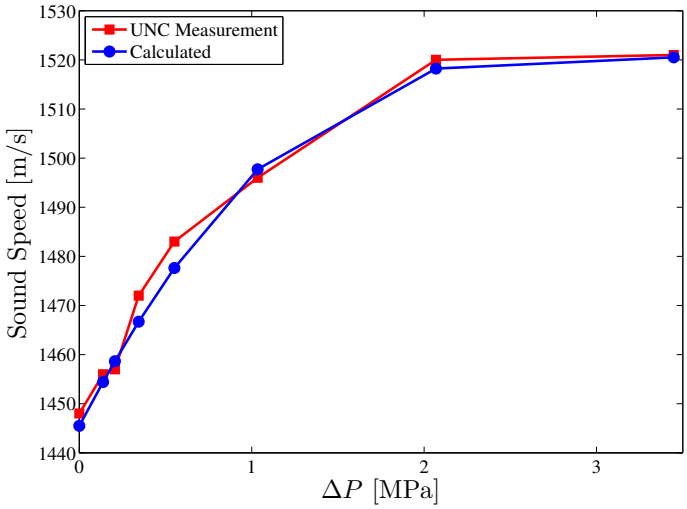


**Figure 4.15:** Gassmann's equation prediction compared with measurement.

been satisfied during the experiment. Also, the steeper transition from lower to higher sound speeds in the measured data was a result of the collapsing of the stiffer-shelled bubbles. This buckling was not considered in the compression modeling.

### 4.3.4 Layer Contrast Enhancement

With an estimation of the bulk modulus of the contrast agents as a function of pressure in hand, an estimation of the effect of bubbles on reflection from an oil-water interface is now made. The reflection coefficient magnitude for the interface between half-spaces of water and oil is about $-13$ dB, meaning the reflected signal will be about 13 dB lower than the incident signal. A $d = 10$ cm layer of water with contrast agents is now placed between the two half-spaces; see Fig. 4.17. The reflection coefficient is computed using Eq. (2.48). The difference between these two reflection coefficients defines the contrast enhancement, and in decibels, the difference is $20 \log_{10} |\mathcal{R}_{\text{layer}}/\mathcal{R}_{\text{nolayer}}|$.

The sound speed and density of the layer are calculated from Wood's law, with the effects of volumetric compression estimated for the measurement, Eq. (4.12). From Fig. 4.18, at atmospheric pressure (a depth of 0 m, blue line), a layer with about 3%

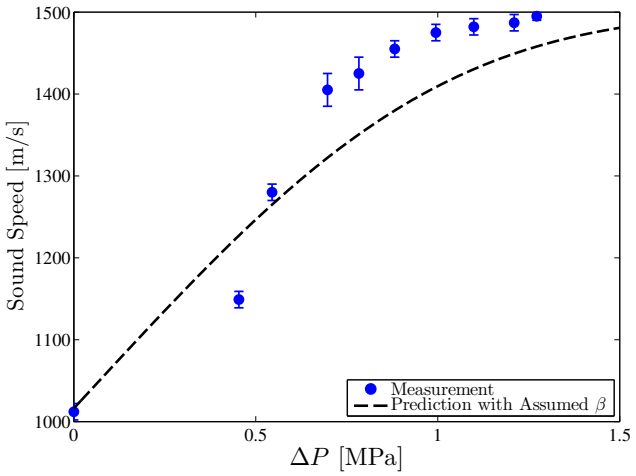


**Figure 4.16:** Comparison of the data measured with encapsulated bubbles (from Fig. 4.10), which were similar to those used in the rock experiments. The dashed line shows the sound speed, given by Eq. (2.53), with the compression factor $\beta(P)$, Eq. (4.12), used for the rock experiment comparison.

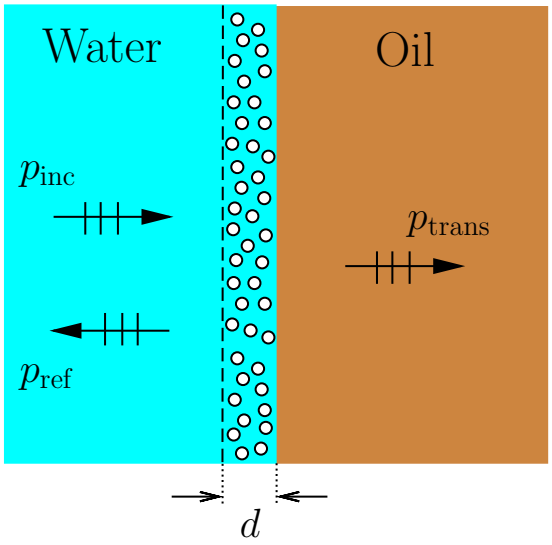


**Figure 4.17:** Diagram of microbubble layer at an oil/water interface. The thickness $d$ is 10 cm.

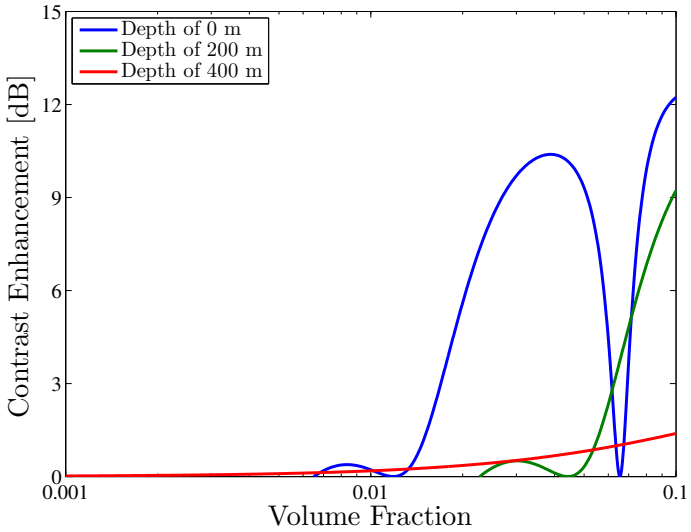


**Figure 4.18:** Plot of the contrast enhancement provided by a layer of contrast agents positioned between half-spaces of water and oil. The frequency is 2 kHz, and the layer is taken to be 10 cm thick. The volume fraction is the relative volume of contrast agents within the layer.

contrast agents provides a 10 dB enhancement of the reflected signal compared to the case without contrast agents. At a depth of 200 m (green line), the enhancement is only about 1 dB for this volume fraction. However, as the volume fraction in the layer nears 0.1, up to 9 dB of enhancement is predicted. Very little enhancement due to the contrast agents is expected for a depth of 400 m (red line), even at volume fractions above 10%. As was seen in Section 4.3.3, a depth of 400 m corresponds to a pressure of about 4 MPa. At these pressures, the microbubbles are compressed substantially and provide very little contrast. It should be noted that the bubbles in these experiments were not designed for use at pressures higher than 10 atm (1 MPa), which is equivalent to a hydrostatic load of 100 m.

## 4.4 Elevated Temperature

The substantial bubble compression and subsequent loss of acoustic contrast seen in the measurements in Section 4.3.2 is a result of the inability of the pre-expanded contrast agents to withstand pressure. The gas inside those microbubbles was at

approximately atmospheric pressure, and so even with the added strength of the shell, the bubbles collapsed under about 10 atm.[101] The problem might be remedied if the gas inside were at some higher pressure, though not so high as to make the bubbles as stiff as the surrounding fluid.

The synthesis team at UNC developed bubbles that contain a fluid (or multi-phase) core at atmospheric pressure. If the bubble is heated, then the contained fluid expands and become gaseous. In this case, the expansion of the bubble is controlled by the ambient pressure, such that the gas core is at a pressure similar to that in the liquid. This prevents the collapse seen at just a few atmospheres which occurred in the measurements made with the pre-expanded bubbles.

There are two important reference temperatures that control the ability of the microbubbles to provide acoustic contrast to the surrounding fluid. The first is the glass transition temperature $T_g$, which is the temperature below which a material's molecules will form an amorphous crystalline lattice, causing the material to appear glassy.[102] When the temperature is below the glass transition temperature of the shell material, the shells exist in a more rigid crystalline state, implying a higher shear modulus of the shell, and thus the bubbles themselves are stiffer overall. However, as the glass transition temperature is approached, the polymer chains become more mobile, and the shells, and thus the bubbles, become more compliant.

The second important temperature is the bubble expansion temperature $T_e$. Governed by the fluid or fluids contained in the shell, when the temperature rises above $T_e$, the core undergoes a phase transition and causes the bubbles to expand to 2–2.5 times their initial diameter (or about 10–20 times their initial volume). This temperature is generally above the glass transition temperature, that is, $T_e > T_g$. Otherwise, the gas would be attempting to expand against a more rigid boundary. The expansion occurs when the shell is more rubber-like, and sufficiently compliant to survive the expansion. For the bubbles used in measurements described below, the glass transition temperature was approximately $T_g \simeq 70°\text{C}$ and the bubble expansion temperature was $T_e \simeq 125°\text{C}$.

### 4.4.1 Experimental Apparatus

The first challenge presented in extending measurements to elevated temperatures was that of sample preparation. The water-based polyacrylamide gel used to encapsulate the pre-expanded bubbles loses its integrity at temperatures above 50°C, and so it would not be able to provide a means of properly distributing the bubbles above this temperature. Instead, a glycerol-based polyacrylamide gel matrix was developed by UNC and the contrast agents were again embedded inside. The newer gels are stable well above 100°C, and so remain intact at the requisite temperatures. Blank gel samples were again tested over this temperature range and showed no substantial effect on the measured sound speed; see Appendix C. The gels containing the bubbles were placed in the resonator, and the spectra were recorded as described in Section 4.2.3.2.

The temperature range of the measurement was limited by the equipment: the operating range of the hydrophone has a manufacturer-specified upper limit of 80°C. While brief excursions above this temperature were permissible, the output signal was noticeably noisier, making the tube resonances much more difficult to discern. Hydrophones able to withstand temperatures above 80°C are less readily available. Also, as the water approaches the boiling point, any remaining dissolved gas is more likely to form bubbles, and the appearance of water vapor bubbles is imminent. These two effects make measurements in temperature ranges much above 80° much more difficult.[†]

The bubbles used had an expansion temperature of about $T_e = 120$°C, and so it was expected that the bubbles would remain at their initial sizes during these measurements. Thus, the bubble fraction $\phi$ would not change.

In order to heat the water and samples, a BriskHeat model BWH-D high-temperature element was coiled around the outside of the glass resonator. The heating element

[†]The onset of boiling varies significantly with pressure. If the surrounding pressure were raised by a few atmospheres, boiling could be avoided near $T_g$.[23]

was about 2.5 cm wide and 1.2 m long, and so there were approximately 2 cm gaps between the coils of the element. The heating element was affixed to the glass tube using high-temperature adhesive tape, and then connected to a variable AC controller. The voltage was set to 40% of the wall voltage (120 $V_{rms}$), which caused the water in the tube to increase its temperature by about 1°C per minute.

Another concern faced in adapting the resonator experiment to higher temperatures was the temperature rating of the pressure vessel. While results of measurements under elevated temperatures and pressures are not presented, such experiments are a thrust of future work on this topic. The vessel used for pressure measurements described in Section 4.3.2 has a temperature rating of 54.4°C, well below the temperature range relevant to the bubbles. To ensure that the temperature around the tube would remain within the required operating range, mineral wool pipe insulation was placed around the resonator and heating element, and a PVC tube with an inner diameter of 10.2 cm was used to enclose the entire assembly; see Fig. 4.19. A rounded cap was fitted with a Styrofoam insert to support the bottom of the tube, and a 4 cm hole was drilled in a second rounded cap to provide pass-through of the signal cables and heating element power. The hole also provides a coupling to the ambient pressure conditions, so application of an elevated external pressure will not crush the PVC cell.

Lastly, two holes were drilled in a large (5 cm diameter) rubber stopper. The stopper was then fit into the top of the resonator column, which meant the water level needed to be several millimeters below the top edge of the tube. The first hole was made to secure the hydrophone sheath and position it in the water column. The second was a hole to allow the stinger of the shaker to pass through into the tube from above and allow pressure coupling, since the hydrophone's fitting was nearly airtight. The shaker was supported on a 1 cm thick silicone ring, which was in turn supported by screws in the wall of the cell. In this way, the shaker was isolated mechanically from the hydrophone. A schematic of the experimental apparatus is shown in Fig. 4.20.

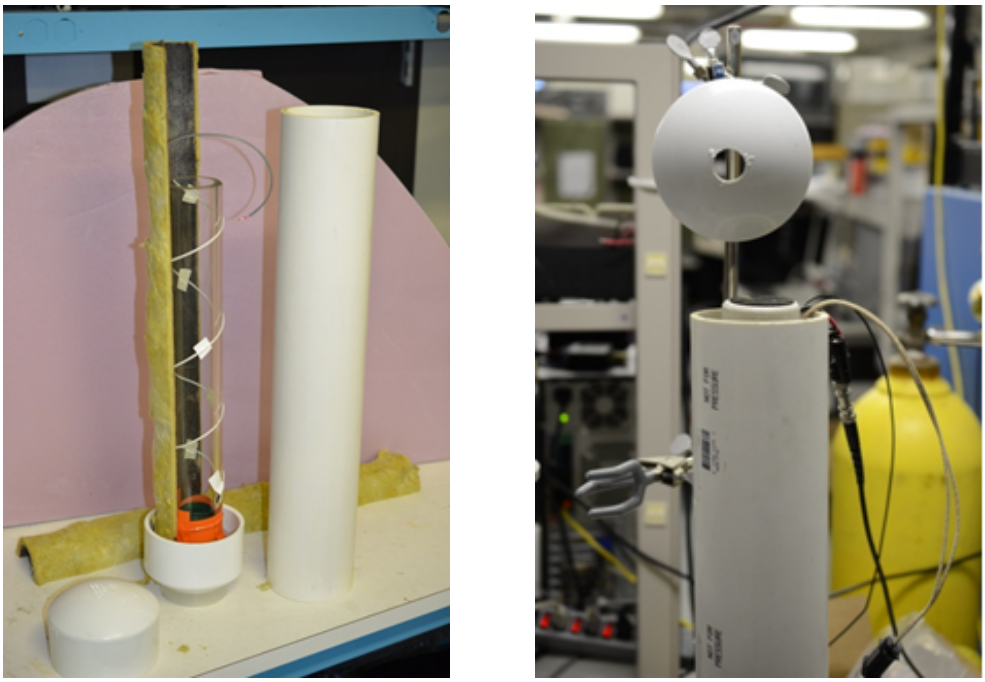

**(a)** **(b)**

**Figure 4.19:** (a) Photograph of the thermal cell with the wool insulation and the PVC housing removed. The heating wire pictured is not the same one used for measurements. (b) Photograph of top of the thermal cell with the shaker mounted, and showing the hole created for electronics pass-through and pressure coupling to the pressure chamber.

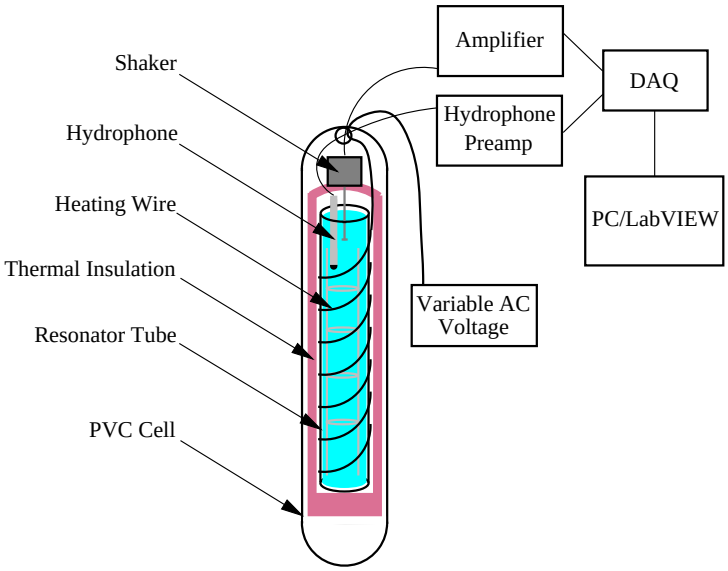


**Figure 4.20:** Experimental apparatus for the measurements at elevated temperature. Photographs of the thermal cell are shown in Fig. 4.19

### 4.4.2 Results

Figure 4.21 shows the measured sound speed as a function of temperature for the thermally-activated bubbles. Water calibration showed good agreement with existing models of sound speed variation with temperature. The bubbles are noticeably stiffer at atmospheric pressure than were the pre-expanded bubbles ($K_{\mathrm{CA}} \simeq 60$ MPa rather than $K_{\mathrm{CA}} \simeq 10$ MPa). However, as the temperature increases, the sound speed in the tube decreases, indicating that the bubbles are becoming more compliant. This softening coincides with the onset of the glass transition temperature $T_g$: as expected, the bulk modulus of the contrast agents decreases substantially as the shells become less rigid. The bulk moduli corresponding to the sound speed results are shown in Fig. 4.22

### 4.4.3 Sources of Uncertainty

The volume of the bubbles was specified by the synthesis team, and, since no bubble expansion was expected, was taken to be well-defined and constant. Instead,

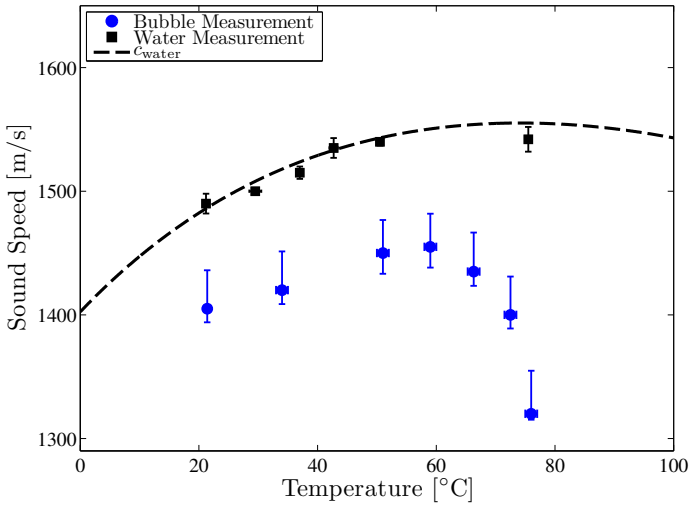


**Figure 4.21:** Measured sound speeds as a function of temperature for thermal bubbles. Dotted reference line is the sound speed in pure water from Ref. 103.

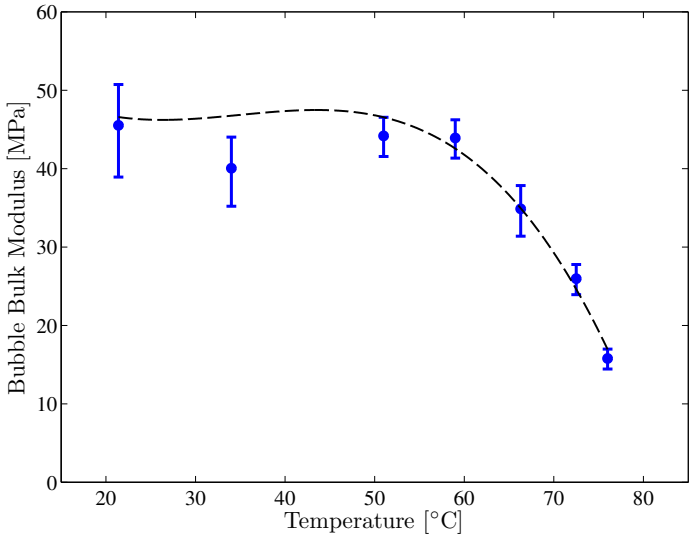


**Figure 4.22:** Bulk modulus of the thermal bubbles inferred from the sound speed measurements shown in Fig. 4.21. Dotted trend line calculated from 3$^{rd}$-degree polynomial

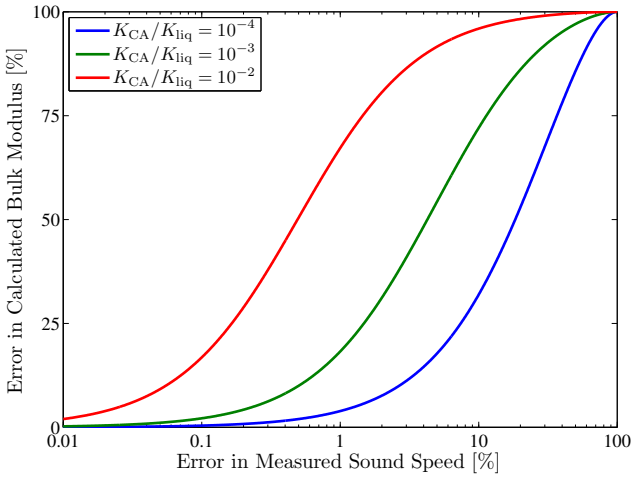


**Figure 4.23:** Plot shows the error in the extracted bulk modulus $K$ as a function of the error in the sound speed in the mixture $c_{\text{eff}}$. For materials that have a bulk modulus on the same order as the host fluid's $K_0$, very high accuracy in $c_{\text{eff}}$ is required to obtain a reasonable estimate of $K$.

measurement uncertainty was induced by two major factors: temperature measurement, and hydrophone performance. During the experiment, the voltage controller was set at about 8–12% to maintain each measurement temperature for about 10 minutes. While the temperature remained relatively constant in these intervals, it did vary by up 1.5°C. The temperature was recorded immediately before and immediately after each measurement, as positioning of the hydrophone and shaker did not allow simultaneous positioning to accommodate the thermal probe. The mean of these two readings was taken to be the temperature during the measurement. The glycerol gels were seen to induce a small, though not measureably consistent, effect on the sound speed. An uncertainty of ±2% is included in the error bars in Fig. 4.21.

While the hydrophone performed reasonably well over its specified operating range, measurements taken near its upper limit were notably noisier, and the peaks were less distinct. In general, however, the uncertainty in the measured sound speed causes smaller uncertainties in computed bulk modulus as the bulk modulus is low-

ered;[†] see Fig. 4.23. For lower temperatures, the bubbles were stiffer, but the sound speed uncertainty was smaller. At higher temperatures the reverse was true: the bubbles were softer, but the sound speed uncertainty was larger. This meant that uncertainty in the bulk modulus was fairly constant, as these two factors more or less offset one another.

## 4.5 Conclusion

While the measurements and calculations presented in this chapter are preliminary, they are nonetheless encouraging. The synthesized microbubbles were shown to provide substantial acoustic contrast at atmospheric conditions. While pressurization mitigated this effect, there is evidence that thermally activated bubbles may solve the problem of collapse and diffusion. Measurements of the behavior of the contrast agents *in situ* have proven consistent with the models described in the present chapter and in Chapter 2. These same models predict potentially detectable impedance reductions for reasonable volume fractions in porous rock.

Measurements of contrast agent properties at simultaneously elevated temperatures and pressures are needed to confirm the expected behavior, and the requirements of practical measurement conditions must be met. However, the principles underlying reduction of acoustic impedance by means of encapsulated microbubbles remain intact based on current findings.

[†]For this reason, such resonance tube measurements work less well for solid materials with $K/K_{\text{liq}} \sim 0.1 - 10$ than for gases and bubbles, for which $K/K_{\text{liq}} \sim 10^{-4} - 10^{-3}$.

# Chapter 5

# Conclusion

The effects of both pure gas bubbles and encapsulated microbubbles on acoustic propagation and reflection have been considered in this thesis. In Chapter 2, the effects of gas bubbles on the acoustic properties of both liquid and solid media were examined using appropriate theoretical models. By restricting analyses to low frequencies, it was shown that very useful simplifications can be made both to dynamical models for bubbly liquids (Zabolotskaya-Soluyan and Commander-Prosperetti) and to full treatments of poroelastic behavior (Biot theory). The resulting quasi-static models (Wood's law and Gassmann's equation, respectively), coupled with empirical data for saturated rock, allowed benchmark calculations to be made for the change in effective properties of saturated rock when gas bubbles are introduced. With the compression of the gas bubbles as the ambient pressure is increased taken into account, these calculations were extended to pressures equivalent to the hydrostatic loads at several kilometers under water. While the contrast is diminished by elevated pressure, the inclusion of gas bubbles in a liquid layer between limestone half-spaces was nevertheless seen to increase the reflection coefficient by about 10 dB. Calculations indicate that the gas bubbles lower the P-wave velocity in saturated limestone by up to ten percent, even at depths greater than a kilometer. In order to extend these results for gas bubbles to contrast agents, a suitable experimental apparatus was validated to obtain the properties of the contrast agents.

An acoustic resonator, consisting of a glass tube containing water, was shown to yield accurate measurements of the sound speed in water. By examining the frequency spectrum of the sound field in the tube when it was excited with a broad-band source, the resonance frequencies of the natural modes of the tube were identified. These

resonances, together with knowledge of the dimensions of the tube, allow the sound speed to be extracted. It was seen that, by accounting for the elasticity of the tube with existing waveguide models, the free-field sound speed could be recovered by employing existing apparatus and software at ARL:UT. Next, gas bubbles were injected into the tube at four fixed positions along the water column, and the sound speed in the bubbly water was determined in the same manner. Since the relative volume of the air was known, Wood's law could be used to determine the bulk modulus of the gas bubbles. The result for the bulk modulus $K_{\text{air}}$ was found to agree with its known value for air. The results indicated a polytropic index for the bubbles that was lower than expected (i.e., the result implied behavior that was closer to isothermal than to adiabatic). This effect was likely due to dispersive effects as the frequencies approached the resonance frequencies of the bubles ($\omega/\omega_0 \simeq 0.5 - 0.8$), a region in which the phase speed in the bubbly water is lower than the Wood's law prediction by about 10% to 20%. The lower phase speeds are predicted by dynamical models which themselves give results for an effective medium, and so effective medium behavior in the tube was determined to be a reasonable assumption.

The use of Wood's law to find $K_{\text{air}}$ is based on the assumption that the water and bubbles in the tube form an acoustically homogeneous mixture. A model of a resonance tube as a series of discrete layers with varying acoustic properties was developed to consider how the number and position of these layers affect the validity of the effective medium approximation. For four layers of pure air comprising void fractions of order $10^{-4}$, the difference between the resonance frequencies of such a layered structure and those expected for a perfectly homogeneous mixture was predicted to be about 12%, which is not very much larger than the experimental uncertainty for the measurements. However, effects of layering (e.g., additional dispersion and stop bands) were not the cause of the discrepancies from Wood's law observed in the air calibration measurements, which were more likely due to dispersion near bubble resonance. The model also predicts that positioning the layers away from the center of the tube provides a frequency spectrum closer to the result for an effective fluid

than for layers placed closer to the center. Since the layered medium model is not a full three-dimensional model of the real resonator, the number and positions of bubbles needed for a measurement cannot be determined exactly. But owing to the successful calibration using air bubbles, it was determined that four samples in the spacing used for the experiment allows unknown bulk moduli to be measured with sufficient accuracy.

With the measurement system verified, it was used to determine the bulk modulus of the microbubble contrast agents. With the contrast agents embedded in an acoustically transparent gel, the samples could be used for measurements in the resonance tube with minimal alterations to the experimental apparatus. Results of these measurements indicate that the tested pre-expanded contrast agents had bulk moduli of about $K_{\mathrm{CA}} \simeq 10$ MPa. While the contrast agents were found to be less compressible than air, as expected they are still over a hundred times more compressible than water, and were shown to reduce the sound speed in the mixture by nearly 50% with volume fractions on the order of 1%.

Ultrasonic measurements made by the synthesis team at UNC demonstrated the ability of the contrast agents to alter the sound speed in saturated porous rock. Comparison of those experimental results and the predictions of Gassmann's equation yield good agreement over the pressure ranges tested. From measurements made by UNC, the size of the contrast agents as a function of pressure was estimated. Given an initial bulk modulus and its dependence on pressure, the reflection from an oil/water interface is predicted to be increased by 5–10 dB by adding a layer of contrast agents, for pressures equivalent to a few hundred meters of ocean depth. At much higher pressures, pre-expanded bubbles were predicted to provide little to no contrast. Therefore, thermal bubbles were considered next.

Thermal bubbles, which have cores designed to undergo a phase change and expand at a controlled temperature, alleviate the problem of collapse, since they are not pre-expanded and thus do not contain a gas at atmospheric pressure. The experimental apparatus was altered to allow the liquid in the resonator to be heated.

Measurements showed that the thermal bubbles were stiffer than the pre-expanded bubbles at atmospheric temperatures, with $K_{\mathrm{CA}} \simeq 60$ MPa. However, as the temperature was raised above the glass transition temperature of the bubble shell material, which was about 60°C, the bubbles were observed to soften. Their bulk modulus at 80°C was measured to be close to that of the pre-expanded bubbles, $K_{\mathrm{CA}} \simeq 10$ MPa.

Thermal bubbles are promising in that they should remain compliant at elevated temperatures and pressures associated with down-well conditions. Given the encouraging results of predictions for gas bubbles in rock, and the preliminary results for encapsulated microbubbles, the ability of these contrast agents to provide measurable contrast in such conditions is plausible. Further measurements are needed, most importantly measurement of the bulk modulus of the thermal bubbles at simultaneously elevated temperatures and pressures. Steps have been taken to allow such measurements in the pressure chamber to be made while remaining within the operational limits of the vessel. Below the resonance frequencies of the contrast agents, the contrast provided is a result only of their compressibility, and so the response of the contrast agents is not frequency-dependent. However, corroboration of future ultrasonic measurements with measurements made at seismic frequencies is important to ensure that the acoustic contrast persists at all frequencies of interest. While many more experiments and calculations are necessary before implementation, present results indicate that encapsulated microbubbles are good candidates for providing exploitable acoustic contrast.

# Appendices

# Appendix A

# Effect of Pressure on Size of Contrast Agents

## A.1 Contrast Agent Properties

An approximate relation is derived for the change in volume of a contrast agent (CA), i.e., gas bubble with a shell, due to an increase in the ambient pressure $P$. It is assumed that density and elastic moduli of the shell do not depend on pressure. When the shell thickness is small in comparison with the shell radius, and the shell material has a shear modulus that is small in comparison with its bulk modulus (which is the case for soft[†] shell materials), then the bulk modulus of a contrast agent as a whole may be expressed as

$$K_{\mathrm{CA}} = \kappa P + 4\mu \frac{h}{R}. \tag{A.1}$$

Here, $\kappa$ is the polytropic index for the gas inside the contrast agent, $P$ is the gas pressure, with $\mu$ the shear modulus, $h$ the thickness, and $R$ the radius of the shell. The bulk modulus of the shell material does not appear in this expression because for soft, thin shells, moderate expansion of contraction of the shell occurs with minimal change in its volume, which is to say that it behaves as an incompressible material. A subscript 0 is used to denote values at atmospheric pressure, e.g.,

$$K_{\mathrm{CA},0} = \kappa P_0 + 4\mu \frac{h_0}{R_0}. \tag{A.2}$$

[†]The ratio $\mu/K = \frac{3}{2}(1-2\nu)/(1+\nu)$, where $\nu$ is the Poisson ratio. For typical rubbers, $\nu \sim 1/2$,[104] and so the ratio $\mu/K$ is very small. Thus, it can be inferred that the bulk modulus of rubbery material is much larger than its shear modulus.

First defined is the compression factor $\beta$, which relates the volume $v$ of the contrast agent to its volume $v_0$ at atmospheric pressure:

$$\beta \equiv \frac{v}{v_0}. \tag{A.3}$$

Since the mass $m$ of the contrast agent does not change (no gas diffusion is considered), the density of the bubble at some depth can be determined from its atmospheric value. That is, since $m = m_0$, then $\rho v = \rho_0 v_0$, and thus $\rho = \rho_0 v_0 / v$, or

$$\rho = \frac{\rho_0}{\beta}. \tag{A.4}$$

Since it has been assumed that shell thickness $h$ is small compared to radius $R$, and since the volume $dv$ of a spherical shell with infinitesimal thickness $dR$ is $4\pi R^2\, dR$, then $dv \simeq v^{\text{shell}}$ and $dR \simeq h$, such that

$$v^{\text{shell}} = 4\pi R^2 h. \tag{A.5}$$

At atmospheric conditions $v_0^{\text{shell}} = 4\pi R_0^2 h_0$. The volume of the shell is constant (incompressible), and thus

$$h = \frac{R_0^2}{R^2} h_0. \tag{A.6}$$

From the definition $\beta = v/v_0 = (R/R_0)^3$,

$$\frac{h}{R} = \frac{1}{\beta} \frac{h_0}{R_0}. \tag{A.7}$$

The gas within the contrast agent is taken to be ideal[†], that is, $Pv^\kappa = \text{constant}$. Thus,

$$Pv^\kappa = P_0 v_0^\kappa \tag{A.8}$$

and so

$$P = \left(\frac{R_0^3}{R^3}\right)^\kappa P_0, \tag{A.9}$$

[†]Ideal gas behavior is a reasonable assumption for air, but some gasses may require real gas behavior to be considered.[63]

or

$$P = \frac{1}{\beta^{\kappa}} P_0. \tag{A.10}$$

Now, substituting Eqs. (A.7) and (A.10) into Eq. (A.1) yields

$$K_{\mathrm{CA}} = \frac{1}{\beta}\left(\frac{\kappa P_0}{\beta^{\kappa-1}} + 4\mu\frac{h_0}{R_0}\right). \tag{A.11}$$

If Eq. (A.2) is used to eliminate the second term in Eq. (A.11), then the latter equation may be rewritten in the form

$$K_{\mathrm{CA}} = \frac{K_{\mathrm{CA},0}}{\beta} + \kappa P_0\left(\frac{1}{\beta^{\kappa}} - \frac{1}{\beta}\right). \tag{A.12}$$

Note that for an isothermal compression of the gas, $\kappa = 1$, and Eq. (A.12) reduces to $K_{\mathrm{CA}} = K_{\mathrm{CA},0}/\beta$.

If the number of bubbles is constant, then the volume fraction $\phi$ will change as the contrast agents compress: smaller bubbles contrast agents occupy a smaller fraction of the total volume. From the definition of the volume fraction and $\beta$, the volume fraction can be written in terms of an initial volume fraction $\phi_0$ as

$$\frac{\phi}{\phi_0} = \frac{v_{\mathrm{CA}}/v_{\mathrm{tot}}}{v_{\mathrm{bub},0}/v_{\mathrm{tot}}}, \tag{A.13}$$

or

$$\phi = \beta\phi_0. \tag{A.14}$$

## A.2 Estimating $\beta$

An estimation of the compression, i.e., an explicit expression for $\beta$, is now obtained. Isothermal compression is assumed, both for simplicity, and because the imagined compression is sufficiently slow that the temperature of the bubbles is able to equilibrate fully. The bulk modulus is defined as

$$K \equiv -v\frac{dP}{dv}, \tag{A.15}$$

relating the fractional change in volume due to a varied pressure. Since $v/dv = \beta/d\beta$, then

$$K_{\mathrm{CA}} = -\beta \frac{dP}{d\beta}. \tag{A.16}$$

Because Eq. (A.12) also gives $K_{\mathrm{CA}}$, taking $\kappa = 1$ for an isothermal gas and setting the right-hand side equal to that of Eq. (A.16) gives

$$\frac{K_{\mathrm{CA},0}}{\beta} = -\beta \frac{dP}{d\beta}, \tag{A.17}$$

or separating variables

$$dP = -K_{\mathrm{CA},0} \frac{d\beta}{\beta^2}. \tag{A.18}$$

Both sides may be integrated to solve for $\beta$ in terms of the pressure $P$. At atmospheric pressure, $P = P_0$ and $\beta = 1$, so

$$\int_{P_0}^{P} dP = -K_{\mathrm{CA},0} \int_{1}^{\beta} \frac{d\beta}{\beta^2}. \tag{A.19}$$

The left-hand side yields $P - P_0 = \Delta P$, and thus

$$\Delta P = K_{\mathrm{CA},0} \left( \frac{1}{\beta} - 1 \right), \tag{A.20}$$

or

$$\beta = \frac{1}{1 + \Delta P / K_{\mathrm{CA},0}}. \tag{A.21}$$

Equation (A.21) is the desired result. Finally, substituting Eq. (A.21) into Eq. (A.12) with $\kappa = 1$ yields simply

$$K_{\mathrm{CA}} = K_{\mathrm{CA},0} + \Delta P \tag{A.22}$$

for the change in the bulk modulus of an individual contrast agent.

# Appendix B

# Derivation of Fluid Substitution Relations

## B.1 Derivation of Eq. (2.64)

Beginning with Eq. (2.63), and rearranging such that all rock- and fluid-specific terms are on one side, gives

$$\frac{K_{\text{dry}}}{K_{\text{min}} - K_{\text{dry}}} = \frac{K_f}{\Omega(K_{\text{min}} - K_f)} - \frac{K_r}{K_{\text{min}} - K_r}. \tag{B.1}$$

Then the values for the bulk moduli of two saturated rock/fluid cases are substituted in: $K_{r1}$ and $K_{f1}$, and $K_{r2}$ and $K_{f2}$. Since the left-hand side of Eq. (B.1) does not depend on the saturated bulk modulus of the rock or the bulk modulus of the pore fluid, the right- and left-hand sides of both fluid cases can be equated. Doing so and rearranging gives

$$\frac{K_{r1}}{K_{\text{min}} - K_{r1}} + \frac{K_{r2}}{K_{\text{min}} - K_{r2}} = \frac{K_{f1}}{\Omega(K_{\text{min}} - K_{f1})} + \frac{K_{f2}}{\Omega(K_{\text{min}} - K_{f2})}. \tag{B.2}$$

Now normalize each term by its numerator:

$$\frac{1}{K_{\text{min}}/K_{r1} - 1} + \frac{1}{K_{\text{min}}/K_{r2} - 1} = \frac{1}{\Omega(K_{\text{min}}/K_{f1} - 1)} + \frac{1}{\Omega(K_{\text{min}}K_{f2} - 1)}. \tag{B.3}$$

Rearranging Eq. (B.3) gives

$$\frac{K_{\text{min}}}{K_{r2}} = 1 + \left[\frac{1}{\Omega}\left(\frac{1}{K_{\text{min}}/K_{f2} - 1} - \frac{1}{K_{\text{min}}/K_{f1} - 1}\right) + \frac{1}{K_{\text{min}}/K_{r1} - 1}\right]^{-1}, \tag{B.4}$$

which is equivalent to Eq. (2.64).

## B.2 Derivation of Eq. (2.66)

Begin with Wood's law[15] for the bulk modulus of the pore fluid containing contrast agents

$$K_{f2} = \left( \frac{\phi}{K_{\mathrm{CA}}} + \frac{1-\phi}{K_{f1}} \right)^{-1}. \tag{B.5}$$

Now Eq. (B.4) becomes

$$\frac{K_{\min}}{K_{r2}} = 1 + \left[ \frac{1}{\Omega} \left( \frac{1}{(1-\phi)K_{\min}/K_{f1} + \phi K_{\min}/K_{\mathrm{CA}} - 1} - \frac{1}{K_{\min}/K_{f1} - 1} \right) + \frac{1}{K_{\min}/K_{r1} - 1} \right]^{-1}. \tag{B.6}$$

Equation (2.66) follows directly from Eq. (B.6).

# Appendix C

# Resonance Tube Calibration

## C.1 Water, Frame, and Traps

Since the effect of the gas or encapsulated bubbles (contrast agents) was sought, it was necessary to ensure that the measurements of sound speed were both accurate and minimally altered by the presence of rigid supports in the water column. Prior to each experiment with bubbles, a measurement was taken with the frame in the water-filled resonator. Recorded spectra for examples of each case are shown in Figs. C.1–C.3. The resulting sound speeds are compiled in Table C.1. A phase speed was calculated for each peak of the spectrum, and a free-field sound speed was inferred by matching the Lafleur and Shields prediction to that phase speed. The measured sound speed $c_{\text{meas}}$ was taken to be the mean of these free-field sound speeds.

| Frame | $c_{\text{meas}}$ [m/s] | Range [%] | $c_{\text{pred}}$ [m/s] | Error [%] |
|---|---|---|---|---|
| None | 1487 | ±0.1 | 1489.0 | 0.1 |
| Frame | 1486 | ±0.3 | 1489.2 | 0.2 |
| Frame & Traps | 1482 | ±0.4 | 1487.5 | 0.4 |

**Table C.1:** Measured sound speeds $c_{\text{meas}}$ and the range for tube calibration compared with theoretical prediction for pure water at the measurement temperature from Ref. 103.

It is assumed that free-field sound speed of the fluid in the tube is constant and well-known within the range of measurements shown in Figs. C.1–C.3. While the metal frame and latex traps do alter the field in the tube from the plain water case, this alteration is small, and may be safely neglected for the purposes of the measurements in this thesis.

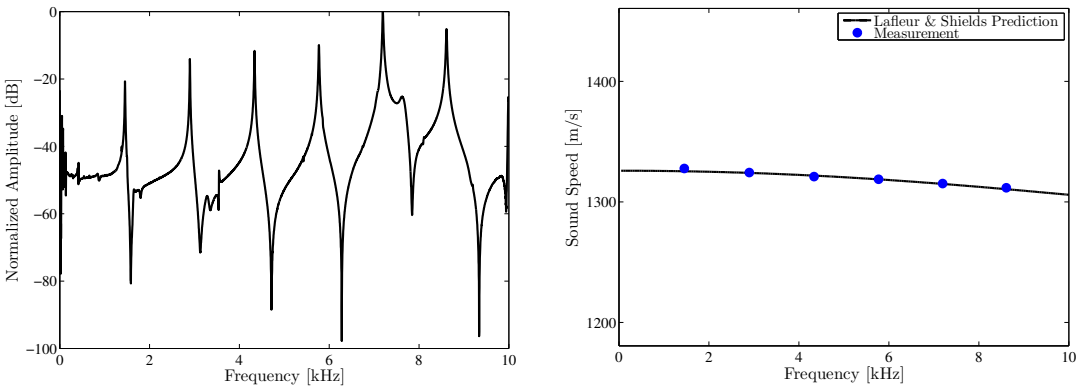


**(a)** **(b)**

**Figure C.1:** (a) Measured spectrum and (b) fit of corrected sound speed for the water-filled resonator.

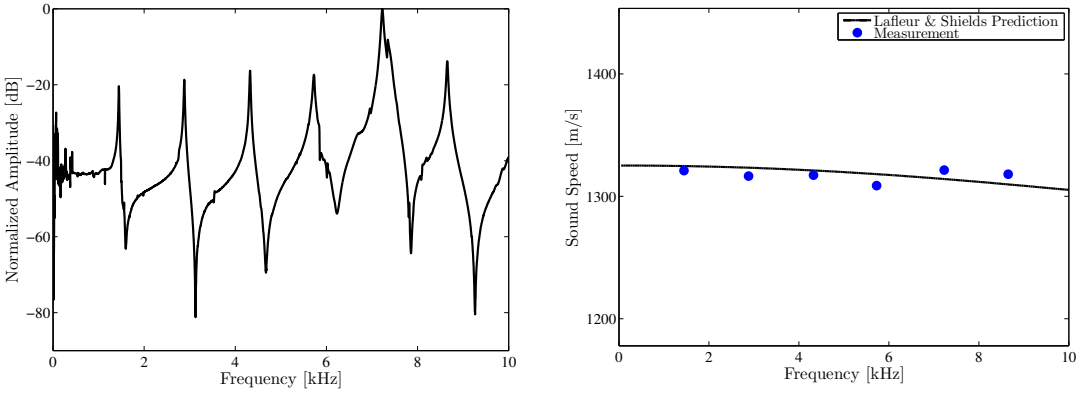


**(a)** **(b)**

**Figure C.2:** (a) Measured spectrum and (b) fit of corrected sound speed for the water-filled resonator with the aluminum frame inserted.

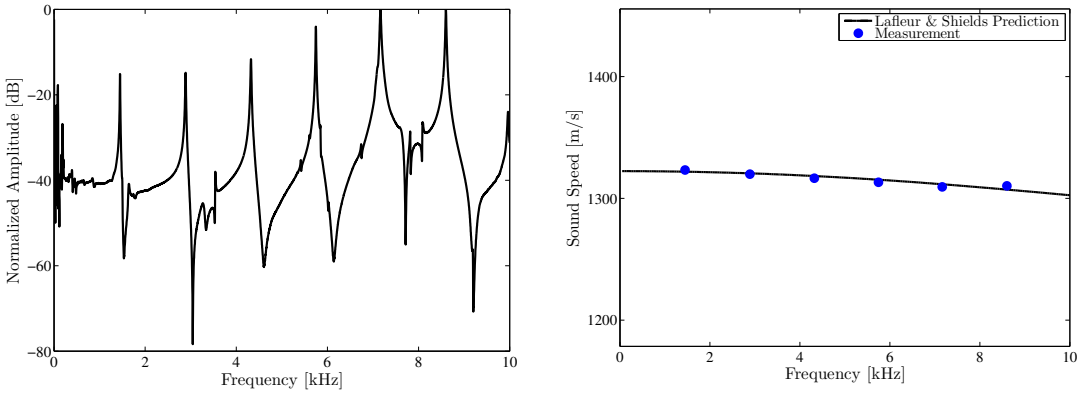


**Figure C.3:** (a) Measured spectrum and (b) fit of corrected sound speed for the water-filled resonator with the aluminum frame inserted and latex barriers.

## C.2 Heating

To ensure that the temperature of the water in the resonator (1) was and would remain sufficiently hot to make the temperature-activated contrast agents sufficiently compliant and (2) was heated in a way such that temperature gradients were minor, several calibrations were performed. First, the resonator was placed within the wool insulation and the heating element was turned on and allowed to heat the vessel to about 80°C. Then the heating power was cut off and the vessel was allowed to cool. A thermocouple was used to measure the temperature a few centimeters beneath the surface of the water in the tube every 3 to 5 minutes; measured temperature as a function of time is shown in Fig. C.4. It is worth noting that the cooling took place on a countertop, rather than in the confined space of the pressure vessel, so the cooling was likely more rapid than it would be in practical use.

Next, since the speed of sound in water is sensitive to the ambient temperature, it was necessary to make sure that the temperature profile did not vary radically along the length of the tube. The tube was heated to some temperature for which steady state was easily acheived (in this case, the temperature measured at the water's surface was $38 \pm 0.2$°C for 20 minutes). Then, the temperature probe was lowered at 1

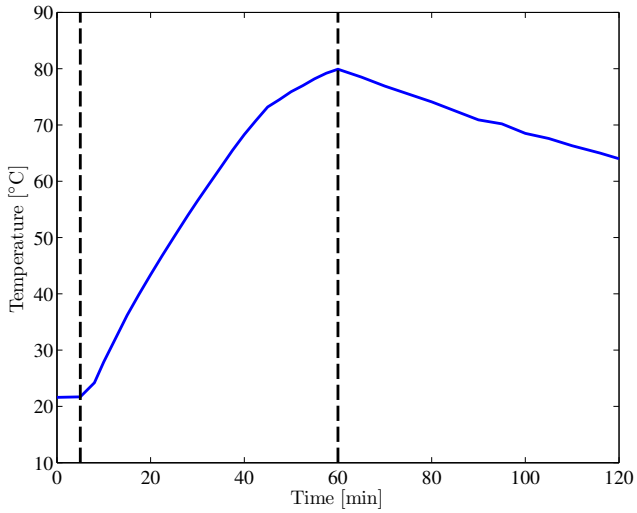


**Figure C.4:** Plot of the measured temperature in the thermal module as a function of time. The first dotted line denotes when the heating element was turned on, the second dotted line marks when heating was turned off.

– 2 cm intervals into the water column. Plotted in Fig. C.5(a) are the results. While the temperature does vary several degrees from the median temperature of 36°C, this variation implies a relatively small change in the specific acoustic impedance of the water along that same length, Fig. C.5(b). So while the temperature distribution for this case was not perfect, it was sufficient to ensure that sound speed measurements should be accurate. The uniformity of the temperature could be improved simply by acheiving steady-state for longer periods of time, allowing the fluid to equilibrate more fully.

## C.3 Measurement Calibration

To ensure that any reduction in sound speed observed in the resonator was due to the contrast agents and not the gel matrix in which they were embedded, a series of measurements were made with polyacrylamide gel and glycerol gels that contained no contrast agents. These "blanks" should affect the measured sound speed very minimally if they are to be taken as acoustically transparent.

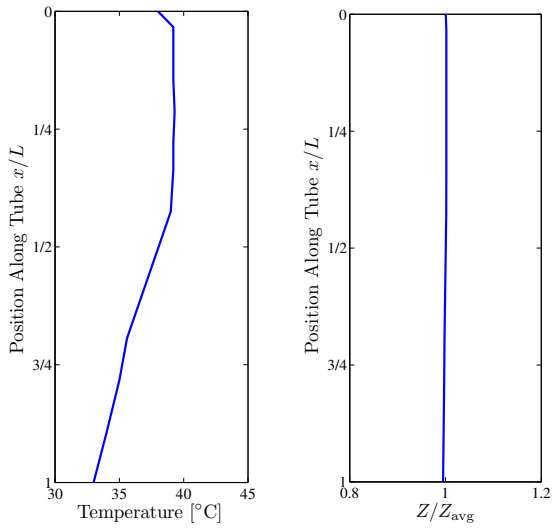


**Figure C.5:** Plots of (a) the measured temperature along the length of the resonator tube at steady state, and (b) the implied impedance at those temperatures, calculated from Ref. 103.

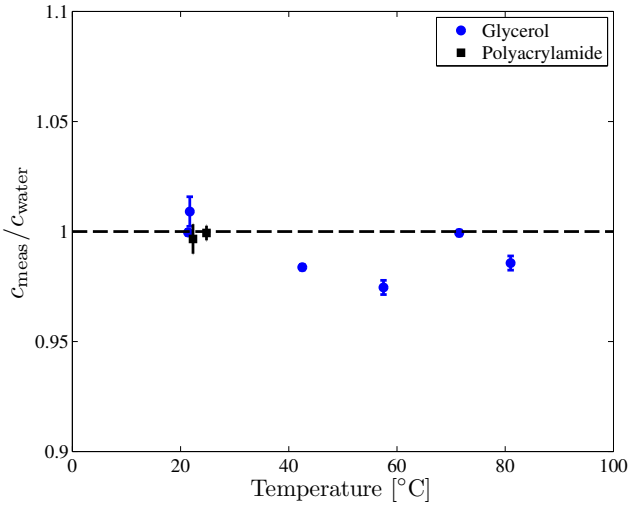


**Figure C.6:** Plot of the measured sound speed in the tube with the indicated gel type. The dotted line corresponds to the expected result for perfectly matched gels.

Figure C.6 shows measured sound speeds, as a function of temperature, for the two gel types. The error bars represent the range of free-field sound speeds for which the Lafleur and Shields prediction matched each of the measured phase speeds in the resonator; for some points in Fig. C.6, these error bars are approximately the same size as the data marker. Measurements with the polyacrylamide gels showed no effect on the sound speed within the measurement uncertainty, and so they can be taken to have no discernable effect on the measurement. The glycerol gels showed some deviation from acoustic transparency, on the order of a few percent. However, there was no trend to the variation, other than that the gels usually lowered the sound speed slightly. However, given the very small change in sound speed, inferring a temperature-dependent bulk modulus of the gels would be guesswork. Instead, an error of about $\pm 2\%$ was included for temperature-dependent contrast agent measurements, though this effect was secondary to hydrophone performance.

# References


[1] N. Warpinski, "Microseismic monitoring: Inside and out", The Journal of Petroleum Technology **61**, 80–85 (2009).

[2] E. Stride and N. Saffari, "Microbubble ultrasound contrast agents: a review", Proceedings of the Institution of Mechanical Engineers, Part H: Journal of Engineering in Medicine **217**, 429–447 (2003).

[3] M. Bruce, M. Averkiou, and J. Powers, "Ultrasound contrast in general imaging research", Technical Report, Phillips Medical Systems Nederland B.V. (2007).

[4] M. A. Borden, S. Qin, and K. W. Ferrara, "Ultrasound contrast agents", in *Molecular Imaging*, edited by B. D. R. R. Weissleder, A. Rehemtulla, and S. S. Gambhir, chapter 28, 425–444 (People's Medical Publishing House, Sheldon, CT) (2010).

[5] A. Bouakaz and P. Dayton, "Introduction to the special issue on ultrasound contrast agents and targeted drug delivery", IEEE Transactions on Ultrasonics, Ferroelectrics, and Frequency Control **60**, 5–6 (2013).

[6] T. Faez, M. Emmer, K. Kooiman, M. Versluis, and A. F. W. van der Steen, "20 years of ultrasound contrast agent modeling", IEEE Transactions on Ultrasonics Ferroelectrics, and Frequency Control **60**, 7–20 (2013).

[7] D. A. G. Bruggeman, "Berechnung verschiedener physikalischer Konstanten von heterogenen Substanzen I. Dielektrizitätskonstanten und Leitfähigkeiten der mischkörper aus isotropen Substanzen", Annalen der Physik **416**, 636–664 (1935).

[8] R. Landauer, "The electrical resistance of binary metallic mixtures", Journal of Applied Physics **23**, 779–784 (1952).

[9] S. Kirkpatrick, "Classical transport in disordered media: Scaling and effective-medium theories", Physical Review Letters **27**, 1722–1725 (1971).

[10] P. M. Morse and K. U. Ingard, *Theoretical Acoustics*, first edition (McGraw-Hill Book Company, New York) (1968).

[11] D. T. Blackstock, *Fundamentals of Physical Acoustics* (Wiley Interscience, New York) (2000).

[12] W. M. Carey and A. D. Pierce, "Sound speed, pulse spreading and reverberation in muddy bubbly sediments", Proceedings of Meetings on Acoustics **14**, 070005 (2012).

[13] A. Mallock, "The damping of sound by frothy liquids", Proceedings of the Royal Society of London A **84**, 391–395 (1910).

[14] A. B. Wood, *A Textbook of Sound*, first edition (The MacMillan Company, New York) (1930).

[15] A. B. Wood, *A Textbook of Sound*, second edition (G. Bell and Sons, London) (1949).

[16] P. S. Wilson and R. A. Roy, "An audible demonstration of the speed of sound in bubbly liquids", American Journal of Physics **76**, 975–981 (2008).

[17] R. A. Fine and F. J. Millero, "Compressibility of water as a function of temperature and pressure", Journal of Chemical Physics **59**, 5529–5536 (1973).

[18] D. G. Fredlund, "Density and compressibility characteristics of air-water mixtures", Canadian Geotechnical Journal **13**, 386–396 (1976).

[19] M. L. Cohen, "Calculation of the bulk moduli of diamond and zinc-blende solids", Physical Review B **32**, 7988–7991 (1985).

[20] M. Minnaert, "On musical air-bubbles and the sounds of running water", Philosophical Magazine **16**, 235–248 (1933).

[21] P. S. Wilson, "Sound propagation and scattering in bubbly liquids", Ph.D. thesis, Boston University (2002).

[22] L. E. Kinsler, A. R. Frey, A. B. Coppens, and J. V. Sanders, *Fundamentals of Acoustics* (John Wiley and Sons, Inc., New York) (2000).

[23] D. V. Schroeder, *An Introduction to Thermal Physics* (Addison Wesley, New York) (1999).

[24] T. G. Leighton, *The Acoustic Bubble* (Academic Press, Inc., San Diego) (1994).

[25] E. A. Zabolotskaya and S. I. Soluyan, "A possible approah to the amplification of sound waves", Soviet Physics - Acoustics **13**, 254–256 (1967).

[26] E. A. Zabolotskaya and S. I. Soluyan, "Emission of harmonic and comination frequency waves by air bubbles", Soviet Physics - Acoustics **18**, 396–398 (1973).

[27] A. Agarwal, *Nobel Prize Winners in Physics* (APH Publishing Corporation) (2008).

[28] A. I. Eller, "Damping constants of pulsating bubbles", The Journal of the Acoustical Society of America **47**, 1469–1470 (1970).

[29] K. W. Commander and A. Prosperetti, "Linear pressure waves in bubbly liquids: Comparison between theory and experiments", The Journal of the Acoustical Society of America **85**, 732–746 (1989).

[30] M. F. Hamilton, Yu. A. Ilinksii, and E. Zabolotskaya, "Dispersion", in *Nonlinear Acoustics*, edited by M. F. Hamilton and D. T. Blackstock, chapter 5, 151–175 (Acoustical Society of America, Melville, NY) (2008).

[31] M. S. Plesset and A. Prosperetti, "Bubble dynamics and cavitation", Annual Review of Fluid Mechanics **9**, 145–185 (1977).

[32] S. Temkin, *Suspension Acoustics*, first edition (Cambridge University Press, New York) (2005).

[33] Yu. A. Ilinskii and E. A. Zabolotskaya, "Cooperative radiation and scattering of acoustic waves by gas bubbles in liquids", The Journal of the Acoustical Society of America **92**, 2837–2841 (1992).

[34] J. Charles Devin, "Survey of thermal, radiation, and viscous damping of pulsating air bubbles in water", The Journal of the Acoustical Society of America **31**, 1654–1667 (1959).

[35] L. L. Foldy, "The multiple scattering of waves", Physical Review **67**, 107–119 (1945).

[36] L. van Wijngaarden, "On the equations of motion for mixtures of liquid and gas bubbles", Journal of Fluid Mechanics **33**, 465–474 (1985).

[37] R. E. Caflisch, M. J. Miksis, G. C. Papanicolaou, and L. Ting, "Effective equations for wave propagation in bubbly liquids", Journal of Fluid Mechanics **153**, 259–273 (1985).

[38] J. B. Keller and M. Miksis, "Bubble oscillations of large amplitude", The Journal of the Acoustical Society of America **68**, 628–633 (1980).

[39] L. D. Landau and E. M. Lifshitz, *Theory of Elasticity*, volume 7 of *Course of Theoretical Physics*, second edition (Pergamon Press, Oxford) (1970).

[40] G. Mavko, T. Mukerji, and J. Dvorkin, *The Rock Physics Handbook* (Cambridge University Press, New York) (2009).

[41] M. A. Biot, "Theory of propagation of elastic waves in a fluid-saturated porous solid. I. low-frequency range", The Journal of the Acoustical Society of America **28**, 168–178 (1956).

[42] T. J. Plona, "Observation of a second bulk compressional wave in a porous media at ultrasonic frequencies", Applied Physics Letters **36**, 259–261 (1980).

[43] V. Cruz and T. Spanos, "Seismic wave propagation in inhomogeneous and anisotropic porous media", Geophysics **50**, 1556–1565 (1985).

[44] F. Gassmann, "Über die Elastizität poroser Median", Vierteljahrsschrift der Naturforschenden Gesellschaft **96**, 1–23 (1951), translated by "Kathy, Christine, John, and Jim", January 1998; received from Haluk Ersoz, 14 March 2012.

[45] G. Mavko and T. Mukerji, "Seismic pore space compressibility and Gassmann's relation", Geophysics **60**, 1743–1749 (1995).

[46] M. Holmes and A. Holmes, "Petrophysical rock physics modeling: A comparison of the Krief and Gassmann equations, and applications to verifying and estimating compressional and shear velocities", in *SPWLA 46th Annual Logging Symposium* (Society of Petrophysics and Well Log Analysis) (2005).

[47] G. H. F. Gardner, L. W. Gardner, and A. R. Gregory, "Formation velocity and density – the diagnostic basics for stratigraphic traps", Geophysics **39**, 770–780 (1974).

[48] A. A. Krokhin, J. Arriaga, and L. N. Gumen, "Speed of sound in periodic elastic composites", Physical Review Letters **91** (1995).

[49] X. Zhu and G. A. McMechan, "Direct estimation of the bulk modulus of the frame in a fluid-saturated elastic medium by Biot theory", in *1990 SEG Annual Meeting* (Society of Exploration Geophysicists) (1990).

[50] P. Rasolofosaon and B. Zibszner, "Petroacoustic characterization of resevoir rocks for seismic monitoring studies", Oil and Gas Science and Technology **58**, 615–635 (2003).

[51] E. Detournary and A. H.-D. Cheng, "Fundamentals of poroelasticity", in *Comprehensive Rock Engineering: Principles, Practice and Projects, Vol. II, Analysis and Design Method*, edited by C. Fairhurst, volume 2, chapter 5, 113–171 (Pergamon Press) (1993), preprint of chapter, received from Haluk Ersoz, 14 March 2012.

[52] D. hua Han and M. L. Batzle, "Gassmann's equation and fluid-saturation effects on seismic velocities", Geophysics **69**, 398–405 (2004).

[53] A. Reuss, "Berechnung der fließgrenze von mischkristallen auf grund der plastizitätsbedingung für einkristalle", Zeitschrift für Angewandte Mathematik und Mechanik **9**, 49–58 (1929).

[54] W. Voigt, "Bestimmung der elastizitätskonstanten von eisenglanz", Annalen der Physik **24**, 129–140 (1907).

[55] R. Hill, "The elastic behaviour of a crystalline aggregate", Proceedings of the Physical Society A **65**, 349–354 (1952).

[56] H. L. F. Helmholtz, *On the Sensations of Tone as a Physiological Basis for the Theory of Music*, third edition (Longmans, Green, and Co., New York) (1895).

[57] B. R. John William Strutt, *The Theory of Sound*, volume 2, first edition (MacMillan and Co., London) (1878).

[58] U. Ingard, "On the theory and design of acoustic resonators", Journal of the Acoustical Scoeity of America **25**, 1037–1061 (1953).

[59] E. Silberman, "Sound velocity and attenuation in bubbly mixtures measured in standing wave tubes", The Journal of the Acoustical Society of America **29**, 925–933 (1957).

[60] F. Eggers, "Ultrasonic velocity and attenuation measurements in liquids with resonators, extending the MHz frequency range", Acoustica **76**, 231–240 (1992).

[61] K. A. Shapiro and I. Rudnick, "Experimental determination of the fourth sound velocity in helium II", Physical Review **137**, 1383–1391 (1965).

[62] P. S. Wilson and K. H. Dunton, "Laboratory investigation of the acoustic response of seagrass tissue in the frequency band 0.5-2.5 khz", The Journal of the Acoustical Society of America **125**, 128–134 (2009).

[63] C. A. Greene, "Low-frequency acoustic classification of methane hydrates", Master's thesis, The University of Texas at Austin (2010).

[64] C. N. Dolder and P. S. Wilson, "A simple resonator technique for determining the acoustic properties of fish schools", The Journal of the Acoustical Society of America **131**, 3287(A) (2012).

[65] C. N. Dolder and P. S. Wilson, "Multi-frequency modes in dispersive media", The Journal of the Acoustical Society of America **132**, 1929(A) (2012).

[66] G. R. Barnard, J. Bardin, and W. B. Hempkins, "Underwater sound reflection from layered media", Journal of the Acoustical Scoeity of America **36**, 2119–2123 (1964).

[67] M. D. Richardson, K. L. Williams, K. B. Briggs, and E. I. Thorsos, "Dynamic measurement of sediment grain compressibility at atmospheric pressure: Acoustic applications", IEEE Journal of Oceanic Engineering **27**, 593–601 (2002).

[68] V. A. Del Grosso, "Analysis of multimode acoustic propagation in liquid cyllinders with realistic boundary conditions - application to sound speed and absorption measurements", Acoustica **24**, 299–311 (1971).

[69] L. D. Lafleur and F. D. Shields, "Low-frequency propagation modes in a liquid-filled elastic tube waveguide", The Journal of the Acoustical Society of America **97**, 1435–1445 (1995).

[70] P. S. Wilson, R. A. Roy, and W. M. Carey, "An improved water-filled impedance tube", The Journal of the Acoustical Society of America **113**, 3245–3252 (2003).

[71] P. S. Wilson, R. A. Roy, and M. Carey, "Phase speed and attenuation in bubbly liquids inferred from impedance measurements near the individual bubble resonance frequency", Journal of the Acoustical Scoeity of America **117**, 1895–1910 (2005).

[72] H. B. Karplus, "The velocity of sound in a liquid containing gas bubbles", Technical Report C00-248, Armour Research Foundation, Illinois Institute of Technology (1958).

[73] A. Ruggles, "The propagation of pressure perturbations in bubbly air/water flows", Ph.D. thesis, Rensselaer Polytechnic Institute (1987).

[74] A. S. Dukhin, P. J. Goetz, T. H. Hines, and P. Somasundaran, "Acoustic and electroacoustic spectroscopy", Colloids and Surfaces **173**, 127–158 (2000).

[75] J. A. Kopechek, K. J. Haworth, J. L. Raymond, T. D. Mast, J. Stephen R. Perrin, M. E. Klegerman, S. Huang, T. M. Porter, D. D. McPherson, and C. K. Holland, "Acoustic characterization of echogenic liposomes: Frequency-dependent attenuation and backscatter", The Journal of the Acoustical Society of America **130**, 3472–3481 (2011).

[76] C. Devin, "Resonant frequencies of pulsating air bubbles generated in short, open-ended pipes", Technical Report 1522, David Taylor Model Basin, Hydromechanics Laboratory (1961).

[77] H. Oğuz and A. Prosperetti, "The natural frequency of oscillation of gas bubbles in tubes", The Journal of the Acoustical Society of America **103**, 3301–3308 (1998).

[78] T. Leighton, P. White, C. Morfey, J. Clarke, G. Heald, H. Dumbrell, and K. Holland, "The effect of reverberation on the damping of bubbles", The Journal of the Acoustical Society of America **112**, 1366–1376 (2002).

[79] J. Cui, M. F. Hamilton, P. S. Wilson, and E. Zabolotskaya, "Bubble pulsations between prallel plates", The Journal of the Acoustical Society of America **119**, 2067–2072 (2006).

[80] D. J. Griffiths and C. A. Steinke, "Waves in locally periodic media", American Journal of Physics **69**, 137–154 (2001).

[81] C. E. Bradley, "Time harmonic acoustic Bloch wave propagation in periodic waveguides. Part I: Theory", Journal of the Acoustical Scoeity of America **96**, 1844–1853 (1994).

[82] C. E. Bradley, "Time harmonic acoustic Bloch wave propagation in periodic waveguides. Part II: Experiment", Journal of the Acoustical Scoeity of America **96**, 1854–1862 (1994).

[83] C. E. Bradley, "Time harmonic acoustic Bloch wave propagation in periodic waveguides. Part III: Nonlinear effects", Journal of the Acoustical Scoeity of America **98**, 2735–2744 (1995).

[84] L. M. Brekhovskikh, *Waves in Layered Media*, second edition (Academic Press, Inc., New York) (1980).

[85] A. D. Pierce, *Acoustics: an Introduction to Its Physical Principles and Applications* (Acoustical Society of America, Melville, NY) (1989).

[86] M. J. S. Lowe, "Matrix techniques for modeling ultrasonic waves in multilayered media", IEEE Transactions on Ultrasonics, Ferroelectrics, and frequency control **42**, 525–542 (1995).

[87] J. L. Rose, *Ultrasonic Waves in Solid Media* (Cambridge University Press, New York) (2004).

[88] S. D. M. Adams, R. V. Craster, and S. Guenneau, "Bloch waves in periodic multi-layered acoustic waveguides", Proceedings of the Royal Society A **464**, 2669–2692 (2008).

[89] Y. Wang and B. A. Auld, "Numerical analysis of Bloch theory for acoustic wave propagation in one-dimensional periodic composites", Technical Report, Stanford University (1986).

[90] C. E. Bradley, "Acoustic Bloch wave propagation in a periodic waveguide", Technical Report, Applied Research Laboratories (1991).

[91] R. Hofstadter, *Felix Bloch 1905-1983*, ninth Dover printing, tenth GPO printing edition (National Academy of Sciences, Washington D.C.) (1994).

[92] K. M. Lee, K. T. Hinojosa, M. S. Wochner, T. F. Argo, P. S. Wilson, and R. S. Mercier, "Sound propagation in water containing large tethered spherical encapsulated gas bubbles with resonance frequencies in the 50 hz to 100 hz range", The Journal of the Acoustical Society of America **130**, 3325–3332 (2011).

[93] P. S. Epstein and M. S. Plesset, "On the stability of gas bubbles in liquid-gas solutions", Journal of Chemical Physics **18**, 1505–1509 (1950).

[94] C. C. Church, "The effects of an elastic solid surface layer on the radial pulsations of gas bubbles", The Journal of the Acoustical Society of America **97**, 1510–1521 (1995).

[95] L. Hoff, P. C. Sontum, and J. M. Hovem, "Oscillations of polymeric microbubbles: Effect of the encapsulating shell", The Journal of the Acoustical Society of America **107**, 2272–2280 (2000).

[96] S. Ravichandran and K. Ramanathan, "Acoustical parameters of polyacrylamide with sodium (meta) silicate and potassium silicate solution at 303 K", Polymer Chemistry **1**, 698–701 (2010).

[97] R. G. Munro, "Elastic moduli data for polycrystalline ceramics", Technical Report NISTIR 6853, National Institute of Standards and Technology, Gaithersburg, Maryland (2002).

[98] M. Thompson, "Density functional calculations of physical properties of sodium oxide", Master's thesis, Stony Brook University (2011).

[99] W. M. Haynes, ed., *CRC Handbook of Chemistry and Physics*, 94 edition (CRC Press) (2013).

[100] D. L. Anderson and O. L. Anderson, "The bulk modulus-volume relationship for oxides", The Journal of Geophysical Research **75**, 3494–3500 (1970).

[101] A. Zhushma, N. Lebedeva, P. Sen, M. Rubinstein, S. S. Sheiko, and P. A. Dayton, "A system for acoustical and optical analysis of encapsulated microbubbles at ultrahigh hydrostatic pressures", Review of Scientific Instruments **84**, 055105 (2013).

[102] G. Adam and J. H. Gibbs, "On the temperature dependence of cooperative relaxation properties in glass-forming liquids", The Journal of Chemical Physics **43**, 139–146 (1965).

[103] N. Bilaniuk and G. S. K. Wong, "Speed of sound in pure water as a function of temperature", The Journal of the Acoustical Society of America **93**, 1609–1612 (1993).

[104] M. H. Sadd, *Elasticity: Theory, Applications, and Numerics* (Elsevier Academic Press, New York) (2005).

# Vita

Scott Joesph Schoen, Jr. was born outside of Boston, Massachusetts to Scott and Nancy Schoen. In May of 2011 he received a Bachelor of Science from Tufts University, majoring in physics and music. He entered the acoustics program in the Department of Mechanical Engineering at The University of Texas at Austin in August of 2011. In July of 2013, he began working for Trident Research, LLC, in Austin, Texas. Scott can be contacted at ScottSchoenJr@gmail.com.

This thesis was typeset with LaTeX by the author.